The Surface Structure of $V_2O_3(0001)$

Inaugural-Dissertation

to obtain the academic degree

Doctor rerum naturalium (Dr. rer. nat.)

submitted to the Department of Biology, Chemistry and Pharmacy

of Freie Universität Berlin

by

Diplom-Chemiker

Felix Elias Feiten

from Berlin

2016

Diese Dissertation wurde von Mai 2012 bis Februar 2016 unter der Anleitung von Herrn Professor Dr. Hans-Joachim Freund in der Abteilung Chemische Physik am Fritz-Haber-Institut der Max-Planck-Gesellschaft angefertigt.

1. Gutachter: Prof. Dr. Hans-Joachim Freund, Fritz-Haber-Institut, MPG

2. Gutachter: Prof. Dr. Thomas Risse, Freie Universität Berlin

Disputation am 29.04.2016

Abstract

Vanadium oxides are widely used as catalysts in industrial reactions. The catalytic activity of a material depends on its surface structure. While the catalytic activity of $V_2O_3(0001)$ has been shown before, the surface termination of $V_2O_3(0001)$ films has been under debate since ion scattering experiments suggested that the surface is terminated by a trilayer of oxygen. This challenged the previously widespread view that the surface is terminated by a full layer of vanadyl groups.

In this dissertation the surface structure of $V_2O_3(0001)$ films was determined by combined I/V-LEED and STM measurements to clear up this controversy. Analysis of numerous preparations show that the as prepared films are terminated by a full layer of vanadyl groups with some local defects. The vanadyl terminated surface can be oxidized to a partially vanadyl covered surface showing a $\left(\sqrt{3} \times \sqrt{3}\right) R30°$ superstructure. Oxidation of the films showing a $\left(\sqrt{3} \times \sqrt{3}\right) R30°$ superstructure leads to formation and evaporation of V_2O_5. These results were combined with concurring results by Jan Seifert et al. and Joachim Paier et al. obtained from fast atom diffraction and density functional theory calculations respectively.

The surface structure of $V_2O_3(0001)$ films reduced by electron bombardment was also characterized. These surfaces show a coexistence of two phases, a disordered and an ordered one. The ordered phase was shown to be terminated by a single layer of vanadium atoms on top of an oxygen trilayer.

Keywords: $V_2O_3(0001)$, I/V-LEED, surface structure, STM

Zusammenfassung

Vanadiumoxide sind weit verbreitete Katalysatoren in industriellen Reaktionen. Die katalytische Aktivität eines Materials beruht auf seiner Oberflächenstruktur. Während die katalytische Aktivität von $V_2O_3(0001)$ gezeigt wurde, wurde die Oberflächenterminierung von $V_2O_3(0001)$ Filmen umstritten, seit Ionenstreuversuche nahelegten, dass diese Oberfläche von einer Dreifachlage Sauerstoff terminiert ist. Dies steht im Widerspruch zu der zuvor weit verbreiteten Ansicht, dass die Oberfläche von einer vollständigen Lage von Vanadylgruppen belegt ist.

In dieser Dissertation wurde die Oberflächenstruktur von $V_2O_3(0001)$ Filmen mit kombinierten I/V-LEED und STM Messungen bestimmt, um diesen Widerspruch aufzulösen. Die Analyse einer Vielzahl von Präparationen zeigt, dass die Filme von einer kompletten Lage Vanadylgruppen, mit lokalen Defekten, terminiert sind. Die Vanadyl-terminierten Oberflächen können zu Oberflächen mit partieller Vanadyl-Belegung oxidiert werden, welche eine $\left(\sqrt{3} \times \sqrt{3}\right) R30°$ Superzelle aufweisen. Oxidation von Filmen die eine $\left(\sqrt{3} \times \sqrt{3}\right) R30°$ Superzelle haben führt zur Bildung und zum Verdampfen von V_2O_5. Diese Ergebnisse wurden mit übereinstimmenden Ergebnissen von Jan Seifert et al. und Joachim Paier et al. kombiniert, welche durch Streuung von schnellen Atomen bzw. Dichtefunktionaltheorie-Rechnungen erhalten wurden.

Es wurde auch die Oberflächenstruktur von durch Elektronenbeschuss reduzierten $V_2O_3(0001)$ Filmen bestimmt. Diese Oberflächen zeigen eine Koexistenz von zwei Phasen: Eine geordnete und eine ungeordnete. Die geordnete Phase konnte als Einfachlage von Vanadiumatomen auf einer Dreifachlage Sauerstoff identifiziert werden.

Stichwörter: $V_2O_3(0001)$, I/V-LEED, Oberflächenstruktur, STM

Acknowledgements

First and foremost I want to thank Prof. Hans-Joachim Freund for giving me the opportunity to work and study in the Chemical Physics department of the Fritz Haber Institute and for supervising my dissertation. Within the CP department he has created an intense and exciting work environment, stimulating discussions and a big family of fellow scientists. I could not have wished for a better place to conduct my dissertation.

I want to thank Prof. Thomas Risse for supervising my thesis and helping in the organization of the disputation.

I thank Dr. Helmut Kuhlenbeck for never-ending scientific and moral support, no matter what time of night, for countless discussions and pen-and-paper calculations, for implementation of the search algorithms and programming of the spot-tracking software that have enabled my I/V-LEED studies and for the good times at BESSY.

Thanks go out to Matthias Naschitzky who provided technical assistance to me throughout the course of my thesis and without whom I would not have been able to do all the experiments I have done or become as comfortable as I have with the STM-1 UHV-chamber.

I want to thank Prof. Joachim Sauer, Prof. Helmut Winter, Jan Seifert and Joachim Paier for their collaboration and the constructive discussions leading up to our collective publication.

I thank Sergey Levchenko for helping me set up the FHI-aims code used in the DFT calculations on the reduced V_2O_3 surface and for assisting me with DFT calculations and STM simulations.

I want to thank Prof. Georg Kresse for supplying the structural data for the three metal termination.

I want to thank Osman Karslıoğlu for teaching me how to operate surface science machinery.

I thank all fellow members of the CP department, past and present, for the good times, for surface science discussions and also for the fun we had.
I thank all fellow students of the International Max Planck Research School (IMPRS) *Functional Interfaces in Chemistry and Physics* for the interesting discussions and especially for the organization of and participation in our workshop *Micro to Macro* at Castle Ringberg, which was the highlight of my PhD.

I want to thank my parents, Eva and Klaus Feiten, who supported me throughout my thesis.

Finally I want to thank the two most important people in my life:
Xiaolin and Inana Feiten
For their moral support and understanding.
For filling my life with joy.
For all the amazing holidays we have had and we will have.

Contents

Chapter 1

Introduction

1.1 General Introduction

Catalysis is ubiquitous in many industrial scale chemical processes as well as in automotive exhaust treatment. [1–3] A catalyst reduces the activation energy for a reaction, thereby increasing the reaction rate, without being consumed. In heterogeneous catalysis the catalyst is in a different physical state than the reagents. Typically the catalyst is a solid material while educts and products are gaseous or liquid. Metal oxides are widely used in heterogeneous catalysis either as support materials for metallic catalysts or as the catalytically active species themselves. [4–6] Many industrial catalysts are the product of trial and error procedures wherein large numbers of varying catalyst materials are prepared and tested to find the one with the highest activity and selectivity for a desired reaction. They are predominantly employed as powders, pellets or supported nanoparticles which maximizes their surface area and thus the catalytic activity per mass unit of catalyst. The reactivity of a heterogeneous catalyst is determined by the atomic and electronic structure at the catalyst surfaces where the reactions take place. The physical states of industrial catalysts described above preclude them from a number of characterization techniques. Because of this the detailed structure of catalyst surfaces is often unknown. However, in order to understand the catalytic mechanism and to design improved catalytic materials more efficiently the corresponding surface structures have to be determined. In surface science, samples are usually prepared and analyzed in ultra-high vacuum (UHV). This allows the use of characterization techniques such as electron diffraction and photoelectron spectroscopy which require low pressures. Furthermore the low pressures in UHV allow the preparation and characterization of clean samples, unobstructed by contamination from the surrounding atmosphere. To reduce the

structural complexity of systems under study, model catalysts are used. Metal nanoparticles deposited on metal oxide single crystals are model systems which are relatively close to industrial catalysts. [7–9] This kind of system allows the use of techniques such as scanning tunneling microscopy (STM), atomic force microscopy (AFM), photoelectron spectroscopy (XPS/UPS), infrared reflection absorption spectroscopy (IRAS), electron energy loss spectroscopy (EELS), temperature programmed desorption (TPD/TDS) and many others under very controlled conditions. However diffraction based characterization techniques such as low energy electron diffraction (LEED) and surface X-ray diffraction (SXRD) can usually not be applied to nanoparticles on oxide surfaces due to the lack of long range order in the surface structure. Epitaxial growth of metal oxides on single crystal metal substrates creates so called inverse model catalysts which allow extensive characterization of the oxide structure. [10, 11] The surfaces exposed by epitaxially grown films are often also found on the faces of nanoparticles. [12–14] This allows information on adsorption sites and catalytic mechanisms to be transferred from model systems to nanoparticles in applications. Control over which crystal surface is exposed by an epitaxially grown film can, to a certain degree, be gained by changing the substrate or varying the deposition parameters. Additionally oxide surfaces can usually be modified by heating the sample in oxygen or UHV after deposition.

1.2 Vanadium Oxides

Vanadium is a group 5 transition metal with the atomic number 23. It was first discovered in 1801 by Andreas Manuel del Rio in Mexican ores and isolated by Henry Enfield Roscoe in 1869. In compounds it can take the oxidation states +2, +3, +4 or +5. Its occurence in minerals results in a variety of colors. Because of this it was named after the Norse goddess Freyja, nicknamed Vanadis, who is the goddess of love, beauty and fertility and is often depicted wearing a beautiful necklace with variously colored stones. [15]

The numerous oxidation states of vanadium lead to a multitude of different oxide phases. [16] The bulk oxides include VO, V_2O_3, V_3O_5, VO_2, V_6O_{13},V_3O_7, V_2O_5, the Magnéli phases V_nO_{2n-1} with $n = 4 - 8$ and the Wadsley phases $V_{2n}O_{5n-2}$. Out of these V_2O_5 is the thermodynamically stable phase under ambient conditions. [17]

Several vanadium oxides show metal to insulator (MIT) transitions which makes them

frequently studied systems in academic research. VO_2 in particular is interesting for electronic applications and electrical switching. [18,19] The details of these phase transitions, both in VO_2 [20–22] and in V_2O_3 [23–28] are still under debate. While these metal to insulator transitions are bulk properties, it has been shown, that the surface termination has an effect on the appearance of the MIT. [29]

Applications of vanadium oxides include optical switching and light detectors [30], usage in the cathode of lithium ion batteries [31–33], as a buffer layer in polymer photovoltaic cells [34], as a functional material with switchable superhydrophobicity/superhydrophilicity [35] and as part of the anode of supercapacitors [36,37].

By far the most important application of vanadium oxides is in oxidation catalysis. The oxidation of SO_2 to SO_3, a step in the production of sulfuric acid H_2SO_4, is performed over a catalyst consisting of V_2O_5 and K_2O. [15] Even though hundreds of millions of tons of sulfuric acid are produced on a yearly basis and vanadium oxide has been used industrially in this process for almost a hundred years the detailed catalytic mechanism of the oxidation on V_2O_5 is still not known. Other industrial oxidations catalysed by V_2O_5 include naphtalene oxidation to phtalic anhydride, maleic anhydride production from benzene, n-butane or butene and propane oxidation to acrylic acid. [38]

Simard et al. reported on the oxidation of o-xylene to phtalic anhydride over SiC coated with V_2O_5 in 1955. [39] They showed that the pentavalent vanadium oxide is reduced during the catalytic reaction, forming V_2O_4, i.e. VO_2 and an oxide phase with a vanadium oxidation state between +4 and +5: $V_2O_{4.34}$ corresponding to $V_{12}O_{26}$.

Kasoaka et al. showed that a powder catalyst of vanadium oxide coated on TiO_2 catalyzes the removal of SO_x and NO_x from gas streams with water and ammonia. [40] The resulting ammoniumsulfate is fixed on the catalyst and needs to be washed off from time to time.

A review paper on vanadium oxide monolayer catalysts by Bond and Tahir [41] summarizes that vanadium oxide monolayers are stable on TiO_2 and Al_2O_3 but on SiC vanadium oxide monolayers aggregate to form V_2O_5 patches. It also gives an overview over the preparative methods used to achieve VO_x monolayers lists impregnation, grafting, chemical vapor deposition and co-precipitation. The monolayers are effective catalysts for oxidation of o-xylene to phtalic anhydride, ammoxidation of aromatics and reduction of nitric oxide by ammonia but do not catalyse the oxidation of butadiene to maleic anhydride. The review discusses vanadyl (V=O) groups as a prevalent feature in these

monolayers and links these to the catalytic activity.

The group of Israel Wachs studied the selective oxidation of methanol to formaldehyde over a monolayer vanadium oxide catalyst on various supports. [42] They found a significant dependence of the turnover frequency (TOF) on the support employed: vanadium oxide supported on ZrO_2/TiO_2 shows a TOF three orders of magnitude larger than on Al_2O_3 with SiO_2 and Nb_2O_5 supports giving intermediate TOFs. While it had been speculated earlier, that the V=O bond predominant in V_2O_5 might be involved in the catalytic oxidation they found no influence of the V=O bond strength on the activity.

It should be noted that the term "monolayer" in these studies may be inaccurate. There has been a discussion about VO_x monolayer catalysts between Joachim Sauer and Hans-Joachim Freund on one side and Israel Wachs and others on the other side.

A more recent review by Weckhuysen and Keller [3] gives a short overview over vanadium coordination chemistry and describes structure and catalytic activity of supported vanadium oxide films in detail. It stresses the fact that the V=O groups in these films are not the active species in oxidation catalysis.

The fact that these catalytic studies have all been performed on powder samples means that the level of structural information attainable is limited and the precise atomic structure of the vanadium oxide monolayer catalysts is not known. In order to gain detailed information on the structure model systems of vanadium oxides are being studied.

There have been some studies on cleaved vanadium oxide single crystals. Kurtz et al. reported a study on the surface electronic structure and chemisorption on cleaved V_2O_3. [43] However, V_2O_3 cleaved along the (047) crystal plane, exposing a surface that might be less interesting than the principal surfaces, such as for example the (0001) surface. Tepper et al. have studied the (001) surface of a cleaved V_2O_5 single crystal by HREELS, ARUPS and XPS and concluded that the terminal oxygen atoms of the exposed vanadyl groups are stable towards reduction with atomic hydrogen. [44]

However, obtaining high quality single crystals of vanadium oxides is difficult and the epitaxial growth of vanadium oxides on metal or metal oxide single crystal allows more reproducible, cleaner and easier preparation of atomically flat vanadium oxide surfaces.

1.3 Past Research on the $V_2O_3(0001)$ Surface

The present work was motivated by a controversy about the surface termination of $V_2O_3(0001)$ films epitaxially grown under standard UHV conditions. While for years this surface was believed to be terminated by a monolayer of vanadyl (V=O) groups, ion scattering studies published in 2011 and 2012 challenged this view and stated that the surface is instead covered by an oxygen trilayer with few to no vanadyl groups. [45–47] This chapter gives an overview over the publications on the $V_2O_3(0001)$ surface published prior to the present thesis with focus on the atomic structure.

Epitaxial film growth of $V_2O_3(0001)$ on Au(111) was first reported by the Somorjai group in Berkely in 1990. [48] They reported a $\left(\sqrt{3} \times \sqrt{3}\right)$ R30° LEED pattern relative to the LEED pattern of the gold substrate and performed some TPD experiments. In this work the $V_2O_3(0001)$ films were prepared by depositing V at room temperature in UHV and annealing it in oxygen afterwards, repeating this cycle multiple times.

Although some studies have investigated $V_2O_3(0001)$ films prepared on oxide substrates [49–56] this overview focusses on the $V_2O_3(0001)$ films prepared on metal single crystals. Metal single crystal substrates are easier to clean and order by repeated sputtering and annealing than oxide single crystals. They are also obtainable with less contaminations, depending on the metal. Well ordered, epitaxially grown $V_2O_3(0001)$ films have been reported on Au(111) [46–48, 57–66], Cu(100) [67, 68], Pd(111) [45, 46, 69–72], Rh(111) [29, 73–75], Re(0001) [76, 77], $Cu_3Au(100)$ [45, 78, 79] and W(110) [57–59].

In most of these studies the films were prepared by reactive deposition of vanadium, i.e. evaporation of vanadium metal onto the single crystal substrate in an oxygen atmosphere. After deposition the films are annealed in oxygen and finally in UHV to improve ordering of the film.

$V_2O_3(0001)$ crystallizes in the corundum structure and displays rhombohedral symmetry with the space group $R\bar{3}c$. [80] The structure consists of slightly distorted hexagonal layers of oxygen separated by buckled layers of vanadium, see Figure 1.

Cutting the bulk structure of V_2O_3 parallel to the [0001] plane can produce three different surface terminations, henceforth called bulk terminations: A structure with two vanadium atoms in the surface unit cell (henceforth called double metal, DM, termination), a structure with one vanadium atom in the surface unit cell (henceforth called single metal, SM, termination) and a surface terminated by an oxygen trilayer (henceforth called bulk O3

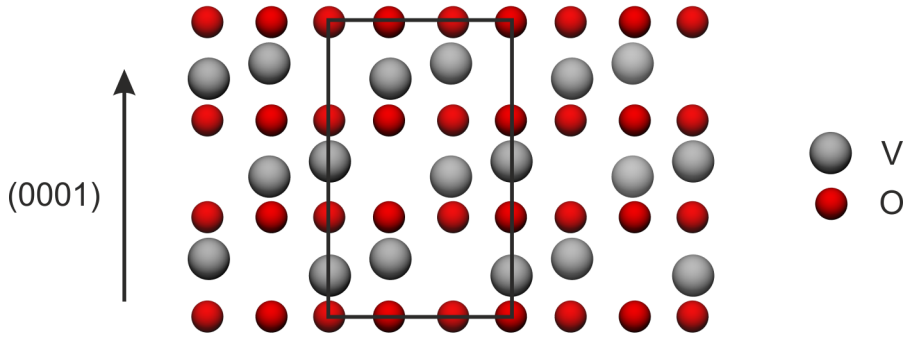

Figure 1: Model of the V_2O_3 bulk structure with the unit cell indicated

termination). These structures are visualized in Figure 2 A) to C).

Czekaj et al. have investigated these bulk terminations of $V_2O_3(0001)$ with density functional theory. [81–83] The structures were modeled by clusters of varying sizes and calculated with local spin density approximation (LSDA) as realized by Vosko, Wilk and Nusair [84] and generalized gradient approximation (GGA) functionals by Perdew, Burke and Ernzerhof (RPBE) [85,86]. Their studies show that bonding in V_2O_3 is a mixture of ionic and covalent bonding. This means that the expected polarity of all three bulk terminations is significantly reduced compared to a purely ionic description. The half metal termination is predicted to be the most stable. Oxygen absorption on top of the vanadium atoms is calculated to produce vanadyl groups V=O with a strong V-O bond. [81]

Kresse et al. have performed DFT calculations on $V_2O_3(0001)$ with the projector augmented wave method [87,88] and the PW91 functional by Perdew and Wang [89,90] using slab models. [91] Their calculations of the surface free energy of $V_2O_3(0001)$ films for various models as a function of oxygen chemical potential leads to a surface phase diagram for $V_2O_3(0001)$ shown in Figure 3.

This phase diagram shows the surface free energy on the vertical axis plotted against the oxygen chemical potential on the horizontal axis for several different surface terminations of the $V_2O_3(0001)$ surface. The thin lines represent surface terminations that have the same unit mesh as bulk V_2O_3. The green line corresponds to the single metal termination. The black line belongs to a vanadyl terminated surface model, see Figure 2 D). This surface results from the addition of an oxygen atom on top of every surface vanadium atom in a single metal termination, as already predicted by Czekaj et al. [81]

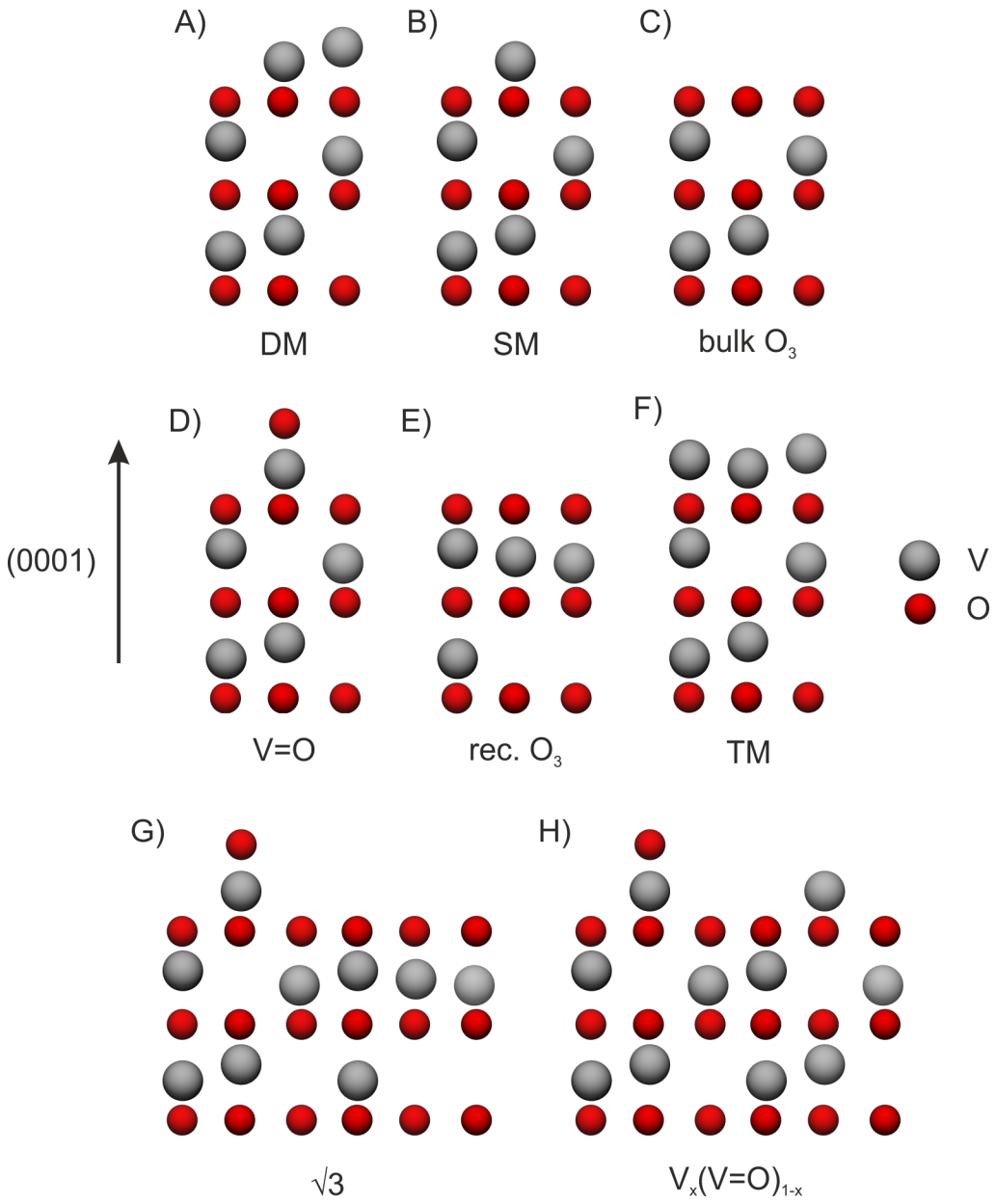

Figure 2: Models of the various V_2O_3 surface terminations discussed in the text

The thin blue line corresponds to a surface terminated by an oxygen trilayer. However, this is not the bulk-like oxygen termination resulting from cutting the bulk structure of V_2O_3 parallel to the [0001] plane as described above. Instead, this reconstructed O3 termination has a structure as shown in Figure 2 E). Below the missing vanadyl groups a vanadium atom moves up into the first subsurface V-layer creating a structure that can also be constructed by placing a VO_2 layer ontop of a single metal terminated V_2O_3 surface. This structure is displayed in Figure 2 E). This reconstruction reduces the polarity of the surface terminated by an oxygen trilayer and in the rest of this thesis the terms

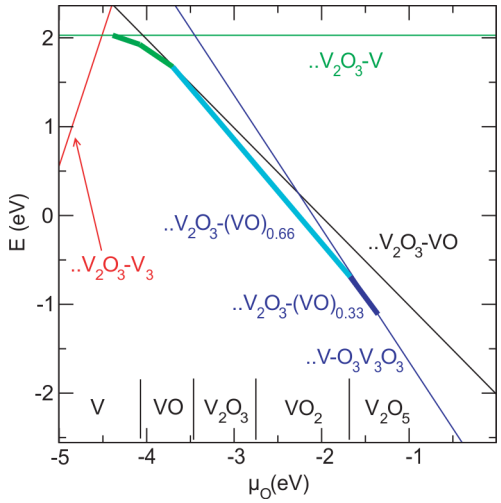

Figure 3: Surface phase diagram for V_2O_3 calculated with DFT; reproduced with permission from [91]

"O3 structure" or "O3 termination" will be used for this reconstructed surface structure. When the bulk O3 surface termination is discussed this will be stated explicitly. The last thin line in Figure 3, colored red, corresponds to a surface structure with three vanadium atoms which we call triple metal (TM) termination, see Figure 2 F). Comparing these four structural models in the phase diagram shows that over a wide range of oxygen chemical potentials, corresponding to typical UHV conditions, the V=O terminated surface is predicted to be thermodynamically favored. In addition, several phases with bigger unit meshes were calculated, to allow partial V=O coverage. The light blue and dark blue thick lines describe surfaces in which one third ($...V_2O_3 - (VO)_{0.66}$, light blue) or two thirds ($...V_2O_3 - (VO)_{0.33}$, dark blue) of the V=O groups are removed from a fully vanadyl covered surface. In these models the sites of missing vanadyl groups are changed in the same way as in the reconstructed O3 termination, i.e. a vanadium atom from the second subsurface layer moves up into the first subsurface layer. A simplified depiction of these partial V=O coverages is shown in Figure 2 G). Finally the thick green line represents mixed phases with partial vanadyl coverage and partial single metal termination ($...V_2O_3 - V_x(VO)_{1-x}$) (Figure 2 H)). This can also be thought of as removing some of the vanadyl oxygen atoms from a vanadyl terminated surface as in Figure 2. The calculations predict that the partially V=O covered surfaces are more stable than the fully vanadyl covered at all oxygen potentials. The authors attribute this to the failure of the DFT calculations to accurately describe the V-O bond-strength which leads to "overbind-

ing" of oxygen; oxygen rich phases are predicted to be more stable than they should. The oxygen chemical potentials at which the metal terminated surfaces (red and green lines) are thermodynamically favored correspond to extremely low oxygen pressures far beyond those achievable in UHV. The O3 termination is predicted to be stable at increased oxygen pressures which are achievable in UHV.

A different DFT study by Todorova et al. comes to similar conclusions. [92] They consider films of varying thickness (one to six vanadium layers) on aluminium oxide Al_2O_3 and find that for the thickest films the results match those by Kresse et al. discussed above.

The Netzer group in Graz prepared thin (between less than 1 monolayer (ML) and 2-3 ML) $V_2O_3(0001)$ films on Pd(111) by reactive deposition of V, i.e. deposition at elevated temperature and in an oxygen atmosphere. [69, 70] This procedure has since been used in most of the studies on epitaxially grown films of $V_2O_3(0001)$ on various metal substrates with very similar parameters. In the following reactive evaporation in O_2 will be assumed as the preparative method for all publications discussed unless explicitly stated otherwise.

Ultrathin films of vanadium oxides show a variety of stoichiometries and structures as demonstrated on Pd(111) [69, 70, 75, 93] and Rh(111) [74, 94]. In order to reduce the structural complexity thicker films are preferable which can be regarded as good models for bulk V_2O_3. While the films prepared in the present thesis are around 100 Å thick, 80 Å thickness as in the work by Schoiswohl et al. [73] or 60 Å which is the lowest thickness reported by Dupuis et al. [57] should also be enough to consider the films as bulk like, in contrast to the ultrathin films with thicknesses of less than 20 Å.

Dupuis et al. have investigated $V_2O_3(0001)$ films with thicknesses between 60 Å and 160 Å deposited on Au(111) and W(110). [57] Infrared reflection absorption spectroscopy (IRAS) and high resolution electron energy loss (HREELS) measurements show a peak at 127 meV which is assigned to the stretching vibration of vanadyl groups based on similar findings for chromyl groups on Cr_2O_3. [95, 96] The vanadyl terminated surface is thermally stable up to 1000 K. XPS measurements show two compononents in each of the $V2p_{3/2}$ and $V2p_{1/2}$ states, one corresponding to bulk like vanadium and another one with higher binding energy assigned to vanadyl V atoms due to its increase when measuring at grazing emission which results in higher surface sensitivity. Near edge x-ray absorption fine-structure measurements also fit a vanadyl terminated structural model. The NEXAFS measurements were expanded and confirmed by simulated NEXAFS [97] and a combined

experimental and theoretical detailed NEXAFS study [61]. Dupuis et al. also showed that the surface can be reduced by electron bombardment and the consequently reduced vibrational signatures of the vanadyl group indicate removal of the vanadyl oxygen atoms. [57] The reduced surface displays increased CO absorption at 90 K and can be restored to a vanadyl termination by exposure to oxygen and subsequent annealing.

STM images of the $V_2O_3(0001)$ surface usually show a hexagonal structure matching a fully vanadyl terminated surface. [73, 75, 78] But there are two interesting exceptions to this: Surnev and coworkers have found coexistence of two different surface phases in STM measurements on a roughly three monolayer thick film of $V_2O_3(0001)$ on Pd(111). [70] Simulated STM images indicate that the two phases represent vanadyl termination and an O3 termination. Niehus et al. have reported STM images showing a distorted hexagonal pattern which they interpret as depicting a double metal termination stabilized by oxygen adsorbates. [79]

Schoiswohl et al. showed that the as-prepared surface can be oxidized by exposure to 5×10^{-6} mbar O_2 at 500 °C. [73] This leads to the appearance of dark depressions in STM images which are interpreted as missing vanadyl groups. These defects form ordered structures with a $\left(\sqrt{3} \times \sqrt{3}\right) R30°$ unit cell relative to the 1×1 vanadyl covered surface. Supercells with either one third or two thirds of the V=O groups missing can be observed and this oxidized phase corresponds to the partially V=O covered surfaces calculated by Kresse and coworkers. [91] In the rest of this thesis the partially V=O covered surface will be referred to as $\sqrt{3}$ structure due to the size of the supercell. LEED images of the $\sqrt{3}$ structure clearly show the additional reflexes.

The vanadyl terminated films can be reduced by two different methods. Deposition of vanadium onto the V=O terminated films leads to a triple metal termination, detected in STM measurements and calculated with DFT. [73, 91] Electron bombardment of the V=O terminated film removes the vanadyl oxygen atoms leading to a single metal termination. [57, 98]

The two types of defects, missing vanadyl oxygen atoms and missing V=O groups, are not easily distinguished in STM measurements. [64] But it has been shown that the dominating type of surface defect, after typical preparations, are missing V=O groups. [66]

The vanadyl covered surface interacts only weakly with a variety of gases. The reduced

surfaces on the other hand interact strongly with several gases and can catalyse reactions. Schoiswohl et al. have demonstrated that while water adsorbs molecularly on the V=O terminated surface dissociation and formation of hydroxyl groups take place on the surface reduced by vanadium deposition. [99] Haija et al. have shown that $V_2O_3(0001)$ films reduced by electron bombardment interact strongly with oxygen and water. [58, 59] The surface reduced by electron bombardment also binds CO, propane and propene more strongly than the vanadyl covered surface. [60] The oxidation of methanol on surfaces reduced by electron bombardment has been studied in detail. On the defect sites created by electron bombardment methanol adsorps dissociatively and is oxidized to formaldehyde. [62, 63, 65]

The first quantitative structure determination of the $V_2O_3(0001)$ surface has been performed by Kröger et al. with photoelectron diffraction (PED). [71] They concluded that the $V_2O_3(0001)$ has a strongly relaxed single metal termination but could neither confirm nor exclude the presence of vanadyl groups. Another PED study by Kröger et al. focussed on hydroxyl groups on $V_2O_3(0001)$ films. [72] They showed that surface hydroxyls form by dissociation of molecular water as well as by reaction with atomic hydrogen.

In 2011 and 2012 several independent ion scattering studies questioned the widespread view that the surface of $V_2O_3(0001)$ films as-prepared under typical conditions in UHV is terminated by vanadyl groups.

Window et al. published a study combining two different ion scattering studies, medium-energy ion scattering (MEIS) and noble gas impact-collision ion scattering spectroscopy with detection of neutrals (NICISS), that both came to the conclusion that the surface is terminated by a reconstructed O3 termination of the type $...V_2O_3 - V - O_3V_3O_3$. [45] The MEIS experiments were performed on $V_2O_3(0001)$ films grown by reactive evaporation of V on Pd(111) and Au(111) while the NICISS measurements were done on $V_2O_3(0001)$ films grown by deposition of vanadium on preoxidized $Cu_3Au(100)$ which was then annealed in oxygen after deposition. The authors rule out a fully vanadyl covered surface but state that up to 20% V=O coverage would be consistent with their results.

Another ion scattering investigation was performed by Seifert et al. via ion beam triangulation. [47] $V_2O_3(0001)$ films were prepared by reactive evaporation of V onto Au(111) under standard conditions. Fast hydrogen atoms were scattered from the vanadium oxide film and the emitted electrons measured as a function of the azimuthal rotation of

the sample. Calculated curves of this function fit the experimental data well for a reconstructed O3 termination but show clear deviations for a vanadyl terminated surface. Annealing of the $V_2O_3(0001)$ surface in UHV, which might be expected to reduce the surface, did not change the ion beam triangulation curves.

Finally another publication by Window et al. discussed the MEIS experiments in detail and introduced a new theoretical phase diagram based on DFT calculations as well as simulated STM images. [46] The phase diagram is based on calculations by Todorova et al. for $V_2O_3(0001)$ films on Al_2O_3. [92, 100] Its results are similar to the phase diagram by Kresse et al. [91]: At the highest oxygen chemical potentials a reconstructed O3 termination model is predicted; reducing the oxygen chemical potential leads to addition of V=O groups occupying one third of the possible sites and two thirds of those sites at even lower oxygen potentials. Even more reducing conditions are predicted to produce mixtures of V=O and V termination. While the authors discuss the overestimation of oxygen binding in the PW91 functional employed they conclude that the theoretical phase diagram is in support of the O3 termination. Simulated STM images are presented for V=O, as well as bulk and reconstructed O3 terminations. The simulations for vanadyl termination correspond well to the hexagonal arrangement of round protrusions found in typical STM images while the triangular features that calculations predict for both O3 terminations have so far only been observed by Surnev et al. [70] as discussed above.

1.4 Aim of the Present Thesis

The goal of the present thesis is the surface structure determination of $V_2O_3(0001)$ films prepared on Au(111) in ultra-high vacuum.

To determine the surface structure, I/V-LEED and STM measurements are combined.

I/V-LEED as a diffraction technique gives information averaged over macroscopic surface areas and allows accurate determination of interatomic distances or lattice constants. However, due to the fact that I/V-LEED is based on long-range order, it provides only averaged information on local defects.

'For instance, it has become clear that a surface showing clear and sharp diffraction spots in low-energy electron diffraction (LEED) experiments can still appear highly defective when imaged by STM.' [101]

STM on the other hand is a local technique that gives real space information. It can yield atomically resolved structural information on local disorder and defects. But it is often not clear if the structures imaged by STM are representative of the whole sample. Structural parameters such as interatomic distances and lattice constants obtained by STM also are not very accurate due to hysteresis and creep of the piezoelectric motors used in the STM as well as thermal drift. STM does also not have chemical sensitivity, although scanning tunneling spectroscopy can help in the characterization of atomic species.

'Therefore, only a combination of local probes and averaging techniques can yield a complete picture.' [102]

In order to be able to directly correlate STM and I/V-LEED data the two methods are performed in direct succession on the same preparation.
Experiments were conducted to determine if there is a coexistence of vanadyl terminated and O3 terminated surface areas. Or if possibly both, vanadyl termination as well as O3 termination, can be prepared under different preparation conditions. Finally the structure of the surface reduced by electrons was also to be determined in order to complete the understanding of the relevant surfaces in the catalytic studies of $V_2O_3(0001)$ performed in our group. [58–60, 62, 63, 65]

Chapter 2

Experimental Methods

A central aspect of the investigation of model systems is the sample's cleanliness. In a UHV system this depends on three parameters, assuming that the sample is clean directly after preparation: the gas pressure in the system, the time between preparation and analysis and the sticking coefficient of gases on the sample. The sticking coefficient can be any number between 0, which would mean that no gas molecules stick to the sample, and 1 which implies that every single gas molecule hitting the sample sticks to it. The sticking coefficient is a property of the combination of sample and gas and thus different surfaces have very different sticking coefficients for different gases. Without knowledge of the sticking coefficient(s) it is impossible to calculate the surface coverage using pressure and time. But using a sticking coefficient of 1 allows calculation of an upper boundary for the maximum coverage that can possibly result under given conditions. In surface science a gas dose is commonly measured in Langmuir L. One Langmuir L corresponds to an exposure of 1×10^{-6} torr for one second. Using a sticking coefficient of 1, 1 L exposure leads to adsorption of one monolayer (ML) of gas molecules on the surface. This leads to the times of exposure needed to form one monolayer depending on the pressure given in Table 1. Even at 1×10^{-9} mbar which is often considered the upper end of the pressure range called UHV it is hard to investigate a clean sample since the specimen will be covered by a significant amount of adsorbed gas within minutes. In order to have a clean sample for an extended period of time, working in the 1×10^{-10} mbar pressure range is necessary.

The experiments were performed in a commercial UHV system from Omicron. It consists of one UHV chamber for sample preparation and analysis, a transfer system with high pressure cell allowing the introduction/removal of samples and STM tips into/from the chamber without venting the system and a gas inlet system. The UHV chamber is

pressure in mbar	**time until ML coverage**
1×10^{-5} mbar	0.1 s
1×10^{-6} mbar	1 s
1×10^{-7} mbar	10 s
1×10^{-8} mbar	100 s $\sim$ 1.7 min
1×10^{-9} mbar	1000 s $\sim$ 17 min
1×10^{-10} mbar	10 000 s $\sim$ 2.8 h
1×10^{-11} mbar	100 000 s $\sim$ 28 h

Table 1: Dependence of time to reach one monolayer coverage on the pressure

evacuated with a turbomolecular pump, an ion pump and a titanium sublimation pump, resulting in a base pressure of $\sim 2 \times 10^{-11}$ mbar. The high pressure cell is pumped by another ion pump. Furthermore a scroll pump and a second turbomolecular pump allow evacuation of the gas inlet system and/or the high pressure cell. The UHV chamber contains the manipulator, a sputtergun for ion bombardment, an EFM-3T evaporator for physical vapor deposition of vanadium, a LEED system with channelplate detector (abbreviated MCP for microchannel plate), an X-ray gun with two anodes, Mg and Al, a hemispherical analyzer for XPS, an Omicron STM-1 housed in a side chamber of the main chamber, that can not be isolated from the main chamber, a carousel for storing samples and STM tips, two wires for annealing of STM tips and a tungsten filament for electron bombardment. Additional facilities within the UHV system, that were not used in this work, include a quadrupole mass spectrometer and additional evaporators. The manipulator houses a receptacle which can hold sample crystals or STM tips mounted on sample holders. This is used during preparation and all characterization methods except for STM. Close to the sample holder a quartz crystal microbalance (QMB) is included within the manipulator, which allows calibration of the rate of evaporation of metal evaporators. A tungsten filament is mounted behind the sample holder for sample heating. The sample holder and sample can be cooled with gaseous nitrogen which in turn is cooled with liquid nitrogen outside of the UHV system. The manipulator can move in three directions and it can be rotated about its axis, to reach different sample positions for transfer and the various preparative and analytical methods.

2.1 Sample Setup and Preparation

The $V_2O_3(0001)$ films prepared in the context of this thesis were deposited onto an Au(111) single crystal. Figure 4 shows a picture of the Au(111) crystal mounted on the sample holder. The Au(111) crystal which was purchased from MaTeck, is fixed on a molybdenum plate with two thin molybdenum wedges that press down on the crystal inside two slits at the sides. Two wires, one chromel and one alumel, are spotwelded onto one of the wedges and contact the sample crystal, acting as a type K thermocouple to determine the sample temperature. The whole sampleholder, including the sample, can be inserted into a receptacle on the manipulator and the electrical contacts at the bottom of the sample holder are connected to feedthroughs in the UHV chamber. Thus, the sample can be put on ground potential for LEED or XPS measurements as well as ion bombardment. When heating the sample or during the deposition of vanadium a high voltage is applied through the same contacts.

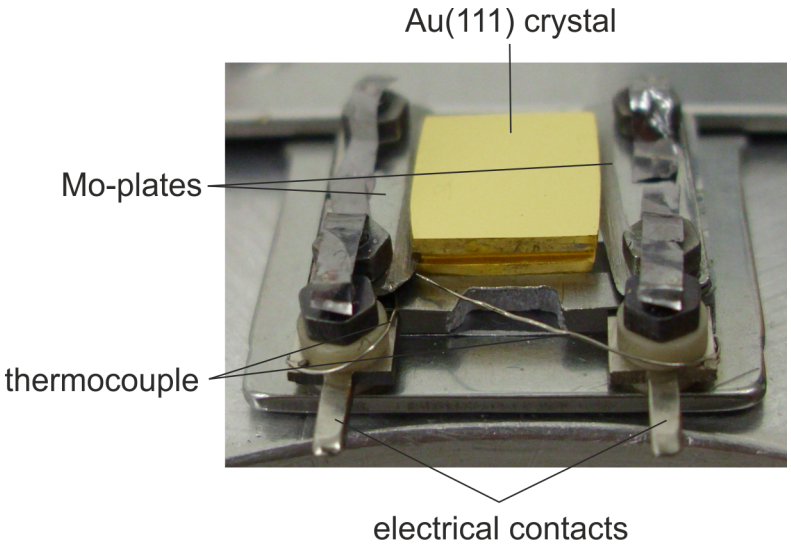

Figure 4: Sample Setup

The Au(111) single crystal used as a substrate for film growth was cleaned via bombardment with Ar^+ ions and subsequent annealing. Two different sputterguns were used with the following settings: An Omicron ISE10 Sputter Ion Source was used with an applied voltage of 1 kV and an Argon pressure of 3.5×10^{-6} mbar. A Specs IQE 11-A sputtergun was used with an applied voltage of 3 kV and an Argon pressure of 2×10^{-5} mbar. Within the sputtergun the elemental Ar gas is ionized and the resulting Ar^+ ions are accelerated towards the sample by the voltage applied. Typical sputter currents were about 10 µA to

15 µA. For sample heating a positive voltage of 500 V was applied to the sample while the tungsten filament for heating was on ground potential.

For film deposition the clean Au-crystal was heated to the desired temperature and the chamber filled with oxygen (typically around 2×10^{-7} mbar) before vanadium was evaporated onto the sample. Deposition rates were ~ 0.75 Å min^{-1} with deposition times of around 2 h giving films of roughly 100 Å thickness.

2.2 Low Energy Electron Diffraction (LEED)

Low energy electron diffraction (LEED) was discovered by Davisson and Germer in 1927 when they performed experiments on a nickel crystal. [103] Davisson and Thomson received the nobel prize in 1937 *"for their experimental discovery of the diffraction of electrons by crystals"*. An electron beam is directed at a crystalline sample and the electrons are diffracted at the crystal lattice. The diffracted beams are made visible on a phosphorous screen and the diffraction pattern on the screen can be recorded with a camera. A schematic drawing of the experimental setup for LEED is shown in Figure 5. Visual inspection of the diffraction pattern allows determination of the symmetry of the surface unit cell and can help judge the degree of order of the sample surface (better ordering leads to less background and sharper diffraction spots). Quantitative structure determination with LEED involves recording diffraction patterns at various electron energies and plotting the spot intensity (I) as a function of the kinetic energy or accelerating voltage (V) giving rise to the term I/V-LEED (often also written LEED-I/V). The thus obtained experimental curves have to be compared with computations of I/V-curves for trial structures and the trial structures have to be varied in repeating calculations until the agreement between experiment and theory is good enough.

In LEED, electrons are emitted from the electron gun with kinetic energies ranging from about 20 eV up to 500 eV. They are diffracted at the sample according to Bragg's law:

$$2dsin\theta = n\lambda \tag{1}$$

d is the distance between two layers in the sample crystal, θ is the angle between the sample and the incoming beam, n is an integer number and λ is the wavelength of the electron. See Figure 6 for a visualization of the geometry involved. Constructive interference occurs

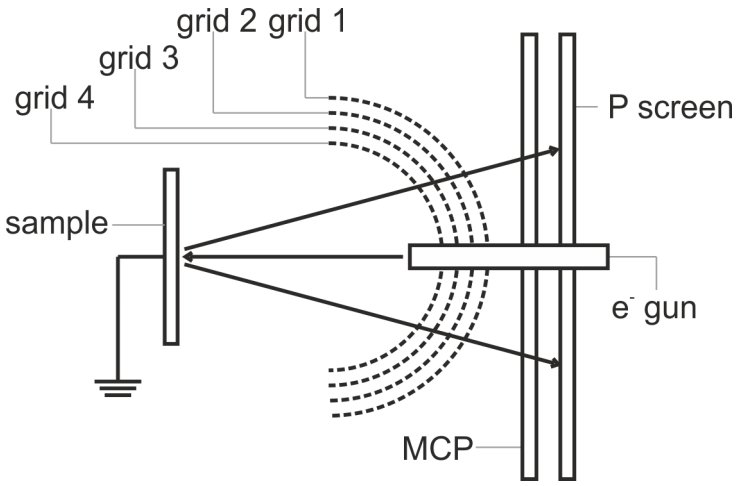

Figure 5: Experimental setup of a microchannel plate LEED system

when Bragg's law is fulfilled, i.e. when the path difference $2dsin(\theta)$ between electrons reflected from subsequent layers is an integer multiple of the electron wavelength, and can only be achieved if the wavelength used is equal to or smaller than the lattice spacing in the sample. With $\lambda = h/\sqrt{2mE}$ the wavelength of low energy electrons ranges roughly from 2.7 Å at 20 eV to 0.5 Å at 500 eV, which is well suited for diffraction at samples with interlayer distances in the Ångstrøm range (typical interlayer distances in metals and metal oxides are in this range).

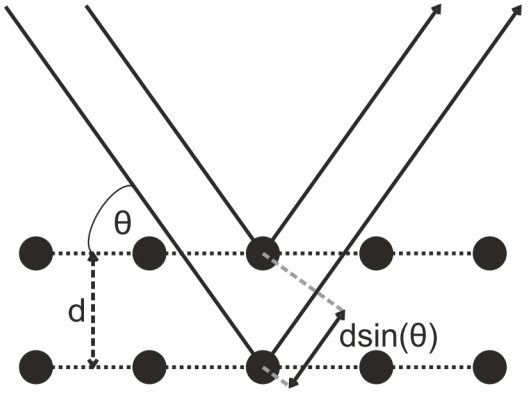

Figure 6: Geometry involved in Bragg's law

At this point it is instructive to introduce the concept of the reciprocal lattice as the reflexes seen on the phosphorous screen are an image of the sample surface in reciprocal space. The principal vectors $\vec{a}_1^*$, $\vec{a}_2^*$ and $\vec{a}_3^*$ of the reciprocal lattice are constructed through

$$\vec{a}_1^* = 2\pi \frac{\vec{a}_2 \times \vec{a}_3}{\vec{a}_1 \cdot (\vec{a}_2 \times \vec{a}_3)}; \quad \vec{a}_2^* = 2\pi \frac{\vec{a}_3 \times \vec{a}_1}{\vec{a}_2 \cdot (\vec{a}_3 \times \vec{a}_1)}; \quad \vec{a}_3^* = 2\pi \frac{\vec{a}_1 \times \vec{a}_2}{\vec{a}_3 \cdot (\vec{a}_1 \times \vec{a}_2)} \tag{2}$$

from the principal vectors $\vec{a}_1$, $\vec{a}_2$ and $\vec{a}_3$ of the real space lattice. The factors 2π are not used in crystallography but are helpful in surface physics. Each principal vector of the reciprocal lattice $\vec{a}_i^*$ is orthogonal to two principal vectors of the real space lattice so that

$$\vec{a}_i^* \cdot \vec{a}_j = 2\pi\delta_{ij} \tag{3}$$

with $\delta_{ij} = 1$ when $i = j$ and $\delta_{ij} = 0$ when $i \neq j$. Points in the reciprocal lattice are mapped by reciprocal lattice vectors $\vec{g}$ with

$$\vec{g} = \nu_1\vec{a}_1^* + \nu_2\vec{a}_2^* + \nu_3\vec{a}_3^* \tag{4}$$

where ν_1, ν_2 and ν_3 are integers.
If we describe the incoming wave with wavevector $\vec{k}$ by $exp\left[i\vec{k}r\right]$ and the scattered wave with wavevector $\vec{k}'$ by $exp\left[i\vec{k}'r\right]$ the scattering amplitude F becomes

$$F = \int dV n(r) exp\left[i\left(\vec{k} - \vec{k}'\right) \cdot r\right] = \int dV n(r) exp\left[-i\Delta\vec{k} \cdot r\right]. \tag{5}$$

$n(r)$ is the local electron concentration and V is the volume of the sample.
The scattering vector $\Delta\vec{k}$ is defined through

$$\vec{k} + \Delta\vec{k} = \vec{k}'. \tag{6}$$

It can be shown that the scattering amplitude F is only significantly different from zero when the scattering vector is equal to a reciprocal lattice vector. This defines the scattering condition

$$\Delta\vec{k} = \vec{g}. \tag{7}$$

Equation 7 can be reformulated into the Laue equations by successively taking the scalar product of both sides with the principal vectors of the real space lattice $\vec{a}_1$, $\vec{a}_2$ and $\vec{a}_3$:

$$\vec{a}_1 \cdot \Delta\vec{k} = 2\pi\nu_1 \quad \vec{a}_2 \cdot \Delta\vec{k} = 2\pi\nu_2 \quad \vec{a}_3 \cdot \Delta\vec{k} = 2\pi\nu_3 \tag{8}$$

In order to fulfill the reflection condition $\Delta\vec{k}$ has to lie on the intersection of three cones defined through the Laue equations. In LEED the three dimensional symmetry of the crystal is broken by the crystal surface resulting in two dimensional symmetry. This simply means, that only two Laue conditions, corresponding to the two principal vectors

of the unit mesh, must be fulfilled for diffraction. The reciprocal lattice is replaced by a reciprocal net in two dimensions. The principal vectors of the reciprocal net $\vec{c}_1^*$ and $\vec{c}_2^*$ are defined through the vectors of the surface mesh $\vec{c}_1$ and $\vec{c}_2$:

$$\vec{c}_1 \cdot \vec{c}_2^* = \vec{c}_2 \cdot \vec{c}_1^* = 0; \quad \vec{c}_1 \cdot \vec{c}_1^* = \vec{c}_2 \cdot \vec{c}_2^* = 2\pi \tag{9}$$

Again the surface physicist's notation has been used, crystallographers would replace 2π with 1. The points of the reciprocal net are then described by

$$\vec{g} = h\vec{c}_1^* + k\vec{c}_2^*. \tag{10}$$

The points of the reciprocal net can be imagined as rods in the third dimension. These rods are of infinite extent and normal to the surface. The diffraction condition can then be visualized through the Ewald sphere depicted in Figure 7. The incoming wavevector $\vec{k}$ is drawn so that it ends at a surface atom and a sphere with radius $2\pi/\lambda$ is drawn around the origin of $\vec{k}$. The Laue conditions are fulfilled for all points on the Ewald sphere that intersect a reciprocal net rod. The resulting diffracted beams $\vec{k}'$ are labelled $\vec{k}'_{h,k}$ according to the indices h, k of the corresponding reciprocal net vector. In Figure 7 the back scattered beams are $\vec{k}'_4$, $\vec{k}'_5$, $\vec{k}'_6$ and $\vec{k}'_7$.

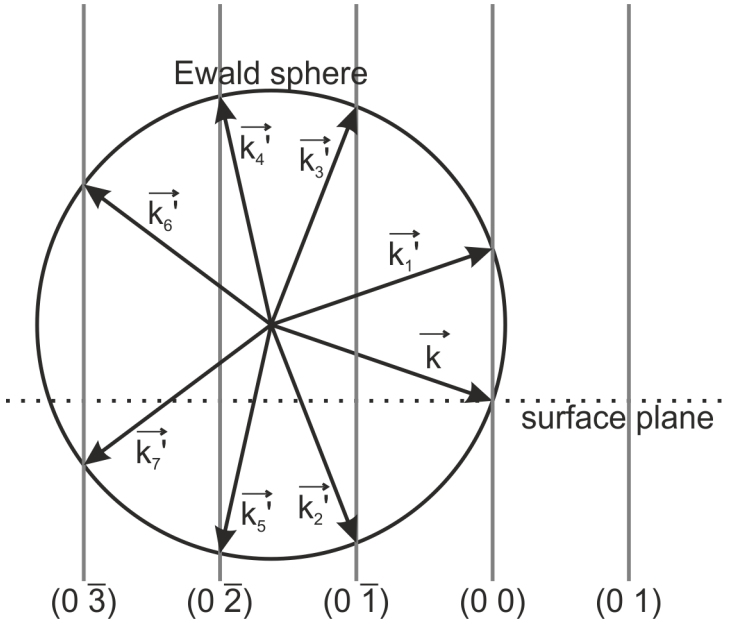

Figure 7: Ewald sphere construction for diffraction of $\vec{k}$

The backscattered electrons then travel through three or four grids before reaching the phosphorous screen. Grid four is grounded to keep the region where the electrons travel

to and from the sample free of electrical fields while grid one is grounded to shield the high voltage applied to the phosphorous screen and the microchannel plate. Grids two and three (in some LEED systems there is just one grid instead of two) are set to a potential $E = -E_{kin} + \Delta V$ where E_{kin} is the kinetic energy of the electrons and ΔV is between 0 V and 10 V. This potential blocks most of the inelastically scattered electrons from reaching the detection system. The microchannel plate (MCP) between the grid-system and the detection screen acts as an electron multiplier. It allows operation of the LEED gun at a lower filament current, compared to LEED systems without MCP, which reduces the radiation damage suffered by the sample during the measurement. While many LEED systems use a thoriated tungsten (WTh) filament as the electron source, lanthanum hexaboride, LaB_6, is preferred for I/V-LEED measurements as it can be operated at a lower temperature resulting in much lower stray light levels, i.e. a reduced background, compared to WTh.

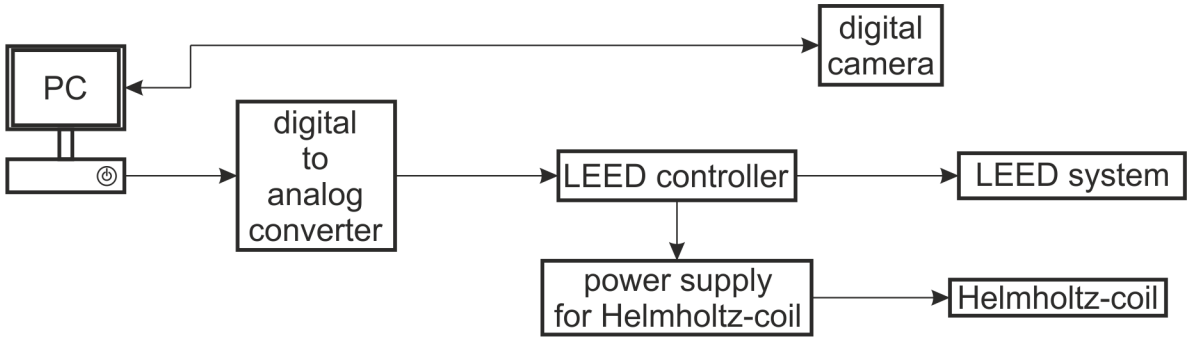

Figure 8: Schematic drawing of the different electronic components for the LEED measurement and their connectivity

Figure 8 shows a schematic drawing of the electronic setup for I/V-LEED measurements. A computer program sets the beam energy by sending a voltage signal to the LEED controller via a digital to analog converter (DAC). The LEED controller then sets the corresponding voltages at the LEED system and simultaneously sends a signal proportional to the beam energy to the power supply for the Helmholtz-coil described in detail below. The diffraction pattern on the phosphorous screen is recorded with a computer controlled digital camera. Integration of camera control and setting of the beam energy into the same software allows automation of the recording of the diffraction pattern at varying beam energies. The integrated spot intensity is then evaluated for all diffraction spots and energies leading to the intensity over voltage (I/V) curves.

An additional experimental requirement when performing I/V-LEED measurements is normal incidence of the electron beam to the sample. While it is theoretically possible to calculate I/V-curves for off-normal incidence this is not possible with the program package used in this thesis (SATLEED [104]) and it would also require precise knowledge of the off-normal angle as well as significantly increased computational cost. Measurements of the earth's magnetic field inside the UHV chamber showed that, while the horizontal magnetic field along the manipulator axis is small (1 µT), there is a significant component (45 µT) in z-direction. In order to compensate for this magnetic field a Helmholtz-coil was mounted onto the chamber as depicted in Figure 9. It consists of two coils of 15 loops each. The current in both coils flows in the same direction resulting in a homogeneous magnetic field between the two coils. The current supplied to the coils is controlled based on the beam energy of the LEED electron gun. Setting an offset and gain for this energy dependent current allows compensation of small angular misalignments as well as cancellation of the earth's magnetic field around the sample at all energies resulting in consistent normal incidence. The fulfillment of the normal incidence condition can be checked by comparing the I/V-curves of symmetry equivalent spots. At normal incidence symmetry equivalent spots will have maxima and minima at the same positions while at off-normal incidence the position of the same minimum or maximum will change between I/V-curves of different symmetry equivalent beams. When the electron beam angle of incidence varies significantly from the surface normal the overall shape of the I/V curves also changes.

Electrons interact strongly with matter making LEED an intrinsically surface sensitive technique. The mean free path of electrons travelling through solid materials depends on the electron's kinetic energy and to a limited degree on the material. This is reflected in the universal curve for the electron mean free path. One visualization of it is shown in Figure 10. The electron mean free path has a minimum at about 50 eV with a value of 5 Å, and is smaller than 10 Å over the complete range of electron kinetic energies usually employed in LEED measurements. This also means that LEED does not just probe the topmost layer of atoms but actually probes a surface volume including several layers.

On the next pages the evaluation of I/V-LEED data will be described, including details of data processing, the calculation of I/V-curves, the comparison between experimental and theoretical curves and the search algorithms used to optimize the trial structure for

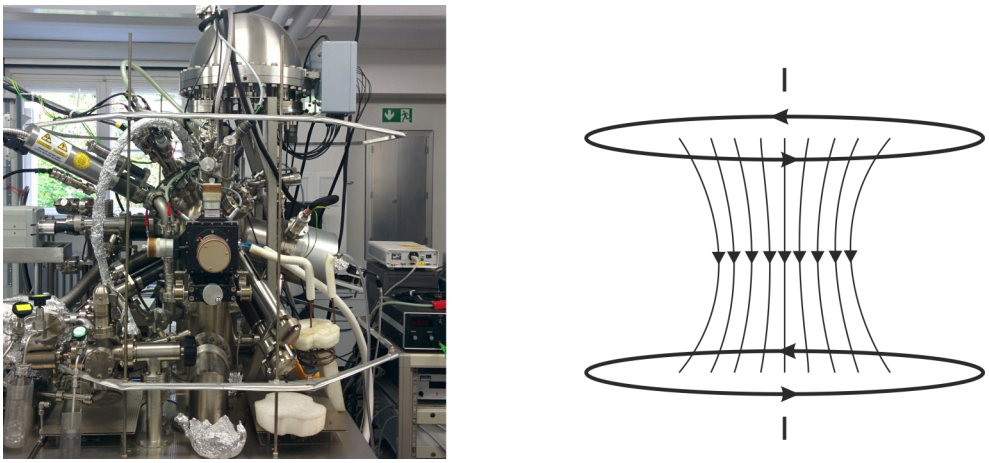

Figure 9: Photograph of the UHV system with Helmholtz-coil on the left and schematic drawing of the Helmholtz-coil inlcuding the field lines of the resulting magnetic field on the right

which I/V-curves are calculated.

After the I/V-LEED measurement is finished a computer program is used to integrate the spot intensities yielding an I/V-curve for every diffraction spot measured. The I/V-curves for symmetry equivalent spots are then added up to improve the signal to noise ratio and the resulting curves are smoothed to remove experimental noise. Additionally two corrections are applied to the experimental data, one correcting for the beam energy dependence of the electron current to the sample and one for the beam energy dependence of the sensitivity of the MCP. The resulting set of symmetry inequivalent beams is used in the comparison with theoretical curves in the following calculations.

The basic procedure for the structure determination with I/V-LEED is displayed in Figure 11. An initial trial structure has to be guessed. The resulting I/V-curves for this trial structure are calculated and then compared with the experimental data via a reliability (R) factor. An R-factor of 0 results if experimental and theoretical curves are identical. An R-factor of 1 describes no-correlation between experiment and theory while an R-factor of 2 means experiment and theory are anti-correlated (which in practice corresponds to computational errors either in the code or in the input). Convergence is reached when the R-factors of several subsequent calculations do not differ significantly. If convergence is not yet reached the trial structure is modified, and the cycle repeated. The search algorithms employed have a limited capability to escape local minima. This means that the structure and R-factor of the converged calculation depend on the initial trial structure. Because

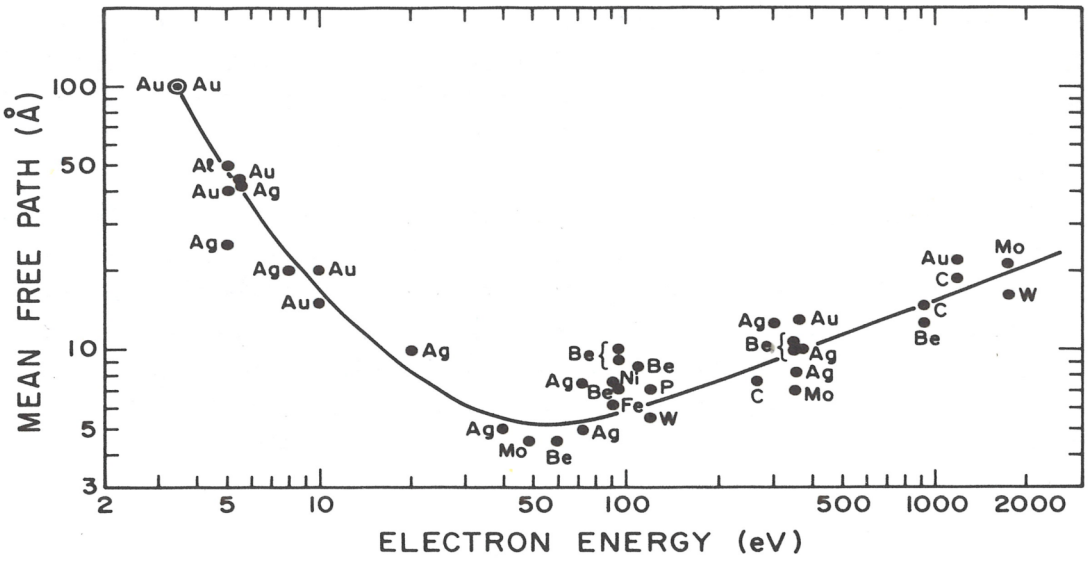

Figure 10: Universal curve for the electron mean free path; reproduced with permission from [105]

of this several different complete cycles as depicted in Figure 11 and described above are performed with varying initial trial structures.

I/V-curve calculation

Because electrons interact strongly with matter, multiple scattering must be considered when quantitatively evaluating LEED data. This is done with dynamical LEED theory. In contrast to this, Kinematic LEED theory, which is similar to the theory used in explaining x-ray diffraction and is a single scattering approach, can be used to gain information about surface morphology in spot profile analysis (SPA) LEED and will not be discussed further here since it is not used in this work.
The theoretical details of the calculation of I/V-curves are treated in *Surface Crystallography by LEED* by Van Hove and Tong [106] in the context of the SATLEED program used within this thesis. A general and detailed description of LEED theory can also be found in *Low Energy Electron Diffraction* by Pendry [107].

While I/V-LEED curves usually have a relatively complicated structure, it is possible to understand how they result from some basic physical principles described in the following. Let us first assume a one dimensional system with atoms evenly spaced from $x = 0$ to $x = \infty$. An incoming wave $exp(ikx)$ with wavevector k is incident upon the system

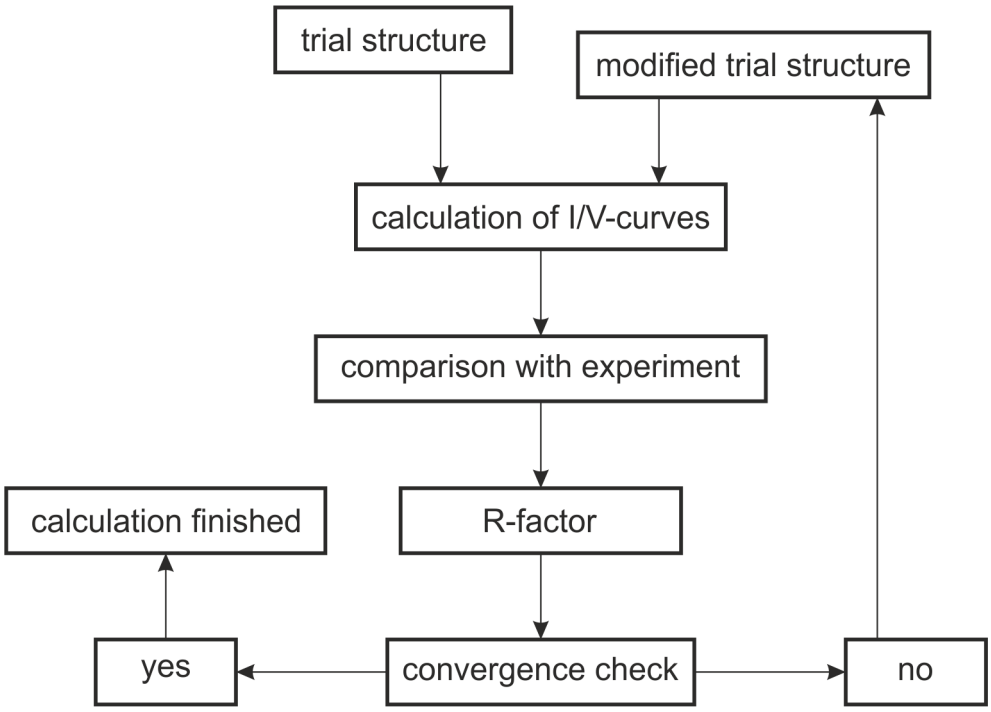

Figure 11: General scheme for the logical steps involved in structure determination with I/V-LEED

from $x = -\infty$. This scattering of the wave by each atom can be described by complex coefficients of reflection r and transmission t. These coefficients determine the proportion of the incoming wave that is reflected or transmitted during a single scattering event.
In the limit of weak scattering, corresponding to kinematic theory, the absolute value of the reflection coefficient $|r|$ is very small while the value for the transmission coefficient $|t|$ is approximated as 1. This leads to a reflection of the incoming wave $exp(-ikx)$ by the one-dimensional crystal as follows:

$$\sum_{j=0}^{\infty} re^{ik2aj}e^{-ikx} = \frac{r}{1-e^{ik2a}}e^{-ikx} \tag{11}$$

with a being the lattice parameter of our one-dimensional crystal. The factor $exp(ik2aj)$ describes the damping of the wave by successive atoms. This leads to small intensity of the reflected wave except for wavevectors which fulfill the Bragg condition $k2a = n2\pi$. The corresponding Bragg peaks have infinite amplitude because the transmission coefficient has so far been approximated as 1. Reducing the transmission coefficient to $|t| < 1$ changes the amplitude of the wave reflected by the atom at $j+1$ from $rexp(ik2aj)$ to $rt^{2j}exp(ik2aj)$ resulting in the following equation instead of 11:

$$\sum_{j=0}^{\infty} rt^{2j} e^{ik2aj} e^{-ikx} = \frac{r}{1 - t^2 e^{ik2a}} e^{-ikx} \tag{12}$$

This results in Bragg-peaks at the same energies as before but which are now of finite height.

So far only single scattering has been considered, i.e. at any single atom the wave is either reflected or transmitted and only the transmitted waves are allowed to be reflected afterwards. But in order to describe the scattering process completely, reflections of reflected waves have to be taken into account. For an exact description all multiple reflections to infinite order have to be calculated. This is realized by treating the electrons as Bloch waves within band structure theory. It changes neither the positions nor the peak-widths of the diffraction peaks but truncates them at the top resulting in flat peaks with a height of 1. These flat peaks correspond to band gaps: Within the band gap, i.e. the flat top of the peak, total reflection occurs, while within the bands, i.e. the region between peaks, only partial reflection and inelastic scattering occur resulting in small intensities.

So far a real transmission coefficient t has been used. In reality however t is usually complex. Introducing this change does not modify the shapes of reflection peaks but affects their position by changing the condition for reflection to

$$k2a + arg(t) = n2\pi. \tag{13}$$

The phase of the transmitted wave is changed by a phase shift $arg(t)$. This phase shift resulting from transmission of the electron wave through an atom has two components. An inner potential corresponding to a shift of the energy axis by a fixed amount (only weakly depending on the electron energy) and multiple scattering within the atom due to resonance effects which show a strong energy-dependence. These effects are introduced into the LEED calculations via energy and element specific phase shifts provided by independent calculations. The inner potential within the atoms results in a shift of the peak positions to lower energies compared to kinematic theory. The intra-atomic resonances scatter the peak positions about the positions already corrected for the inner potential, typically resulting in even lower energies for the peaks.

The peak width of the peaks in I/V-LEED curves depends on the penetration depth of the electrons. Since each atom reflects a portion $|r|$ of the incoming wave, there is a

number of atoms N that will reflect all of the wave with $N|r| = 1$. With the distance between atoms a as above the penetration depth then becomes $Na = a/|r|$. Two atoms produce peaks seperated by $\Delta k \sim \pi/a$. A chain of $N+1$ sources produces N peaks with seperation $\Delta k \sim \pi/(Na)$ between two peaks. The peak width $2\Delta k$ is roughly half that separation: $2\Delta k \sim \pi/(2Na)$. This means the energy width of the diffraction peaks is

$$2\Delta E = 2\frac{\hbar^2}{m_e}k\Delta k \sim \frac{\hbar^2}{m_e}k\frac{\pi}{2}\frac{1}{Na} = \frac{\pi\hbar}{2m_e}k\frac{|r|}{a}. \tag{14}$$

Replacing the penetration depth Na with the electron mean free path λ gives

$$2\Delta E \sim \frac{\pi\hbar^2}{2m_e}\frac{k}{\lambda} \sim 2V_{0,i}. \tag{15}$$

$V_{0,i}$ is the imaginary part of the complex electron energy which broadens sharp peaks in the spectra to a width of $2V_{0,i}$. At very low electron energies ($E_{kin} << 50eV$) total reflection becomes relevant leading to peak widths much larger than $2V_{0,i}$, but at the electron energies used in this work (50 eV to 500 eV) inelastic damping described by $2V_{0,i}$ dominates peak widths.

A three-dimensional treatment of the scattering process, instead of the one-dimensional case discussed so far, leads to an increase in the number of beams the diffracted electrons can travel in as a result of the periodicity in three dimensions. The bulk structure of crystals is periodic in three dimensions yielding three-dimensional reciprocal lattice vectors. In LEED the symmetry of the crystal in one direction is broken by the surface. This means the diffracted beams are characterized by two-dimensional lattice vectors $\vec{g}$ which are visualized on the phosphorous screen of the LEED system. The beams are well defined if the surface is ordered and their positions on the screen depend only on the unit-mesh, i.e. the two-dimensional unit-cell, and the electron wavelength. Every layer in the crystal diffracts an incoming beam $\vec{g}$ into an outgoing beam $\vec{g'}$ with reflection coefficient $r_{\vec{g'},\vec{g}}$ or transmission coefficient $t_{\vec{g'},\vec{g}}$. Each beam has a wavevector $k\left(\vec{g}\right)$ and each wavevector has a component $k_\perp\left(\vec{g}\right)$ perpendicular to the surface. This results in the diffraction condition

$$k_\perp\left(\vec{g}\right)\cdot a + arg\left(t_{\vec{g},\vec{g'}}\right) + k_\perp\left(\vec{g'}\right)\cdot a + arg\left(t_{\vec{g'},\vec{g'}}\right) = n\cdot 2\pi \tag{16}$$

with a being the distance between the layers. This equation holds for single scattering theory and the different reflected beams have only intensity maxima obeying eq. 16. However strong multiple scattering creates additional maxima which can be understood

in terms of intermediate beams. The beam incident on the sample, $\vec{0}$, can scatter into an intermediate beam $\vec{g_i}$. This intermediate beam can then scatter into a beam $\vec{g'}$. Both scatterings, $\vec{0}$ to $\vec{g_i}$ and $\vec{g_i}$ to $\vec{g'}$ will at some energies fulfill eq. 16 leading to additional maxima in $\vec{g'}$ not explained by single scattering from $\vec{0}$ into $\vec{g'}$.

For I/V-LEED calculations a "muffin-tin model" is used to represent the potential in the crystal. The muffin-tin potential consists of two parts. Spherical functions of finite extent are placed at the positions of the atoms so that neighbouring spheres touch but do not overlap. In between those spheres the potential is assumed to be constant. This constant potential is called the inner potential V_0 and is complex with real part $V_{0,r}$ and imaginary part $V_{0,i}$. The real part $V_{0,r}$ has a slight energy dependence which is neglected and excerts a constant phase shift on the waves travelling through it. The imaginary part $V_{0,i}$ reproduces inelastic scattering resulting from processes such as single-electron and plasmon excitations. The form of the potential at the interface between surface and vacuum is not well understood but three different events can in theory happen at this interface: Refraction of any wave passing through the surface because momentum parallel to the surface is conserved while momentum perpendicular to the surface is changed, reflection by the surface (only if the electron has an energy not much larger than $V_{0,r}$) and diffraction if the interface potential has structure parallel to the surface. In the LEED code refraction is calculated while the latter two effects are neglected. Within the muffin-tin potential the electron wavefunction can be expressed as linear combinations of plane waves or spherical waves. Both of the representations have advantages in different situations and both are used. Diffraction of the incoming wave is calculated in three steps. First diffraction from a single atom is considered within a spherical representation, then diffraction within a layer of atoms is calculated, again with spherical wavefunctions. Finally diffraction between layers is calculated. For this last step plane waves are used to represent the electron wavefunction. Exact treatment of multiple scattering including scattering to infinite order requires infinite computational efforts. High complexity of the surface geometry and strong multiple scattering also significantly increase the computational cost. In order to reduce the computational effort several approximations are used. Instead of treating systems as infinite in two dimensions slab models of finite thickness are used. A method called Renormalized Forward Scattering (RFS) can calculate interlayer diffraction more efficiently by treating surface reflectivity as a pertubation expansion of backward scatter-

ing. This is a good approximation as the backward scattering is relatively weak. For the forward scattering RFS does use scattering phase shifts, because this is a strong process. A similar method termed Reverse Scattering Pertubation applies this approximation for diffraction within a layer. Thermal vibrations of atoms are included in the theory via energy-dependent Debye-Waller factors for the atomic scattering amplitudes.

Comparing theory and experiment

The calculated I/V-curves need to be compared with the experimental data. Visual inspection of the experimental and theoretical curves can give an impression of how good the overall agreement is. But in order to quantify the quality of the fit, which is necessary for a self-consistent cycle as depicted in Figure 11, a numerical value has to be assigned to the degree of similarity between the curves. This quantity is called the reliabilty (R) factor. There exist numerous R-factors for various applications of comparing curves and in I/V-LEED the Pendry R-factor [108], which will be described in the following, is most commonly used. Pendry's R-factor is based on the idea, that peak positions in I/V-curves can be calculated pretty accurately, whereas the intensities are not as well reproduced. Specifically absolute intensities should not play any role in the determination of the R-factor while relative intensities between peaks should be somewhat considered. While normalization of the experimental data removes the influence of absolute intensities, the use of the logarithmic derivative of the intensities with respect to the energy, instead of the intensities themselves, within the R-factor calculation, reduces the influence of relative intensities between different peaks:

$$L(E) = \frac{I'}{I} = \frac{\partial I/\partial E}{I} \tag{17}$$

Multiple scattering can lead to destructive interference that causes zero intensity in the I/V-curves. This would lead to an infinitely large $L(E)$. Therefore instead of $L(E)$ a function $Y(E)$ is used which avoids division by zero in the I/V-curves:

$$Y(E) = \frac{L^{-1}}{L^{-2} + V_{0i}^2} = \frac{L}{1 + (LV_{0i})^2} \tag{18}$$

The Pendry R-factor is then defined as

$$R_P = \sum_{\vec{g}} \int \left(Y_{\vec{g},theory} - Y_{\vec{g},experimental}\right)^2 dE \Big/ \sum_{\vec{g}} \int \left(Y^2_{\vec{g},theory} + Y^2_{\vec{g},experimental}\right) dE \quad (19)$$

The better the agreement between experimental and theoretical curves the closer R_P gets to 0. When the average of the product $Y_{\vec{g},theory} \times Y_{\vec{g},experimental}$ becomes zero, the two curves are defined as uncorrelated and R_P becomes 1.

Search Algorithms

We have so far discussed the calculation of the I/V-curves as well as the comparison with experiment through a Pendry R-factor. Looking at Figure 11 one crucial step in the structure determination with I/V-LEED is still missing: The modification of the trial structure. Theoretically it is possible to simply randomly vary the input parameters (atomic coordinates, Debye temperatures representing vibrational amplitudes and real and imaginary part of the inner potential) repeatedly until a low R-factor has been achieved. In practice, because of the complexity of the LEED calculations and the size of the parameter space, this is unlikely to give good results within realistic timescales even when using many processors in parallel. The solution are directed search algorithms. Often a simple minimization algorithm such as the Powell method [109] is used in combination with Tensor LEED. [110, 111] In Tensor LEED the trial structure is described by a perturbation of a reference structure. The changes in the I/V-curves of the reference structure as a result of the distortion are calculated by first order perturbation theory. This can significantly reduce the computational cost. While Tensor LEED is very fast it can fail when the initial trial structure is very different to the structure with minimal R_P and thus in this work Tensor LEED is not used. Instead we have employed two different search algorithms which both include full dynamical calculation of all beams for all trial structures. However the modification of the trial structures is not done randomly but systematically. Because of this, the time needed to reach convergence in the R-factor when running calculations on many CPUs is acceptable. The two different search algorithms used are Covariance Matrix Adaptation - Evolutionary Strategy (CMA-ES) and Differential Evolution (DE). As their names indicate they both employ evolutionary schemes in that they create a population of individuals from the initial trial structure and use this population to create a next generation population, repeating this process many times. The difference between

the two algorithms is the way in which one generation is created from the previous one. In this work, CMA-ES [112] was implemented through use of the Shark library [113]. CMA-ES creates individuals solely mutation. The user defines the numbers of parents μ (individuals in a generation used to create the next generation) and the number of children λ (individuals resulting from the parent generation) with $\lambda > \mu$. Additionally the width, i.e. standard deviation, of the normal distribution which enters the mutation step is entered for each parameter. The normal distributions for all parameters are represented in a covariance matrix. Initially the covariance matrix is used together with random numbers to generate the first generation from the trial structure input by the user. This generation is then used as the first parent generation, generating offspring through mutation of individuals by a combination of random numbers with the covariance matrix. From the λ individuals of this generation of children μ are selected based on fitness to form the next generation of parents. The fitness in this case is related to the Pendry R-factor, so that the smaller the R-factor the bigger the fitness of the respective individual. To speed up the evolutionary process and minimize the amount of generations that have to be calculated before convergence with respect to R is reached the covariance matrix is adapted based on the hypersurface of the R-factor generated from the previous generations. This gives rise to the name covariance matrix adaptation.

Differential Evolution [114] represents individuals as vectors and perturbs parents with a difference between two individuals of the parent generation to create offspring. Each generation G consists of NP D-dimensional vectors $\vec{\chi}_{i,G}$ with D being the number of fit parameters and $i \in 1, 2, \ldots, NP$. The first generation is generated by random deviations with a normal distribution to the initial trial structure. For each target vector $\vec{\chi}_{i,G}$, that means each vector in the parent generation, a mutated vector $\vec{\nu}_{i,G+1}$ is generated as follows:

$$\vec{\nu}_{i,G+1} = \vec{\chi}_{j,G} + F \cdot (\vec{\chi}_{k,G} - \vec{\chi}_{l,G}) \tag{20}$$

with the indexes $j, k, l \in \{1, 2, \ldots, NP\}$, $i \neq j \neq k \neq l$ and $F > 0$. j, k, l are randomly chosen and in order to fulfill the above NP has to be at least four. F is a real number $\in [0, 2]$ that describes how strongly the difference $(\vec{\chi}_{k,G} - \vec{\chi}_{l,G})$ influences the mutated vector. In the next step a trial vector $\vec{\tau}_{i,G+1}$ with D parameters is generated such that

$$\vec{\tau}_{i,G+1} = (\vec{\tau}_{1,i,G+1}, \vec{\tau}_{2,i,G+1}, \ldots, \vec{\tau}_{D,i,G+1})\,. \tag{21}$$

The parameters $\vec{\tau}_{j,i,G+1}$ are determined according to

$$\vec{\tau}_{j,i,G+1} = \begin{cases} \vec{\nu}_{j,i,G+1} & \text{if } (random(j) \leq CR) \text{ or } j = rnb(i) \\ \vec{\chi}_{j,i,G} & \text{if } (random(j) > CR) \text{ and } j \neq rnb(i) \end{cases}. \tag{22}$$

$random(j) \in [0,1]$ is the jth evaluation of a random number generator. $CR \in [0,1]$ is the crossover ratio set by the user. $rnb(i) \in \{1, 2, \ldots, D\}$ is randomly chosen to guarantee that at least one parameter of the mutated vector is incorporated in the trial vector. Thus, the trial vector $\vec{\tau}_{ji,G+1}$ is a mixture between the mutated vector $\vec{\nu}_{i,G+1}$ and the target vector $\vec{\chi}_{i,G}$. In total NP trial vectors are generated. For each trial vector the Pendry R-factor is determined and if it is lower than R_P of the corresponding target vector the trial vector replaces the target vector in the next generation.

2.3 Scanning Tunneling Microscopy (STM)

The scanning tunneling microscope (STM) was developed by Binnig and Rohrer at IBM Zürich in 1981 [115, 116] and earned them the Noble Prize in Physics in 1986 together with Ernst Ruska who developed the transmission electron microscope. In STM a sharp metal tip is brought within several Å of a conductive surface. Application of a bias voltage between sample and tip generates a tunneling current. The tip is then laterally moved across the sample by two piezoelectric motors in x and y direction. The z position is controlled with a third piezoelectric motor that moves the tip vertically relative to the sample. The z movement is coupled to a feedback loop that measures the tunneling current, compares it with a user-defined setpoint for the tunneling current and changes the voltage applied to the z motor to keep the tunneling current at the setpoint. The z position of the tip as a function of x and y coordinates yields a three dimensional image of the sample. Employment of piezoelectric drives to control the position allows placement of the tip with sub-atomic precision. The tunneling current is a very sensitive probe for the surface topography since it depends on the distance between sample and tip exponentially following the expression

$$I \propto f\left(U\right) \cdot exp\left(-\alpha \cdot s \cdot \sqrt{\Phi}\right). \tag{23}$$

Here I is the tunneling current, U is the bias voltage applied, $\alpha = 10/\left(\mathrm{nm}\sqrt{\mathrm{eV}}\right)$, s is the distance between sample and tip in nm and Φ is an effective barrier height for the tunneling process in eV. Φ is a good approximation to the work function when U is small. The function $f\left(U\right)$ depends on the electronic structures of tip and sample and is roughly proportional to U. Standard convention puts the tip on ground potential. This means that applying a positive voltage to the sample results in electrons tunneling from the tip into unoccupied orbitals of the sample as visualized in Figure 12. A negative voltage applied to the sample has electrons tunneling from occupied sample orbitals to the tip.

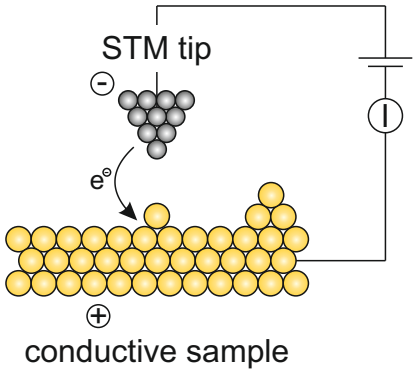

Figure 12: Working principle of STM

In order to get good resolution the quality of the metal tip used to probe the surface is crucial. Ideally it is terminated by a single atom and very sharp to minimize interactions between other tip atoms and the sample. While a variety of metals including gold, iridium and molybdenum among others, as well as metal alloys (most prominently platinum-iridium) are used as materials for STM tips the following discussion will focus on tungsten as a tip material which was used throughout this work.

Sharp W tips were prepared by electrochemical etching of 0.25 mm thick W wire, which was previously annealed in UHV, in an aqueous 2 M KOH solution. The W wire was cut into 1 cm to 2 cm long pieces which were in turn attached to the Mo tip carriers via spot welding. Ta plates were used to fix the W wire ontop of the Mo tip carrier. The W wire was then inserted into the solution and a bias of several volts applied between the W wire and the counter electrode. Over the course of 10 min to 20 min the wire gets thinner until

eventually the bottom part drops off leaving a sharp tip behind at the top as shown in Figure 13. Quick transfer of the tip into the UHV system reduces the amount of oxidation it suffers; W readily oxidizes even at room temperature.

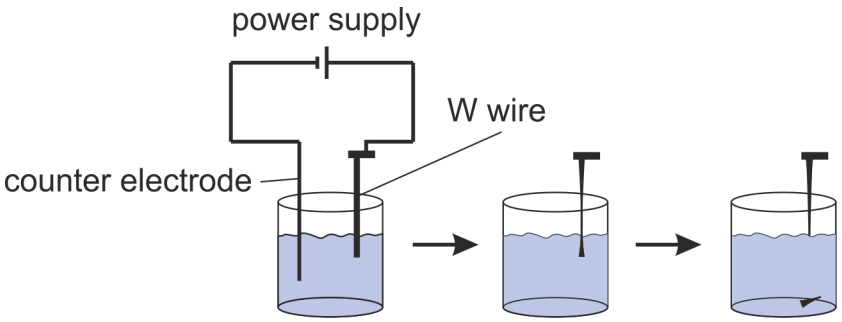

Figure 13: Setup for etching W tips with KOH solution

In the UHV system the W tips are optimized through two procedures: Annealing and ion bombardment. Both methods can remove an oxide overlayer from the tip and both can induce changes in the tip geometry. Typically ion bombardment is used to clean the tip from oxide after exposure to oxygen while tip annealing is used when the tip appears to not be sharp enough to give good resolution. In order to anneal the tip two W wires within the UHV system are brought into contact with the tip from both ends as depicted in Figure 14. Then a voltage is applied and a current of $\sim 10\,\mathrm{A}$ is being run through the tip for $\sim 5\,\mathrm{min}$.

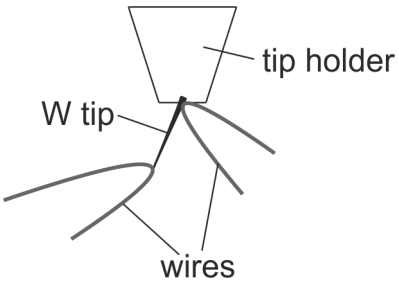

Figure 14: Geometry for annealing of W tips

Ar^+ bombardment was carried out with 5000 V in 4×10^{-6} mbar Ar with an Omicron ISE10 Sputter Ion Source or 3000 V in 2×10^{-5} mbar Ar with a Specs IQE 11-A sputtergun leading to currents of about 10 µA to 20 µA. The typical duration of ion bombardment was between 5 min and 20 min.

In the following some of the common problems encountered in STM are presented together with possible solutions.

The first and biggest problem is the observation of very noisy images that show little to no features that can be attributed to the sample. This is usually due to a bad, i.e. blunt or unstable, tip but can be a combination of a dirty or disordered sample and a suboptimal tip. This can lead to time-consuming preparation of the tip followed by the realization that, even with a good tip, only a badly ordered or dirty sample is being imaged. The reasons for a badly ordered or dirty sample could be inadequate preparation (for example ion bombardment leads to rough surfaces with many defects, annealing at too low temperatures or for too short periods of time might fail to induce sufficient ordering of the film, preparation of oxides in the wrong oxygen pressure or metal deposition at an erroneous rate) or contamination through the chamber atmosphere (due to relatively high pressures, a very reactive surface or too much time passing since the last cleaning/ preparation step).

There are two solutions to these issues.

Following a previously established preparative routine, that is known to produce well-ordered samples, is one of them.

Additionally ensuring a relatively high sample quality by means of other, less time-consuming analytical methods prior to STM measurements can save significant amounts of time. While early on in this thesis the visual quality of LEED images was often used as a first estimate for film quality, over the course of the project this was developed into a quantitative method whereby the spot intensity of a diffraction spot in LEED is divided by the background intensity. The larger this ratio is the higher the order of the surface.

A fact that can be either detrimental or beneficial is that the tip is not static and can change during the measurement by either picking up atoms or molecules from the sample or by dropping off particles. In the case of a high quality tip this is undesired and in order to avoid ruining a good tip that currently gives high resolution it can be helpful to scan smaller areas, reducing the chance of encountering adsorbates during a scan. On the other hand a bad tip can be improved through this mechanism, making bigger scan-areas suitable to shape an unstable tip.

Another way to change the tip is by "pulsing", i. e. applying a short voltage pulse between tip and sample. When applying a voltage of opposite sign to the bias voltage used in the STM scan and slightly smaller in magnitude the tip will jerk towards the sample which can induce dropping off or picking up of atoms or molecules.

Two more problems are thermal drift and piezo creep. Thermal drift results from the sample not being thermalized (in the setup used in this work the STM is always at room temperature). This leads to a significant drift imaged in STM images and basically makes imaging impossible until the sample is thermalized. In order to avoid this, thermalization of the sample directly after preparation and before insertion into the STM is preferable. Piezo creep occurs either due to the scanning motion of the tip, this is typically visible as lines across the STM pictures which run in opposite directions in backwards and forwards scan (see Figure 15), or due to movement of the scan area by the user, which leads to a significant drift after the new scan area is reached and usually dies down within half of an image.

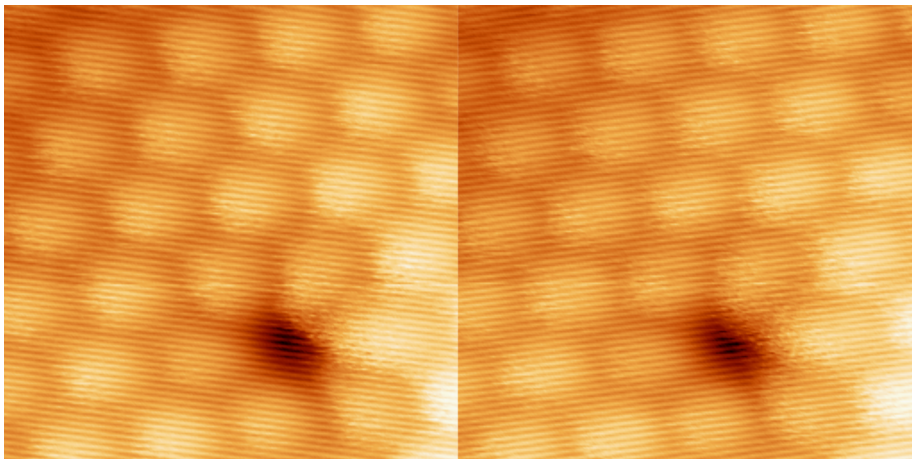

Figure 15: 2.5 Å by 2.5 Å images of the $V_2O_3(0001)$ surface in forward (left) and backward (right) scan direction showing the scanlines resulting from piezo creep.

2.4 X-Ray Photoelectron Spectroscopy (XPS)

Photoelectron spectroscopy was pioneered by Kai Siegbahn in the 1950s and 1960s and he consequently received the Nobel Prize in physics in 1981, shared with Nicolaas Bloembergen and Arthur Leonard Schawlow for their contributions to the development of laser spectroscopy. In photoelectron spectroscopy (PES) electromagnetic radiation is used to eject electrons from atoms or molecules (see Figure 16). This is based on the photoelectric effect discovered by Hertz in 1887 [117] and explained by Einstein in 1905 [118] through the following formula

$$h\nu = \frac{1}{2}m_e v^2 + BE + q\Phi \ . \tag{24}$$

h is Planck's constant, ν the frequency of the incoming electromagnetic radiation, m_e is the electron mass, v is the velocity of the photoelectron ejected, BE is the binding energy of the electron within the atom, q is a reference charge and Φ is the sample's workfunction. Depending on the energy range of the incident electromagnetic radiation photoelectron spectroscopy is often divided into two areas: in X-ray Photoelectron Spectroscopy (XPS) X-rays with a wavelength of several nm or less are used to excite core electrons, in Ultraviolet Photoelectron Spectroscopy (UPS) photons from the ultraviolet range of the spectrum are used to excite valence electrons. In this work XPS was used exclusively and therefore the rest of the text will focus on XPS; the working principle and many features are however the same in both techniques.

The binding energies of the electrons in a specific element are characteristic features of that element. They are tabulated and allow identification of the elemental composition of a sample, coining the alternative name Electron Spectroscopy for Chemical Analysis (ESCA) as a synonym for XPS. In addition the chemical environment of an atom influences the binding energies of the atom's electrons. A more positively charged atom will bind its electrons more strongly, leading to a reduced kinetic energy of the photoelectron emmitted. For example the binding energies of the vanadium $2p_{3/2}$ level are 512 eV in elemental vanadium (formal oxidation state 0), 515 eV in V_2O_3 (formal oxidation state +III), 516 eV in VO_2 (formal oxidation state +IV) and 517 eV in V_2O_5 (formal oxidation state +V). This chemical shift of the binding energies allows the distinction of several atoms of the same element with different oxidation states coexisting in a sample. XPS thus allows identification of the elements contained in a sample, the oxidation states of those elements and the stoichiometry of the sample. Determining the stoichiometry involves integration over peak areas and has to account for element dependent cross sections for X-ray absorption as well as electron mean free path lengths that depend on the material and the electron kinetic energy.

In order to generate X-rays either a laboratory source (i.e. $Al - K_\alpha$ or $Mg - K_\alpha$ in our experiments, Cu can be used if higher energies are needed) or synchrotron radiation can be used. The advantages of synchrotron radiation are much a higher intensity leading to better signal to noise ratios, a better energy resolution and the tunability of the X-

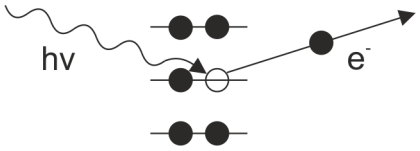

Figure 16: Basic principle of photoelectron spectroscopy

ray energy which allows the optimization of the crossection between an orbital to be investigated and the X-rays further increasing sensitivity. The ejected photoelectrons are analyzed in a hemispherical analyzer. A hemispherical analyzer consists of two concentric hemispheres acting as condensers. The voltage applied between them focuses electrons of a certain kinetic energy while electrons with deviating kinetic energy are deflected and do not reach the exit slit. In principle scanning the kinetic energy of the electrons could be done by varying the voltage applied between the two hemispheres. In practice this is avoided because it would lead to an energy resolution varying with kinetic energy of the measured electrons. Instead the electrons coming into the analyzer are retarded by electrostatic lenses before reaching the analyzer. In this way all electrons traveling through the detector have the same kinetic energy, called pass energy, and thus the energy resolution is constant over the complete energy range of the spectrum. The kinetic energy that the electrons had before being retarded can easily be calculated from the retarding voltage used to decelerate them.

The strong interaction between electrons and atoms makes photoelectron spectroscopy an inherently surface sensitive technique. While the X-rays which are used to excite the sample interact relatively weakly with matter and can penetrate into the bulk of the sample material the escape depth of the photoelectrons produced by them is much smaller.

This can be used to increase the surface sensitivity of the measurement, i.e. reduce the volume of the sample probed, by varying the angle between sample and detector. When the sample normal is in line with the axis of the analyzer as shown in the left hand side of Figure 17 the depth probed is maximized because the distance electrons have to travel from a certain depth towards the analyzer before they reach the sample surface is at a minimum. Increasing the angle between the detector and the sample normal, as depicted in the right hand side of Figure 17, increases the distance travelled by electrons from a certain depth to the surface and thus reduces their impact on the measured spectra.

The resulting spectra at off-normal emission are thus more surface sensitive. Comparison of spectra taken at normal emission and at grazing emission can allow identification of surface-specific features. The maximum angle achievable depends on the experimental setup.

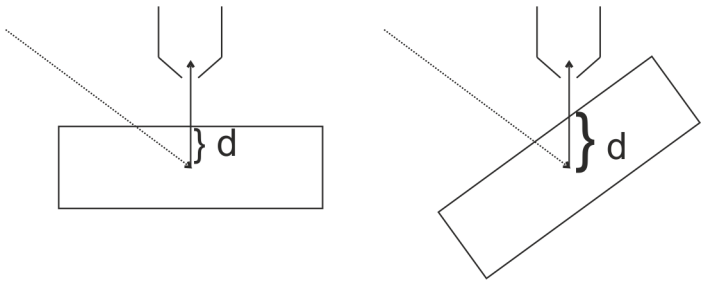

Figure 17: Dependence of the electron escape depth on the angle between sample and analyzer

Photoemission spectra can be plotted on a scale of kinetic energy or binding energy. Often, the binding energy scale is preferred, as it allows easy identification of the photoelectron peaks: the binding energies of these peaks are independent of the excitation source. When identifying spectral features of a sample with known elements it is easiest to assign all the photoelectron peaks corresponding to the known elements first. Afterwards the peaks for Auger processes in these elements can be assigned. In an Auger process the core hole left behind by the photoemission process is filled by an electron from a higher lying orbital. The difference in energy between the two levels is transferred to a third electron which escapes the sample and can be measured. In contrast to photoelectrons, which have a binding energy independent of the X-ray source, for Auger electrons the kinetic energy is fixed and the position on a binding energy scale varies when changing the X-ray source. The remaining spectral features can either belong to unknown elements, i.e. contaminations, in the sample or be X-ray satellites, X-ray ghost lines or shake-up lines. Satellites result when using non-monochromatic X-rays. Ghost lines are created by X-rays coming from a different element than the chosen x-ray source. They can result from impurities in the anodes or from oxidized anode material. Shake-up lines are the consequence of transitions to excited states. These have higher energies than the ionized ground state and thus the kinetic energy of the photoelectron will be smaller, leading to shake-up lines with higher binding energy than the main peak.

Chapter 3

Results and Discussion

V_2O_3 films were prepared by evaporation of vanadium in an oxygen atmosphere while heating the Au(111) substrate. After vanadium evaporation was finished the sample was annealed in two steps, first in oxygen and then at low oxygen pressure or in UHV, to achieve ordering of the V_2O_3 film. Typical conditions were 573 K and 2×10^{-7} mbar O_2 pressure during deposition, 700 K and 2×10^{-7} mbar O_2 pressure in the first annealing step and 900 K and 5×10^{-9} mbar O_2-pressure in the final annealing step.

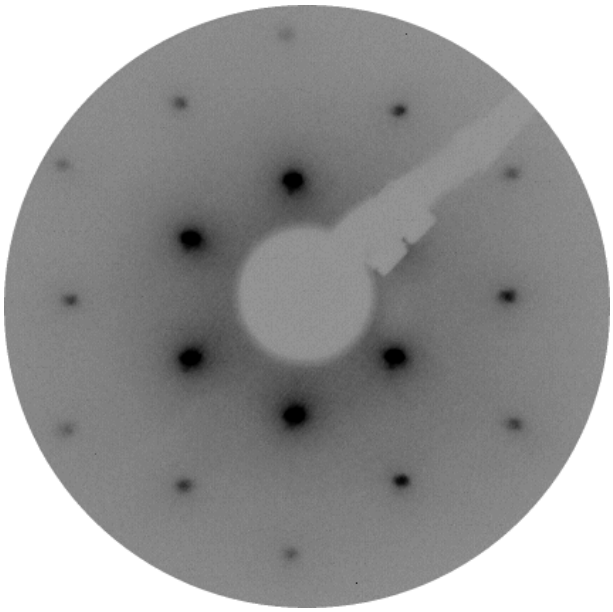

Figure 18: LEED image of the $V_2O_3(0001)$ surface taken at an energy of 150 eV

This results in ordered V_2O_3 films exposing the (0001) surface. A LEED image of this surface taken at an electron energy of 150 V is shown in Figure 18. It displays the hexagonal structure characteristic of the $V_2O_3(0001)$ surface.

An XPS spectrum of a V_2O_3 film, recorded with $Al - K_\alpha$ X-rays at an emission angle of 70°, is shown in Figure 19 with a binding energy scale. The upper right hand of the

image shows a scan of the area around the O1s and V2p peaks. The peaks at 1000 eV binding energy and higher result from Auger processes. Transitions from the core levels of vanadium and oxygen produce peaks at 631 eV (V2s), 531 eV (O1s), 524 eV ($V2p_{1/2}$), 516 eV ($V2p_{3/2}$), 69 eV (V3s), 41 eV (V3p) and 22 eV (O2s). At 87 eV the Au4f peak is detectable despite the ~ 100 Å thick V_2O_3 film, because the photoemission process has a very large cross section for this peak.

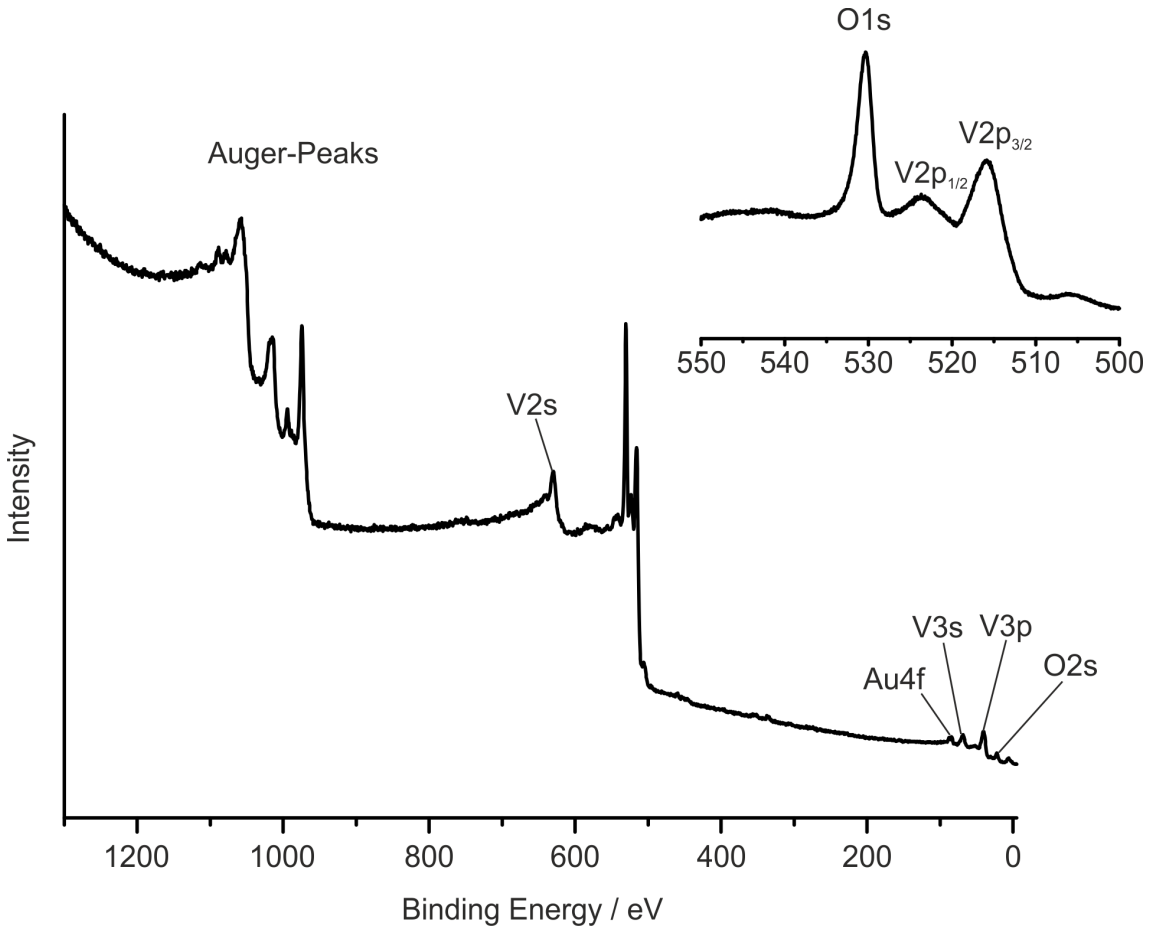

Figure 19: XPS spectrum of the $V_2O_3(0001)$ surface, X-ray source $Al - K_\alpha$, grazing emission (70°)

Surface Structure of $V_2O_3(0001)$ Revisited

Felix E. Feiten,[1] Jan Seifert,[1,2] Joachim Paier,[3,†] Helmut Kuhlenbeck,[1,*] Helmut Winter,[2] Joachim Sauer,[3] and Hans-Joachim Freund[1]

[1]*Fritz-Haber-Institut der Max-Planck-Gesellschaft, Faradayweg 4-6, 14195 Berlin, Germany*
[2]*Humboldt-Universität zu Berlin, Institut für Physik, Newtonstrasse 15, 12489 Berlin, Germany*
[3]*Humboldt-Universität zu Berlin, Institut für Chemie, Unter den Linden 6, 10099 Berlin, Germany*

(Received 20 January 2015; published 26 May 2015)

In a recent paper [A. J. Window *et al.*, Phys. Rev. Lett. 107, 016105 (2011)], it was proposed that $V_2O_3(0001)$ is terminated by the so-called O_3 termination, a reconstruction with a terminating distorted hexagonal oxygen layer. We show that the surface is terminated by vanadyl (V=O) groups instead. This conclusion is based on quantitative low-energy electron diffraction combined with scanning tunneling microscopy, fast atom scattering, and density functional theory employing the Heyd-Scuseria-Ernzerhof functional. New insights into the subsurface sensitivity of ion beam triangulation show that results previously interpreted in favor of the O_3 termination are reconcilable with vanadyl termination as well.

DOI: 10.1103/PhysRevLett.114.216101 PACS numbers: 68.35.B-, 61.05.jh, 68.47.Gh

Vanadium oxides find significant interest in basic research and are of technological importance because of their metal to insulator transitions and applications in oxygen transfer catalysis [1–5]. The surface termination is of decisive relevance for both classes of applications—this is obvious for the area of catalysis, but the influence on phase transitions, at least in near-surface layers, has also been shown [6]. For $V_2O_3(0001)$, a number of studies have been published, but there is still an ongoing debate about its termination [7–14].

For almost a decade, the $V_2O_3(0001)$ surface prepared under ultrahigh vacuum (UHV) conditions was assumed to be vanadyl terminated. This conclusion was based mainly on the presence of an intense vanadyl signal in vibrational spectra [7,8], but scanning tunneling microscopy (STM), X-ray photoelectron spectroscopy, and near edge X-ray absorption fine structure data also supported this view [7,8,15]. However, recent studies employing ion scattering and density functional theory (DFT) strongly favor the O_3 termination [9–11].

Motivated by this controversy, we have performed an extensive quantitative surface structure determination employing low-energy electron diffraction (LEED) and *I-V* LEED combined with STM, as well as fast atom scattering and DFT. Furthermore, we reinterpret the results of a previous ion scattering study [10].

The hexagonal bulk unit cell of V_2O_3 gives rise to three different possible terminations when cutting parallel to the 0001 plane: metal terminations with two vanadium atoms [double metal (DM)] ($\cdots O_3{-}V_2{-}O_3{-}V_2$) and one vanadium atom [single metal (SM)] ($\cdots O_3{-}V_2{-}O_3{-}V$) in the surface unit cell, respectively, and an oxygen termination ($\cdots O_3{-}V_2{-}O_3$). DFT calculations indicate that several reconstructions are energetically favorable over the bulk terminations [12,13]. At low oxygen chemical potential a vanadyl-covered surface ($\cdots O_3{-}V_2{-}O_3{-}V{=}O$) is thermodynamically stable, while at higher oxygen chemical potential incomplete V=O terminations form, with ordered superstructures at 2/3 and 1/3 of the full V=O coverage and finally an O_3 termination completely devoid of V=O groups. Compared to the bulklike, oxygen-terminated surface, this O_3 termination is reconstructed with each second V atom from the second layer moved up into the first layer ($\cdots O_3{-}V{-}O_3{-}V_3{-}O_3$) as shown in Fig. 1.

About 100 Å thick $V_2O_3(0001)$ films were prepared on Au(111) by deposition of vanadium from an *e*-beam evaporator with a rate of ~0.7 Å/ min in an O_2 ambience, followed by annealing in oxygen and finally in UHV for a short time. Some films were afterwards oxidized by annealing at elevated oxygen pressures. While films deposited at 1×10^{-7} mbar$< p(O_2) < 1 \times 10^{-6}$ mbar show a (1×1) LEED pattern, a $(\sqrt{3} \times \sqrt{3})R30°$ superstructure appears after exposure to higher O_2 pressures. This is the first clear evidence that none of the prepared layers was O_3

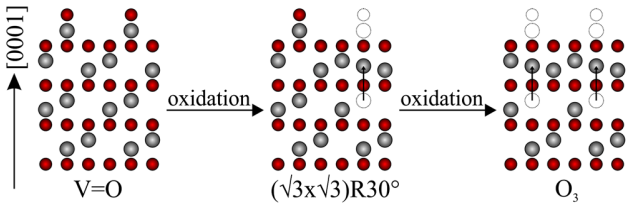

FIG. 1 (color online). Structural model (V gray and O red) of surface terminations predicted by DFT.

*Corresponding author.
kuhlenbeck@fhi-berlin.mpg.de
†To whom all correspondence regarding the density functional computations should be addressed.
joachim.paier@chemie.hu-berlin.de

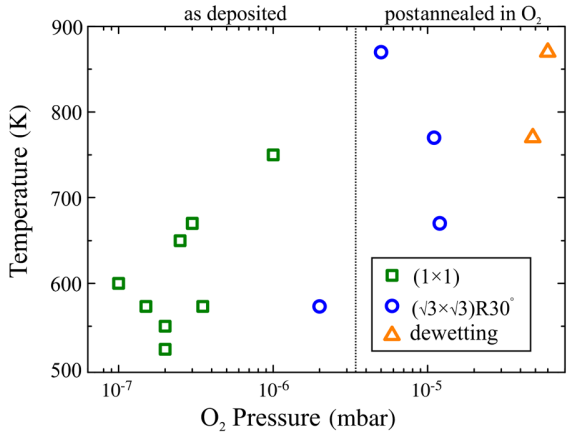

FIG. 2 (color online). Experimentally observed surface phases as a function of the preparation conditions.

terminated, since the oxygen content in the O_3 structure is higher than in the $(\sqrt{3} \times \sqrt{3})R30°$ phase. At even higher oxygen pressure, the film disappeared, probably through formation of V_2O_5, which sublimates at above ~800 K [16]. An overview of the observed phases is shown in Fig. 2.

While the $(\sqrt{3} \times \sqrt{3})R30°$ termination can easily be identified by LEED, both the V=O-covered surface and the O_3 termination exhibit identical reflex patterns. Thus, *I-V* LEED analysis was used to differentiate between these structures and to determine the positions of the atoms at the surface. For this study, the intensities of 32 diffraction spots were recorded. Averaging over symmetry equivalent spots and different domains yielded eight different beams over a combined energy range of 1819 eV. Beam damage was minimized by use of a LEED system with a microchannel plate detector, reducing electron currents to the surface to less than 10 nA. *I-V* curves were calculated with a modified version of the SATLEED package of Barbieri and van Hove [17]. The Pendry *R* factor [18] was used to quantify the agreement between theory and experiment—a smaller *R* factor means better agreement. The structures were refined by minimization of the *R* factor using a covariance matrix adaptation evolution strategy as implemented in the SHARK library [19]. Depending on the structural model, 15–17 atomic coordinates and three to five Debye temperatures as well as the imaginary and real parts of the inner potential and a linear background of the experimental data were selected as refinement parameters.

A total of 14 different structures with varying interlayer distances (five SM, five V=O, two DM, and two O_3 [11,12,20,21]) were selected as start structures for the refinement. Out of all models, coordinates published by Czekaj, Hermann, and Witko [20] for a V=O-terminated surface led to the smallest *R* factor after refinement ($R = 0.12$) [22]. In contrast, the smallest *R* factor for the O_3 termination is 0.36. The corresponding *I-V* curves shown in Fig. 3 visualize the good agreement between the

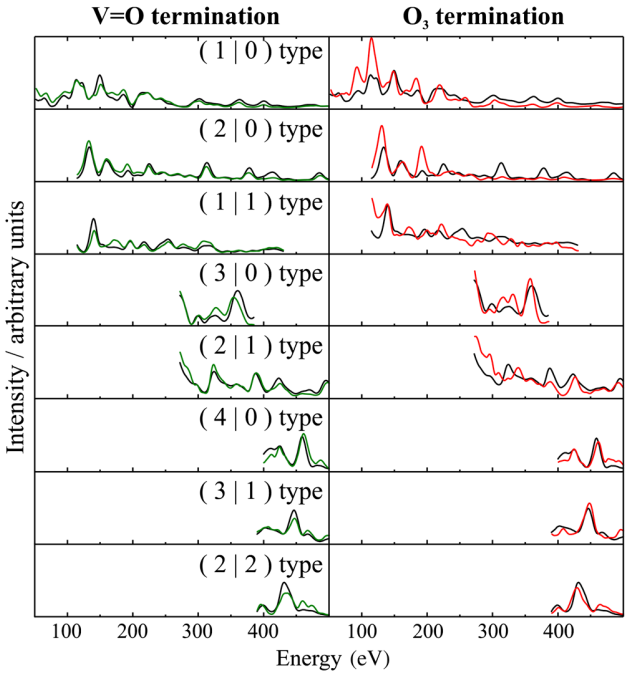

FIG. 3 (color online). Calculated *I-V* LEED curves (green and red) and experimental data (black) for the eight symmetry inequivalent beams.

V=O simulation and the experiment, while there are clear deviations from the experimental curves for the best-fit simulation of the O_3 termination.

STM images obtained for the (1×1) phase always show a hexagonal lattice (Fig. 4). This type of STM image is consistent with Tersoff-Hamann simulations for a fully vanadyl-covered surface, while the triangular features characteristic of an O_3 termination [11] or a bulklike oxygen termination [23] were never seen. Figure 4(a) shows an image taken directly after recording the *I-V* curves shown in Fig. 3. The bright triangular features are attributed to a slight reduction of the surface. In Fig. 4(b), a slightly oxidized surface is imaged. Herein dark depressions correspond to missing V=O groups [8].

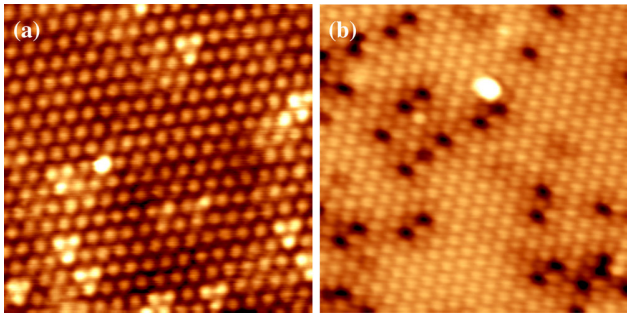

FIG. 4 (color online). Atomically resolved STM images of the $V_2O_3(0001)$ surface. (a) Slightly reduced layer; (b) slightly overoxidized layer. 10×10 nm^2, 2 V, and 0.1 nA.

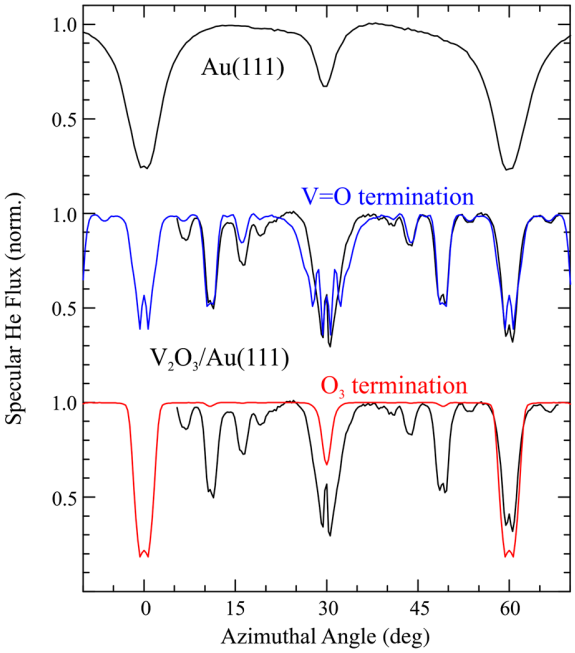

FIG. 5 (color online). Intensity of specularly reflected 2 keV He atoms (black curve) from Au(111) and a $V_2O_3(0001)$ thin film as a function of the azimuthal angle as well as simulations for the vanadyl (blue curve) and O_3 termination (red curve) of $V_2O_3(0001)$.

Further evidence is provided by grazing angle scattering of 2 keV He atoms. In this experiment the flux of specularly reflected He atoms was recorded as a function of the azimuthal rotation of the sample for a polar incidence angle of 1° with respect to the surface plane. Incidence along a principal axis, i.e., for scattering along a line of densely packed atoms, leads to a broadening of the angular distribution and thus to a reduction of the flux in the specular direction. In Fig. 5, this flux is plotted for Au(111) (upper panel) and a $V_2O_3(0001)$ film (lower panels). The data are compared with simulations based on classical trajectories using a superposition of atomic pair potentials as described elsewhere [24]. For the vanadyl termination (blue curve) good overall agreement is observed, whereas the close packing of surface oxygen atoms in the O_3 model (red curve) leads to narrow axial channels with little lateral deflection of scattered projectiles for most directions. The simulated curve deviates significantly from the experimental one.

This finding seems to be in conflict with a recent ion beam triangulation study [10] which favored the O_3 termination. In this study, electron emission following the grazing scattering from the surface of 25 keV H atoms was recorded as a function of the azimuthal surface orientation. For close-packed crystal surfaces, thin films, and adsorbate systems, a high surface sensitivity of ion beam triangulation has been demonstrated [25,26]. However, for one monolayer of the amino acid alanine on Cu(110) [24], a curve similar to that for the clean substrate was obtained, whereas from triangulation, based on the specular flux of 2 keV He atoms, information on the position of the topmost methyl groups is obtained. A similar issue may also be in effect for the $V_2O_3(0001)$ surface, where the relatively sparsely distributed vanadyl groups may affect the emission of electrons to a lesser extent than previously assumed.

Since DFT has been invoked to support the O_3 surface termination [9], we examine the sensitivity of DFT results with respect to the choice of the exchange-correlation functional, specifically with respect to Fock exchange. The screened hybrid functional after Heyd, Scuseria, and Ernzerhof (HSE) [27] with a range-separation parameter of 0.207 $Å^{-1}$ was used. Spin polarization was not included, because at ambient temperature V_2O_3 is a nonmagnetic metal crystallizing in the rhombohedral corundum structure. Our spin-unpolarized DFT calculations use the VASP code and employ projector-augmented plane waves (PAWs) up to a kinetic energy of 600 eV [28–30]. The electron-ion interaction was described by using PAW pseudopotentials with $3p^6 3d^3 4s^2$ and $2s^2 2p^4$ as valence electrons for V and O, respectively. Symmetric slab models of the primitive surface unit cell with a lattice constant of 4.933 Å (HSE equilibrium lattice constant) and 30 atomic layers were used, and a vacuum layer of approximately 10 Å was employed to separate periodic images of the slabs. To model the bulk, two innermost V atoms and one neighboring O trilayer per V were kept frozen at bulk positions. Forces acting on the atoms in the remaining 26 layers were relaxed to better than 0.05 eV/Å. To sample the surface Brillouin zone, Γ-centered Monkhorst-Pack meshes using $(2 \times 2)k$ points were used. Energies obtained by using a $(4 \times 4)k$ mesh (single points) consistently shifted the intercepts of the linear equations for surface energies by less than 6 meV/$Å^2$; thus, the results did not change qualitatively.

Schwingenschlögl and co-workers found that lowering the amount of Fock exchange (FX) from 25% to 10% in the HSE hybrid functional results in a more balanced description of the VO_2 bulk phases [31]. However, we found that HSE using the "as defined" amount of FX of 25% outperforms the Perdew-Burke-Ernzerhof (PBE) [32] functional, which is based on the generalized-gradient approximation (GGA) and does not include Fock exchange. HSE heats of formation for V_2O_3, V_2O_4, and V_2O_5 agree better with observed values than PBE results. Also, the oxidation of V_2O_3 to V_2O_4 is better described by using the HSE functional [33]. We do not claim that a simple hybrid functional like HSE consistently captures the complex physics of V_2O_3 mostly driven by Coulomb correlation effects, but based on the aforementioned thermochemical results we believe that HSE surface stabilities are more reliable than results obtained by using the PBE or the closely related Perdew-Wang 1991 GGA-type functionals used in earlier work [12]. Recent HSE results by Rubio

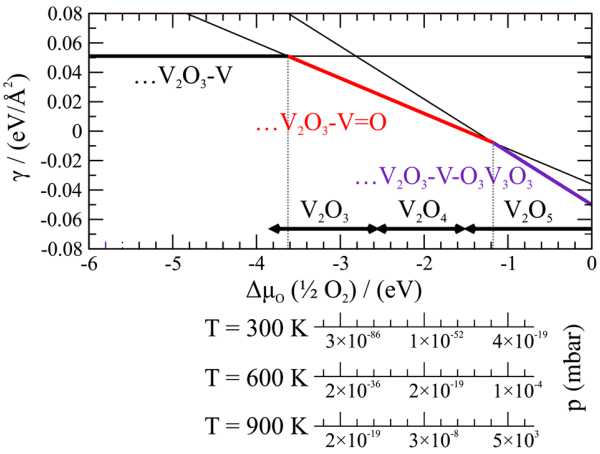

FIG. 6 (color online). Surface energy γ as a function of the chemical potential $\Delta\mu_O$ for different terminations of the $V_2O_3(0001)$ surface. At the bottom, the chemical potential scale is transformed into O_2 pressure scales (mbar) for different temperatures. The stability ranges of the bulk phases are indicated by the horizontal black arrows.

and co-workers [34], which describe the metal-insulator transition in paramagnetic V_2O_3 correctly, provide further support for our findings.

When adding some FX to the GGA-based functional, the highest oxygen chemical potential, for which V=O termination is calculated to be thermodynamically favorable, increases from −2.3 (which is exactly the same as the PBE functional, i.e., no FX) through −1.9 (HSE with 10% FX) to −1.2 eV (HSE with 25% FX).

The phase diagram calculated with HSE is shown in Fig. 6. Phase diagrams for pure GGA as well as for 10% FX are provided in Supplemental Material [35]. The oxygen chemical potential $\Delta\mu_O(\frac{1}{2}O_2)$ uses half of the total energy of the O_2 molecule as a reference. Tabulated values for the enthalpy H and entropy S at the temperature T were used [36]. Further details on the pressure and temperature dependence of $\Delta\mu_O$ can be found in Refs. [37,38]. Black arrows at the bottom refer to the stable bulk phases at the respective chemical potentials, while the bold lines above indicate the expected surface terminations. Figure 6 shows that the V=O termination is predicted to be thermodynamically stable over a wide range of oxygen chemical potentials. As also shown previously [12], the V=O termination cannot be reduced by heating in UHV, since the required potential is too negative to be realized experimentally. While conditions that would favor the O_3 termination are experimentally accessible, the stable bulk phase expected under these conditions is already V_2O_5, in agreement with the findings summarized in Fig. 2, which indicate that the oxide layer sublimates. We note that, according to the DFT calculations, V_2O_3 is not the equilibrium bulk phase for all preparation conditions employed in this study. This is a hint that the formation of higher oxides is just prevented by kinetic limitations.

In conclusion, we have shown that the $V_2O_3(0001)$ surface, prepared under standard UHV conditions, is terminated by vanadyl groups. *I-V* LEED measurements and fast atom scattering are clearly in favor of this termination, like the STM results. Recent ion beam triangulation results are also reconcilable with a vanadyl-terminated surface.

In a recent study, Window *et al.* [9] proposed that the surface might be terminated by an equilibrium mixture of O_3 and V=O areas with a small V=O contribution in order to explain the presence of the V=O stretching vibration in vibrational spectra. Neither our STM studies, which always show the presence of a single phase for well-prepared layers, nor our DFT calculations, which predict the vanadyl termination to be stable under the relevant conditions, support this conclusion. DFT shows that the O_3 termination is drastically destabilized. Even if one assumes an error of several hundred meV in the chemical potential of oxygen, which corresponds to several orders of magnitude of an error in the pressure, a phase equilibrium between V=O and O_3 with a noticeable contribution of the O_3 phase cannot be reached. This is in marked contrast to previous DFT studies [12,13] and can be attributed to the higher accuracy of the HSE hybrid functional as shown by, compared with experiment, improved formation enthalpies of bulk V_xO_y phases [33].

This work was supported by the Deutsche Forschungsgemeinschaft (DFG) through their collaborative research center 546, "Transition Metal Oxide Aggregates." We also acknowledge support from the Fonds der Chemischen Industrie, the North-German Supercomputing Alliance in Berlin and Hannover (HLRN; grants for computing time), and thank Horst Niehus for helpful discussions.

*Corresponding author.
kuhlenbeck@fhi-berlin.mpg.de
†To whom all correspondence regarding the density functional computations should be addressed.
joachim.paier@chemie.hu-berlin.de

[1] K. Held, G. Keller, V. Eyert, D. Vollhardt, and V. I. Anisimov, Phys. Rev. Lett. **86**, 5345 (2001).
[2] S. Surnev, M. Ramsey, and F. Netzer, Prog. Surf. Sci. **73**, 117 (2003).
[3] G. Deo and I. E. Wachs, J. Catal. **146**, 323 (1994).
[4] G. C. Bond and S. F. Tahir, Appl. Catal. **71**, 1 (1991).
[5] D. Göbke, Y. Romanyshyn, S. Guimond, J. M. Sturm, H. Kuhlenbeck, J. Döbler, U. Reinhardt, M. V. Ganduglia-Pirovano, J. Sauer, and H.-J. Freund, Angew. Chem., Int. Ed. Engl. **48**, 3695 (2009).
[6] F. Pfuner, J. Schoiswohl, M. Sock, S. Surnev, M. G. Ramsey, and F. P. Netzer, J. Phys. Condens. Matter **17**, 4035 (2005).
[7] A.-C. Dupuis, M. Abu-Haija, B. Richter, H. Kuhlenbeck, and H.-J. Freund, Surf. Sci. **539**, 99 (2003).

[8] J. Schoiswohl, M. Sock, S. Surnev, M. Ramsey, F. Netzer, G. Kresse, and J. Andersen, Surf. Sci. **555**, 101 (2004).
[9] A. J. Window, A. Hentz, D. C. Sheppard, G. S. Parkinson, H. Niehus, D. Ahlbehrendt, T. C. Q. Noakes, P. Bailey, and D. P. Woodruff, Phys. Rev. Lett. **107**, 016105 (2011).
[10] J. Seifert, E. Meyer, H. Winter, and H. Kuhlenbeck, Surf. Sci. **606**, L41 (2012).
[11] A. J. Window, A. Hentz, D. C. Sheppard, G. S. Parkinson, D. P. Woodruff, W. Unterberger, T. C. Q. Noakes, P. Bailey, M. Ganduglia-Pirovano, and J. Sauer, Surf. Sci. **606**, 1716 (2012).
[12] G. Kresse, S. Surnev, J. Schoiswohl, and F. P. Netzer, Surf. Sci. **555**, 118 (2004).
[13] T. K. Todorova, M. V. Ganduglia-Pirovano, and J. Sauer, J. Phys. Chem. B **109**, 23523 (2005).
[14] I. Czekaj, K. Hermann, and M. Witko, Surf. Sci. **545**, 85 (2003).
[15] C. Kolczewski, K. Hermann, S. Guimond, H. Kuhlenbeck, and H.-J. Freund, Surf. Sci. **601**, 5394 (2007).
[16] S. Guimond, J. M. Sturm, D. Göbke, Y. Romanyshyn, M. Naschitzki, H. Kuhlenbeck, and H.-J. Freund, J. Phys. Chem. C **112**, 11835 (2008).
[17] A. Barbieri and M. van Hove, private communication, http://www.icts.hkbu.edu.hk/vanhove/.
[18] J. B. Pendry, J. Phys. C Solid State Phys. **13**, 937 (1980).
[19] C. Igel, V. Heidrich-Meisner, and T. Glasmachers, J. Mach. Learn. Res. **9**, 993 (2008).
[20] I. Czekaj, K. Hermann, and M. Witko, Surf. Sci. **525**, 33 (2003).
[21] E. A. Kröger, D. I. Sayago, F. Allegretti, M. J. Knight, M. Polcik, W. Unterberger, T. J. Lerotholi, K. A. Hogan, C. L. A. Lamont, and D. P. Woodruff, Surf. Sci. **601**, 3350 (2007).
[22] See Fig. S1 in Supplemental Material at http://link.aps.org/supplemental/10.1103/PhysRevLett.114.216101 for structural data of the best-fit models.
[23] S. Surnev, G. Kresse, M. Sock, M. G. Ramsey, and F. P. Netzer, Surf. Sci. **495**, 91 (2001).
[24] J. Seifert, M. Busch, E. Meyer, and H. Winter, Phys. Rev. B **89**, 075404 (2014).
[25] T. Bernhard, J. Seifert, and H. Winter, J. Phys. Condens. Matter **21**, 134001 (2009).
[26] J. Seifert and H. Winter, Nucl. Instrum. Methods Phys. Res., Sect. B **315**, 9 (2013).
[27] J. Heyd, G. E. Scuseria, and M. Ernzerhof, J. Chem. Phys. **118**, 8207 (2003); **124**, 219906 (2006).
[28] G. Kresse and J. Furthmüller, Phys. Rev. B **54**, 11169 (1996).
[29] G. Kresse and D. Joubert, Phys. Rev. B **59**, 1758 (1999).
[30] P. E. Blöchl, Phys. Rev. B **50**, 17953 (1994).
[31] H. Wang, T. A. Mellan, R. Grau-Crespo, and U. Schwingenschlögl, Chem. Phys. Lett. **608**, 126 (2014).
[32] J. P. Perdew, K. Burke, and M. Ernzerhof, Phys. Rev. Lett. **77**, 3865 (1996).
[33] See Tables S3 and S4 in Supplemental Material at http://link.aps.org/supplemental/10.1103/PhysRevLett.114.216101 for tables showing bulk heats of formation and heats of reactions.
[34] F. Iori, M. Gatti, and A. Rubio, Phys. Rev. B **85**, 115129 (2012).
[35] See Fig. S2 in Supplemental Material at http://link.aps.org/supplemental/10.1103/PhysRevLett.114.216101 for phase diagrams of pure GGA and 10% FX.
[36] *CRC Handbook of Chemistry and Physics*, edited by D. R. Lide and H. P. Frederiske, 76th ed. (CRC Press, Boca Raton, FL, 1995).
[37] K. Reuter and M. Scheffler, Phys. Rev. B **65**, 035406 (2001).
[38] M. V. Ganduglia-Pirovano and J. Sauer, Phys. Rev. B **70**, 045422 (2004).

The Surface Structure of V_2O_3(0001) revisited

Felix E. Feiten,[1] Jan Seifert,[1,2] Joachim Paier,[3] Helmut Kuhlenbeck,[1]
Helmut Winter,[2] Joachim Sauer,[3] and Hans-Joachim Freund[1]

[1]*Fritz-Haber-Institut der Max-Planck-Gesellschaft, Faradayweg 4-6, 14195 Berlin, Germany*
[2]*Humboldt-Universität zu Berlin, Institut für Physik, Newtonstr. 15, 12489 Berlin, Germany*
[3]*Humboldt-Universität zu Berlin, Institut für Chemie, Unter den Linden 6, 10099 Berlin, Germany*

SUPPLEMENTAL MATERIAL

Table of Contents

1. Structural data of the best fit V=O and O_3 models resulting from I/V-LEED

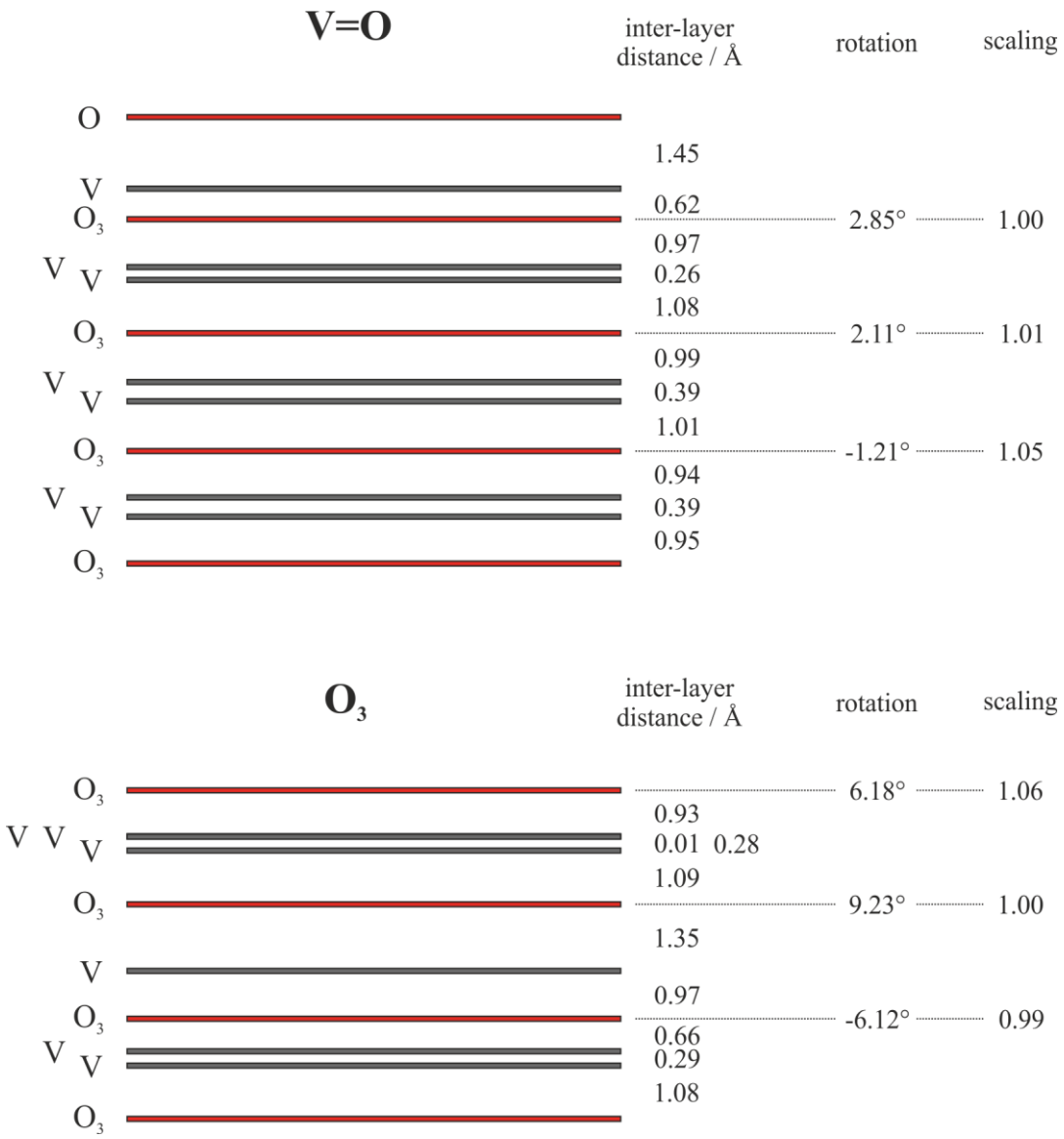

Figure S1. Interlayer spacings of the best-fit structures for V=O and O_3 termination resulting from I/V-LEED. Rotation and scaling of the oxygen trimers are given relative to the bulk values for V_2O_3. Note that the topmost two V layers in the O_3 termination have a very small interlayer distance, making them appear as one in this image.0.01 Å is the distance between those two layers while 0.28 Å is the distance between the second and third vanadium layer.

2. Surface energy changes as a function of the chemical potential $\Delta\mu_O(^1/_2O_2)$

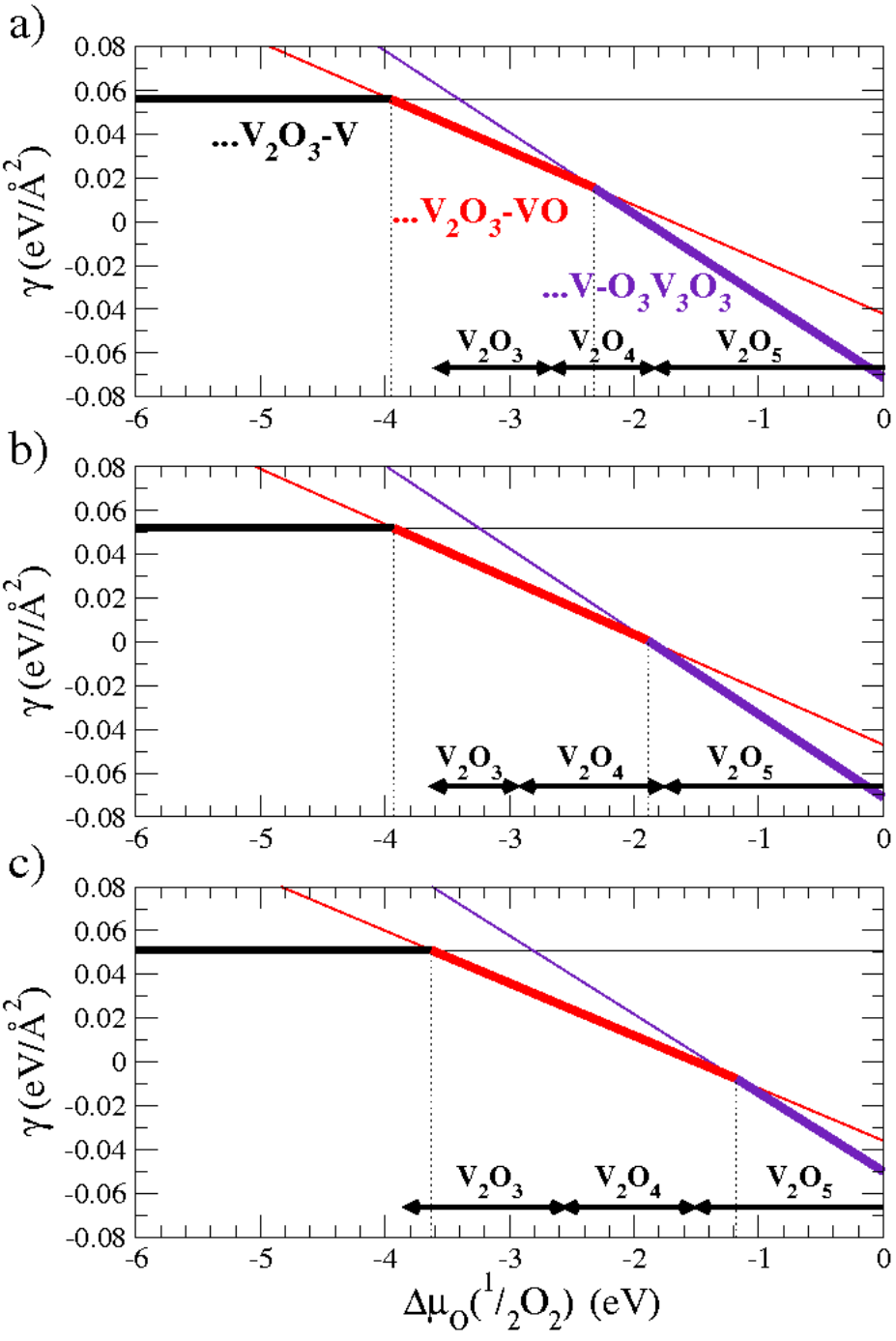

Figure S2. Surface energy γ as a function of the chemical potential $\Delta\mu_O$ for different terminations of the (0001) surface of rhombohedral V_2O_3 obtained using a) the PBE-GGA, b) HSE with 10% Fock-exchange, and c) HSE with 25% Fock-exchange (standard).The black line indicates the termination with a (single) V atom, red and indigo depict V=O– and $O_3V_3O_3$–terminations, respectively.

3. Bulk heats of formation and heats of reaction of vanadium oxide phases

Table S3: Energies were obtained using the PAW pseudopotentials ("V_pv", "O" for bulk vanadium oxide phases, and "O_h" for molecular oxygen) released as of 04/2012. Energies given in eV/formula unit.

	PBE	**HSE (10% FX)**	**HSE (25% FX)**	**obsd.**
ΔH^f_{VO}	-3.24	-3.86	-4.94	-4.47[a]
ΔH^f_{V2O3}	-10.89	-10.86	-11.58	-12.64[a]
ΔH^f_{V2O4}	-13.58	-13.75	-14.15	-14.66[b]
ΔH^f_{V2O5}	-15.43	-15.51	-15.67	-16.07[a]
ΔH^r_1	+5.34	+3.14	+1.70	+3.70
ΔH^r_2	-2.69	-2.89	-2.57	-2.15
ΔH^r_3	+0.42	+0.56	+0.52	+0.43

Comments:

ΔH^r_1 is the reaction enthalpy of reaction 1 etc.

reaction 1: $V_2O_3 \rightarrow 2\ VO + {}^1/_2\ O_2$

reaction 2: $V_2O_3 + {}^1/_2\ O_2 \rightarrow V_2O_4$

reaction3: $V_2O_4 \rightarrow {}^1/_2\ V_2O_3 + {}^1/_2\ V_2O_5$

References

a NIST-JANAF, Thermochemical Tables.

b W. Brückner, H. Oppermann, W. Reichelt, J. I. Terukow, F. A. Tschudnowski, and E. Wolf, *Vanadiumoxide, Darstellung, Eigenschaften, Anwendung* (Akademie, Berlin, 1983).

4. Total energies (FX ≡ Fock-Exchange)

Table S4: Total energies were obtained using the PAW pseudopotentials ("V_pv", "O" for bulk vanadium oxide phases, and "O_h" for molecular oxygen) released as of 04/2012.

[eV/f.u.]	PBE	HSE (10% FX)	HSE (25% FX)
O_2	-10.05131	-11.69311	-14.19973
V (bcc)	-8.95035	-9.66443	-10.796204
VO (spin-pol., AFM)	-17.21218	-19.36840	-22.837748
V_2O_3 (non-spinpol.)	-43.86972	-47.725673	-54.467827
V_2O_4 (non-spinpol.)	-51.58226	-56.46265	-64.14703
α-V_2O_5	-58.46183	-64.06978	-72.76263
V-term. slab $\{V_{20}O_{30}\}$	-434.163835	-473.14869	-540.46018
VO-term. slab $\{V_{20}O_{32}\}$	-452.140265	-492.63618	-561.91116
O_3-term. slab $\{V_{18}O_{30}\}$	-415.63292	-452.68217	-515.67054

Comment:

Total energies for slabs are not given per f.u., but report total energies for the composition given in curly brackets.

For VO, V_2O_3, and V_2O_4 cubic, rhombohedral (corundum), and monoclinic (M1) structures were employed, respectively.

The impact of atomic vibrations upon the I/V-LEED curves is described by the Debye model with the Debye temperature Θ_D as relevant parameter. Bulk Debye temperatures $\Theta_{D,bulk}$ for many materials are documented, $\Theta_{D,bulk}$ for V_2O_3 is 580 K. [119] However, LEED is an intrinsically surface sensitive technique as described above and vibrational amplitudes are larger at the surface than they are in the bulk of a material. Surface Debye temperatures $\Theta_{D,surf}$ are often well approximated by $\Theta_{D,bulk}/\sqrt{2}$. [120] They can also be experimentally determined by measuring the intensities of LEED spots as a function of the temperature. [121]

The intensity of diffraction spots decreases with increasing temperature according to

$$\mathrm{I_{hk}\,(T) = I_{hk,0} \times \exp\left[-\frac{1}{3}\left\langle u^2\right\rangle \left(\Delta\vec{K}_{\mathrm{hk}}\right)^2\right]} \tag{25}$$

where $I_{hk,0}$ is the intensity at 0 K, $\langle u^2 \rangle$ is the mean square amplitude (MSA) of vibrating scatterers and $\Delta\vec{K}_{hk}$ is the scattering vector. The MSA can be calculated according to [122]:

$$\mathrm{\left\langle u^2\right\rangle = \frac{9\hbar^2}{M_{eff}k_B\Theta_{D,surf}} \times \left[\frac{1}{4} + \left(\frac{T}{\Theta_{D,surf}}\right)^2 \int_0^{\frac{\Theta_{D,surf}}{T}} \frac{x}{e^x - 1}\,dx\right]} \tag{26}$$

M_{eff} is the effective mass of the vibrating scatterers. The integral can be replaced by the following rational approximation given by Thacher [123]:

$$\mathrm{\frac{1}{x}\int_0^x \frac{t}{e^t - 1}\,dt = \frac{24.155 - 0.2758x + 0.08386x^2}{24.166 + 5.6522x + x^2} + \varepsilon\ ,|\varepsilon| < 0.00048 \text{ for } 0 \le x \le 10} \tag{27}$$

A fit of experimentally determined temperature-dependent LEED intensities to the function given in equation (25) can be used to determine the surface Debye temperature $\Theta_{D,surf}$.

Temperature dependent intensities for the spots of (1 0) and (1 1) type at a primary beam energy of 100 eV were measured. Data were first taken upon cooling from room temperature to 100 K and then upon heating from 100 K to room temperature, each at a rate of approximately 0.25 K $\mathrm{min^{-1}}$. The experimental data are displayed in Figure 20. For a calculation of the scattering vectors see Appendix 6.3. As Steurer et al. have noted, the choice of M_{eff} for a system containing more than one sort of atom is not

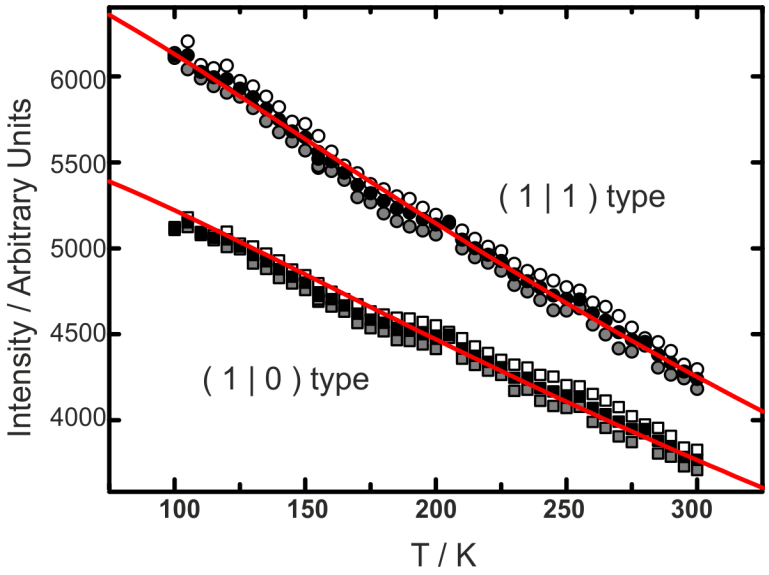

Figure 20: Temperature dependent spot intensities measured with LEED. Empty symbols: data acquired during cooling from 300 K to 100 K, grey symbols: data measured upon heating from 100 K to 300 K, black symbols show the average of the datasets obtained during heating and cooling. Fits (see text) are shown as red lines.

trivial [124]. Using the average of the atomic masses of V and O would give $M_{eff} = 34$ u; using the average weighted with the abundance of V and O in V_2O_3 (V:O = 2:3) leads to $M_{eff} = 30$ u. These values are probably too small since vanadium has a significantly higher scattering cross section than oxygen and therefore a choice of M_{eff} near to the mass of vanadium might be more appropriate. As an upper boundary one could choose the sum of both masses, yielding $M_{eff} = 67$ u. The $\Theta_{D,surf}$ for the three effective masses discussed above are given in Table 2. All surface Debye temperatures listed in Table 2 are smaller than the bulk Debye temperature for V_2O_3 (580 K) [119], as expected. They are also all within ±100 K of $1/\sqrt{2}\,\Theta_{\mathrm{D,bulk}}$. The quality of the fit to the curves does not depend on M_{eff} which is the reason why only a single fit line is shown for each spot in Figure 20.

A critical issue of this approach is the calculation of M_{eff} since no clear rules for its computation are known. Table 2 clearly shows that $\Theta_{D,surf}$ depends strongly on M_{eff} and therefore an inaccurate M_{eff} results in an inaccurate $\Theta_{D,surf}$; the overall spread of $\Theta_{D,surf}$ in Table 2 is 180 K! Another issue is that this method gives only a single value for $\Theta_{D,surf}$. However, the vibrational properties of different surface atoms are different and this can not be adequately described with a single Debye temperature. Because of this

several Debye temperatures for different atomic species were treated as fit parameters in the I/V-LEED calculations, instead of using one fixed value derived from temperature dependant measurements.

M_{eff} / u	Beam	$\Theta_{D,surf}$ / K
30	(1 0)	500
	(1 1)	450
34	(1 0)	470
	(1 1)	420
67	(1 0)	345
	(1 1)	320

Table 2: Surface Debye Temperatures $\Theta_{D,surf}$ obtained with different effective masses for two different beams.

THE JOURNAL OF PHYSICAL CHEMISTRY C

Article

pubs.acs.org/JPCC

Surface Structure of $V_2O_3(0001)$: A Combined I/V-LEED and STM Study

Felix E. Feiten, Helmut Kuhlenbeck,* and Hans-Joachim Freund

Department of Chemical Physics, Fritz Haber Institute of the Max-Planck Society, Faradayweg 4-6, 14195 Berlin, Germany

Supporting Information

ABSTRACT: Using I/V-LEED and scanning tunneling microscopy, we have investigated the surface structure of ~100 Å thick $V_2O_3(0001)$ films on Au(111). Both methods clearly show that the surface is terminated by a layer of vanadyl groups. I/V-LEED quantitative structure determination applied to differently prepared films always leads to a Pendry *R*-factor for the V═O termination close to 0.11 while the *R*-factor for a reconstructed O_3 termination is always larger than 0.2 and increases with increasing data set size. These results are at variance with a recent publication by Window et al. [*Phys. Rev. Lett.* **2015**, *114*, 216101] in which the authors propose that the $V_2O_3(0001)$ surface is terminated by a reconstructed O_3 structure. Surface oxidation experiments also contradict the conclusions of Window et al. since oxidation leads to a previously identified structure with a $(\sqrt{3} \times \sqrt{3})R30°$ LEED pattern which is not expected for oxidation of an O3-terminated surface. In the course of the I/V-LEED calculations the individual Debye temperatures of the surface atoms were determined as part of the structural optimization procedure. We show that this approach is superior to the kinematical analysis of temperature-dependent LEED measurements.

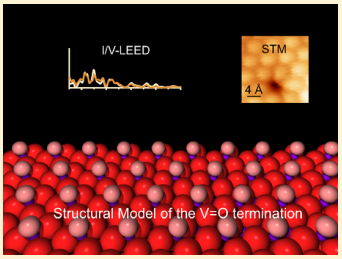

INTRODUCTION

Transition metal oxides play a crucial role in heterogeneous catalysis as support materials for metal nanoparticles, but they also show catalytic activity themselves.[1−4] Knowledge of their atomic scale surface structure is necessary to understand catalytic reactions on them. Vanadium oxides are widely used in industrial oxygen transfer catalysts.[5,6] While phosphorus-doped V_2O_5 is the vanadium oxide most commonly employed in the industry, the $V_2O_3(0001)$ surface also shows catalytic activity.[7,8]

The surface structure is a relevant parameter for catalytic reactions, and therefore the termination of V_2O_3 films prepared in UHV has been discussed in a number of publications.[9−19] Different structural models discussed in these publications are graphically summarized in Figure 1. V_2O_3 crystallizes in the corundum structure. A cut parallel to the 0001 plane can lead to three different surface terminations: a double metal termination (DM) with two vanadium atoms in the surface unit cell, a single metal termination (SM) with one vanadium atom in the surface unit cell, and an oxygen termination (bulk O_3) with three oxygen atoms in the topmost layer. Density functional theory (DFT) calculations[9,10] predict a number of structures to be more stable than these bulk-like terminations: while at very low chemical potentials of oxygen the surface is expected to be vanadium terminated, vanadyl covered surfaces are predicted for higher oxygen potentials. With increasing oxygen pressure the V═O groups are subsequently removed, leading to supercells missing 1/3 or 2/3 of the V═O groups. Both structures exhibit a $(\sqrt{3} \times \sqrt{3})R30°$ superstructure in the LEED pattern and are henceforth called $\sqrt{3}$ structure without differentiating between them. Finally, at even higher oxygen chemical potentials a termination with an oxygen layer at the surface is predicted. In this structure, below the surface every second vanadium atom from the second layer moves up to the first layer to compensate for the charge of the oxygen layer. This is called the reconstructed (rec) O_3 termination.

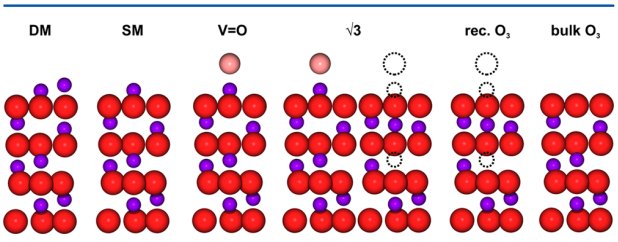

Figure 1. Side-view models of different surface terminations of $V_2O_3(0001)$. Oxygen atoms are depicted in red (pink for V═O oxygen) and vanadium atoms in purple.

For years the accepted view was that the surface is fully covered by vanadyl groups under common UHV conditions. This was based mostly on vibrational spectra (IRAS and HREELS) which show a strong peak for the V═O stretching mode at 127 meV and the fact that atomically resolved STM (scanning tunneling microscopy) images show a simple (1×1) pattern similar to what is expected for a vanadyl-terminated surface.[11,12] NEXAFS (near-edge X-ray absorption fine structure) and XPS (X-ray photoelectron spectroscopy) spectra also fit to a V═O-terminated surface.[13] On the other hand, several ion scattering studies favor the reconstructed O_3 termination.[14−16] In a recent publication we have shown, by

Received: July 17, 2015
Revised: September 4, 2015
Published: September 11, 2015

DOI: 10.1021/acs.jpcc.5b06943
J. Phys. Chem. C 2015, 119, 22961−22969

using I/V-LEED (I/V analysis of LEED [low-energy electron diffraction]), STM, ion scattering, and DFT that the surface is most likely vanadyl terminated.[17]

In this paper we combine STM with I/V-LEED to investigate the V_2O_3 surface structure. Scanning tunneling microscopy can give atomically resolved structural information, but contrary to I/V-LEED, there is no chemical sensitivity to identify the types of atoms and STM does only supply information about the very surface. On the other hand, STM can give quickly (if the tip performs well) an impression of the quality of the film, revealing the types and the density of the defects. Deviations from the ideal surface structure like defect structures, shear planes, stacking faults,[20] etc., or more or less ordered contamination layers may influence experimental I/V curves and thus impair the results of I/V LEED studies. Therefore, the role of STM in such a quantitative LEED experiment may be the control and the optimization of the surface quality. I/V-LEED can be applied best to well-ordered systems, and STM can help to establish such systems and to verify that they are well-ordered.

We have also determined surface Debye temperatures by using them as parameters in the I/V-LEED calculations. Finally, we discuss our results in the context of previous publications on the $V_2O_3(0001)$ surface.

EXPERIMENTAL DETAILS

Experiments were conducted in an Omicron UHV chamber with a background pressure $<5 \times 10^{-11}$ mbar. The chamber is equipped with a room temperature STM (STM-1) and a MCP LEED system as well as an X-ray source with Al and Mg anodes and a hemispherical analyzer for XPS, all from Omicron. Sample cleaning is done via Ar^+ ion bombardment and annealing with a W filament behind the sample. An Au(111) crystal, bought from MaTeck, Germany, was used as substrate for the growth of the $V_2O_3(0001)$ film. The sample temperature was measured with a K-type thermocouple, spot-welded to two Mo plates which fix the crystal on the sample holder. Prior to film deposition the cleanliness and surface ordering of the Au crystal were checked by XPS, LEED, and STM.

Vanadium was deposited in an oxygen atmosphere with an Omicron EFM-3T evaporator at a rate of about 0.7 Å/min, as determined by calibration with a quartz crystal microbalance. Oxygen pressure and sample temperature during vanadium deposition were varied between 523 and 670 K and between 1×10^{-7} and 2×10^{-6} mbar of O_2 for different preparations. Typically 5.4 nm of V, corresponding to 10 nm of V_2O_3, was deposited. After deposition the films were first annealed in O_2 with the same oxygen pressure as during deposition, followed by an annealing step at increased temperature in UHV to improve the order of the film.

While the oxygen pressure was set via filling the whole chamber with O_2 during film deposition, a custom-built pinhole doser was used to generate pressures up to 6×10^{-5} mbar at the sample surface in postannealing steps. Details of the preparation of the samples discussed in this publication can be found in Table 1. In this table the steps B to G for film 3 as well as B to M and Q to S for film 4 are omitted since those preparations are not discussed here. They can be found in the Supporting Information, Table S1.

I/V-LEED quantitative structure determination works best if the electron incidence direction differs from the sample normal by not more than a few tenths of a degree. In order to achieve this condition, one Helmholtz coil was mounted at the chamber.[21] Varying the magnetic field strength by adjusting the current running through the coil as a function of the electron beam energy allows for simultaneous compensation of the magnetic field at the sample position and the correction of small angular sample misalignments. We only employed one coil because a measurement of the magnetic field strength at the sample position showed that only the vertical component was significant (40−50 μT) while the magnetic field in the horizontal directions was very small ($\approx$1 μT). A Sony black and white digital camera was used to take images of the LEED screen; typical exposure times were between 300 and 500 ms per image.

The current of the electron beam to the sample was less than 10 nA in the I/V-LEED experiments. A very slight difference between subsequently recorded I/V curves was recognizable under this condition, which we attribute to a slight oxygen depletion. A clear effect of this reduction on the *R*-factor could not be detected. For testing purposes also some I/V curves with a significantly reduced ion flux were measured. In this case no effect of the electron irradiation could be detected, and the

Table 1. Details of Some Preparation Steps for the Films Discussed in This Work

no.	step	preparation details	LEED pattern/comment
1	A	film deposition: 650 K, 2.5×10^{-7} mbar O_2	
		annealing: 700 K, 3×10^{-7} mbar O_2, 20 min	(1×1)
		annealing: 800 K, 5×10^{-9} mbar, 10 min	
	B	annealing: 870 K, 5×10^{-8} mbar O_2, 10 min	(1×1)
	C	annealing: 870 K, 5×10^{-6} mbar O_2, 15 min	$\sqrt{3}$
	D	annealing: 870 K, 6×10^{-5} mbar O_2, 15 min	formation of V_2O_5 and evaporation
2	A	film deposition: 600 K, 1×10^{-7} mbar O_2	
		annealing: 650 K, 1×10^{-7} mbar O_2, 15 min	(1×1)
		annealing: 870 K, 1.6×10^{-9} mbar, 10 min	
	B	annealing: 850 K, 1.1×10^{-10} mbar, 30 min	(1×1)
3	A	film deposition: 523 K, 2×10^{-7} mbar O_2	(1×1)
		annealing: 523 K, 2×10^{-7} mbar O_2, 15 min	
		...	
	H	annealing: 900 K, 2.9×10^{-10} mbar, 30 min	(1×1)
	I	annealing: 900 K, 5×10^{-7} mbar O_2, 60 min	(1×1)
	J	annealing: 900 K, 5×10^{-7} mbar O_2, 150 min	(1×1)
4	A	film deposition: 573 K, 2×10^{-6} mbar O_2	$\sqrt{3}$
		annealing: 773 K, 2×10^{-6} mbar O_2, 15 min	
		...	
	N	annealing: 950 K, 2×10^{-7} mbar O_2, 105 min	(1×1)
	O	annealing: 923 K, 1.3×10^{-10} mbar, 23 min	(1×1)
	P	XPS measurements for 4 h	(1×1)
		...	

DOI: 10.1021/acs.jpcc.5b06943
J. Phys. Chem. C 2015, 119, 22961−22969

curves were essentially identical to the ones measured with higher electron currents.

Two correction functions to the experimental I/V curves were measured, and the data were corrected accordingly: First, the current of the primary beam depends on the beam energy E_{beam}. This current was determined by measuring the current of electrons flowing from the sample to ground with the sample set to a positive bias voltage in order to limit the contribution of secondary electrons. Second, the MCP detection sensitivity varies with E_{beam} since the electron impact energy at the MCP varies with E_{beam}. This dependence was measured through variation of the front bias of the MCP for a constant beam energy.

COMPUTATIONAL DETAILS

I/V curves were calculated using a modified version of the SATLEED package by A. Barbieri and M. A. van Hove (available for download at http://www.icts.hkbu.edu.hk/vanhove/). Fourteen different trial structures were used as starting structures in the optimization runs: five single metal (SM), two double metal (DM), five vanadyl (VO), and two reconstructed O_3 (O3) terminations, based on structures published in a number of theoretical and experimental publications on the $V_2O_3(0001)$ surface.[9,15,18,22,23] Different models of the same type, e.g., two different VO structures, have different interlayer distances. A table with structural details for all starting structures can be found in the Supporting Information, Table S2. We used an evolutionary strategy algorithm (CMA-ES) to optimize the trial structures by minimization of the Pendry *R*-factor.[24] In the optimization runs the coordinates of all atoms above the fourth O_3 layer below the surface were varied in order to minimize the *R*-factor (see Figure 8). Thus, 15−17 atomic coordinates were optimized depending on the structural model: 15 coordinates for the O3 models, 16 coordinates for the SM models, and 17 coordinates for the VO and DM models. The C_3 symmetry of the system couples the coordinates of the three oxygen atoms in the 2d unit cell in each layer so that only the coordinates of one of these atoms had to be optimized. The vanadium atoms are located on C_3 axes. In this case such a coupling does not exist, but the atom coordinates in the surface plane were not varied in order to not violate the C_3 symmetry. Other optimization parameters were three to five Debye temperatures characterizing the vibrational amplitudes of the atoms, the real and imaginary parts of the inner potential, a linear background, and the in-plane lattice parameter *a*. The five Debye temperatures T_{Debye} are those of the bulk vanadium and oxygen atoms, that of the oxygen atoms in top O_3 layer, that of topmost V atoms in V═O and metal terminations, and that of the O atoms in the vanadyl groups. The structural optimizations runs were started with the highest angular momentum number considered in the calculations set to LMAX = 7 and a 2 eV electron energy step width, followed by another full optimization using the parameters resulting from the first step as start configuration but LMAX = 9 and 1 eV steps. The relativistic phase shifts employed were calculated for bulk V_2O_3 using the phase shift program that comes with the SATLEED package.

RESULTS

As we have shown previously, oxidation of the as-prepared films with a (1 × 1) hexagonal LEED pattern leads to a $\sqrt{3}$ structure followed by the formation of V_2O_5 which sublimates at sufficiently high temperature. This is a first hint that the surface is not terminated by a reconstructed O3 layer since the oxygen content in the O3 structure is higher than in the $\sqrt{3}$ structure if we accept the structural models of the $(\sqrt{3} \times \sqrt{3})R30°$ structure published in refs 9 and 10. Therefore, oxidation of the O3 structure should not lead to a $\sqrt{3}$ structure. LEED patterns observed after different preparation treatments of film no. 1 are shown in Figure 2.[17]

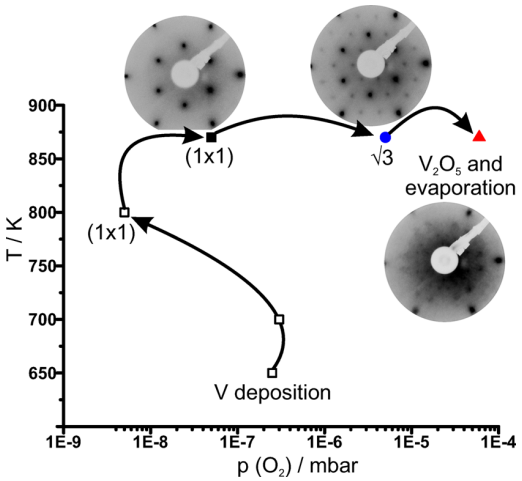

Figure 2. Preparation steps of film no. 1. At some points characteristic LEED patterns (electron energy = 100 eV) are shown.

While V_2O_5 was not directly observed, its formation and evaporation were concluded from the observation that in the oxidation experiment the V_2O_3 LEED pattern disappeared and the Au (substrate) peaks in XPS increased significantly (Figure S1). While V_2O_3 is thermally stable in UHV up to <1000 K, V_2O_5 begins to sublimate in UHV at 823 K.[25]

STM. STM images of the (1 × 1) structure show a honeycomb lattice with two different types of defects. Dark depressions correspond to missing vanadyl groups while bright triangular features are attributed to the reduction of the surface since they can be observed after irradiating the sample with electrons. The type and the density of surface defects depend on the preparation conditions. Figure 3A shows the trimeric features of a reduced surface for film no. 3. Annealing this sample in oxygen led to their disappearance and the appearance of dark depressions (Figure 3B). Further oxidation increased the density of dark depressions (Figure 3C). The LEED patterns of these three surfaces are essentially indistinguishable by visual inspection, and only by STM is it possible to identify these structures, which permits to take specific measures to remove them.

I/V-LEED Symmetry. Two schematic drawings of the V_2O_3 LEED pattern are shown in Figure 4. Figure 4A shows the LEED patterns of $V_2O_3(0001)$ (black circles) and Au(111) (gray stars). The $V_2O_3(0001)$ surface has C_3 symmetry, and thus the six diffraction spots surrounding the (0 0) reflex should consist of two sets of symmetry inequivalent beams. In reality, however, the experimental I/V curves of all six spots appear to be identical. This is due to mirror planes in the Au(111) substrate shown as gray dashed lines in Figure 4A. They are responsible for the presence of two different domains in the V_2O_3 film, related to each other through a mirror operation.

DOI: 10.1021/acs.jpcc.5b06943
J. Phys. Chem. C 2015, 119, 22961−22969

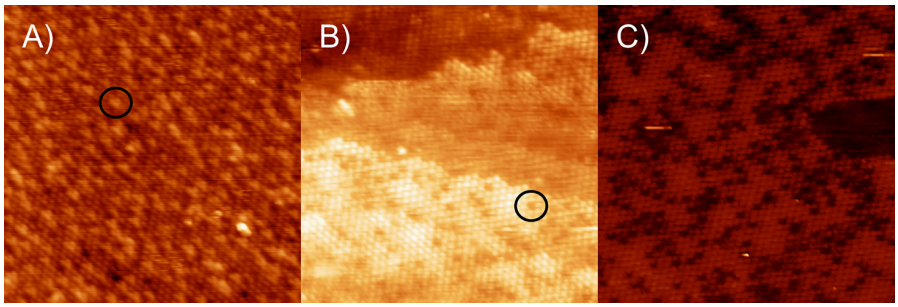

Figure 3. STM images illustrating the oxidation of slightly substoichiometric $V_2O_3(0001)$. 20 nm × 20 nm, +1 V, 0.1 nA. All images are from film no. 3. (A) Preparation step H, reduced surface. (B) Step I, trimeric features gone. (C) Step J, number of missing V═O groups increased. One of each of the two types of defects is encircled in (A) and (B), respectively. See Table 1 for details of the preparation steps.

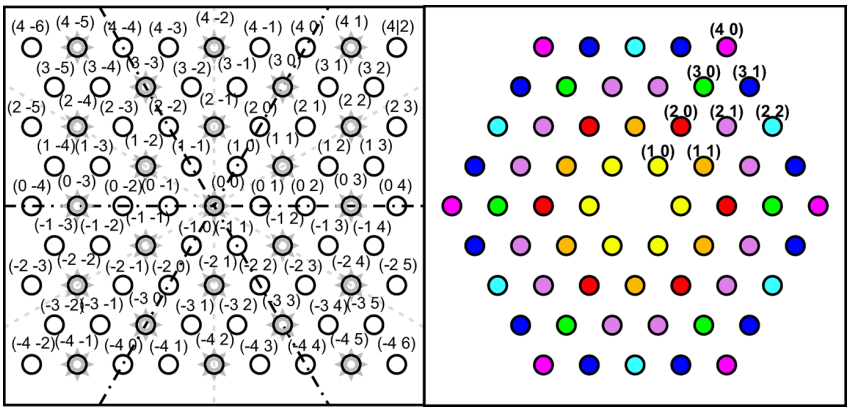

Figure 4. (A) Scheme of the $V_2O_3(0001)$ (black circles) and Au(111) (gray stars) LEED patterns with lines of apparent symmetry as explained in the text. (B) Color-coded scheme showing spots with similar I/V curves in the same color.

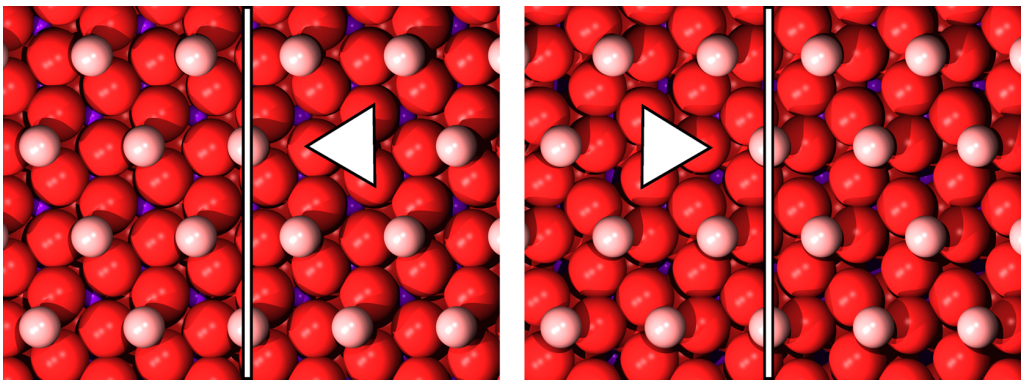

Figure 5. Models of two subsequent vanadyl-terminated surfaces. Oxygen trimers and the mirror plane which transforms them into each other are indicated.

The LEED intensities corresponding to these two domains add up in the LEED pattern, and equal abundance of both domains leads to the observed quasi-6-fold symmetry. This explains the equivalent I/V curves for many of the diffraction spots which are not symmetry-equivalent in C_3, but not for all of them, like the (1 1) and the (−1 2) spots. The identical intensities of these spots are related to the different azimuthal orientations of the oxygen trimers in subsequent layers of the V_2O_3 structure. Figure 5 shows surfaces of two subsequent oxygen layers with vanadyl groups on top. The oxygen layers have a slightly distorted hexagonal structure and can be constructed from the oxygen trimers indicated by triangles. These two surfaces can be transformed into each other by a mirror operation using the mirror plane indicated as a vertical line in Figure 5 plus a translation. Equal abundance (which is quite likely the case) of both types of surface leads to lines of effective symmetry in the LEED pattern, indicated as black dash-dotted lines in Figure 4A. The resulting apparent symmetry of the V_2O_3 LEED pattern is shown in Figure 4B where diffraction spots with identical I/V curves have the same color. We note that the equal abundance of domains related to the Au(111) mirror planes cannot be taken for granted. A miscut of the Au(111) surface may break the mirror symmetry and influence the abundance of the $V_2O_3(0001)$ domains. However, in our

DOI: 10.1021/acs.jpcc.5b06943
J. Phys. Chem. C 2015, 119, 22961−22969

experiments we always found the effective symmetry indicated in Figure 4B.

Debye Temperature Determination. Atomic vibrations influence the diffraction of electrons and have to be considered in I/V-LEED calculations. They are usually described through the Debye temperature Θ_D within the Debye model. In I/V-LEED, instead of the bulk Debye temperature $\Theta_{D,bulk}$, the surface Debye temperature $\Theta_{D,surf}$ is used in order to take into account the different vibrational properties of surface atoms. Van Delft has shown that surface Debye temperatures $\Theta_{D,surf}$ can be roughly estimated by multiplying $\Theta_{D,bulk}$ with $1/\sqrt{2}$.[26] Using a bulk Debye temperature of 580 K for V_2O_3[27] gives $\Theta_{D,surf} \approx 410$ K.

Temperature-dependent measurements of LEED intensities allow the experimental determination of $\Theta_{D,surf}$ as shown by Jepsen and Marcus.[28] As these authors have shown themselves, this method is relatively inaccurate. In our case this procedure is further complicated since it involves an effective mass which is hard to define for systems containing more than one sort of atoms.[29] Furthermore, this approach yields only a single value for $\Theta_{D,surf}$. However, inequivalent surface atoms will have different vibrational properties, and therefore their Debye temperatures will in general be different. The vibrational amplitudes of the atoms (and therefore their Debye temperatures) are relevant input parameters for I/V-LEED computations, and therefore we decided not to use a probably inaccurate Debye temperature $\Theta_{D,surf}$ determined with the method mentioned above, but instead to use the Debye temperatures of the atoms in the model structures as parameters in the optimization runs as described in the Computational Details section. Table 2 gives an overview of the temperatures obtained in this way with the I/V-LEED calculations discussed later in this text. The Debye temperatures for O and V atoms in the vanadyl groups are always smaller than the Debye temperatures of deeper lying atoms, as expected. Together with the Debye temperature for the top O3 layer they are close to the surface Debye temperature of 410 K estimated with the $\Theta_{D,surf} \approx 1/\sqrt{2}\Theta_{D,bulk}$ rule. The values for lower lying atoms, labeled "bulk" in Table 2, closely match the bulk Debye temperature of 580 K. The good agreement between the bulk values listed in Table 2 and the literature bulk value indicates that this method delivers reasonably accurate values. The spread of the values for different preparations in Table 2 may give an impression of the accuracy of the Debye temperatures determined with I/V-LEED.

Table 2. Debye Temperatures Θ_D Determined with I/V-LEED Optimization Runs, Assuming a Vanadyl-Terminated Surface (Values Listed for Samples #2B, #3H, and #4O)

	Θ_D (K)		
type of atom[a]	exp #2B	exp #3H	exp #4O
vanadyl O	305	315	310
vanadyl V	364	288	366
top O_3 layer O	440	457	443
bulk V	553	596	560
bulk O	631	615	626

[a]"Bulk" refers to all atoms below the topmost O3 layer.

I/V-LEED and STM Measurements. I/V-LEED measurements were always combined with STM in order to document the surface quality before I/V-LEED data were recorded. The STM images in Figure 6 show a surface with missing V═O groups (Figure 6A, sample #2B, taken before I/V-LEED), a somewhat reduced surface with many trimeric features (Figure 6B, sample #3H, taken before I/V-LEED), and a surface with fewer trimeric defects (Figure 6C, #4O, taken after I/V-LEED). I/V-LEED structural optimization as described above was performed for all three of these preparations; the best-fit Pendry *R*-factors are listed in Table 3, and the experimental I/V curves are plotted in Figure 7 together with the curves calculated for the best-fit V═O terminated structure. The Pendry *R*-factors for structural models with double metal (DM) termination were always so large that they are not discussed here.

Table 3. Best-Fit *R*-Factors for Three Preparations and Three Models and the Respective Energy Ranges of the I/V-LEED Measurements

preparation	R_{pendry} (V═O)	R_{pendry} (O3)	R_{pendry} (SM)	total energy range (eV)
#2B	0.12	0.23	0.20	766
#3H	0.10	0.26	0.14	1128
#4O	0.12	0.36	0.23	1819

The energy ranges of the LEED measurements were 50 eV → 300 eV for preparation #2B, 50 eV → 400 eV for preparation #3H, and 50 eV → 500 eV for preparation #4O. This leads to the tabulated total energy ranges as the sum of the energy ranges of symmetry inequivalent spots listed in Table 3. The smallest *R*-factor for all three preparations is the *R*-factor for models with vanadyl termination, which is a clear hint that the $V_2O_3(0001)$ surface is in fact vanadyl terminated. Another indication comes from the dependence of the *R*-factor on the

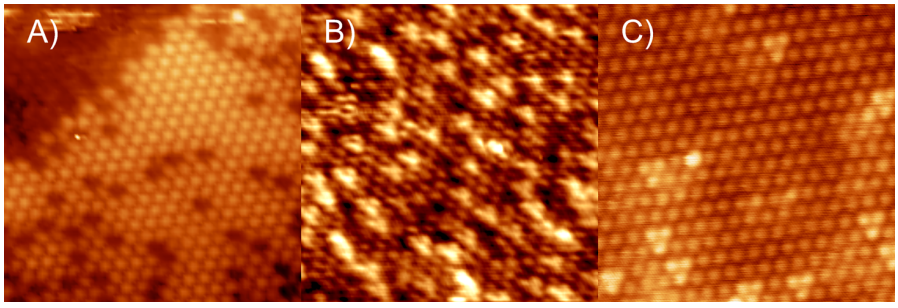

Figure 6. Atomically resolved STM images of different $V_2O_3(0001)$ films: (A) film #2B, taken before I/V-LEED; (B) film #3H, taken before I/V-LEED; (C) film #4O, taken after I/V-LEED. All images 10 nm × 10 nm, +1 V, 0.1 nA.

DOI: 10.1021/acs.jpcc.5b06943
J. Phys. Chem. C 2015, 119, 22961−22969

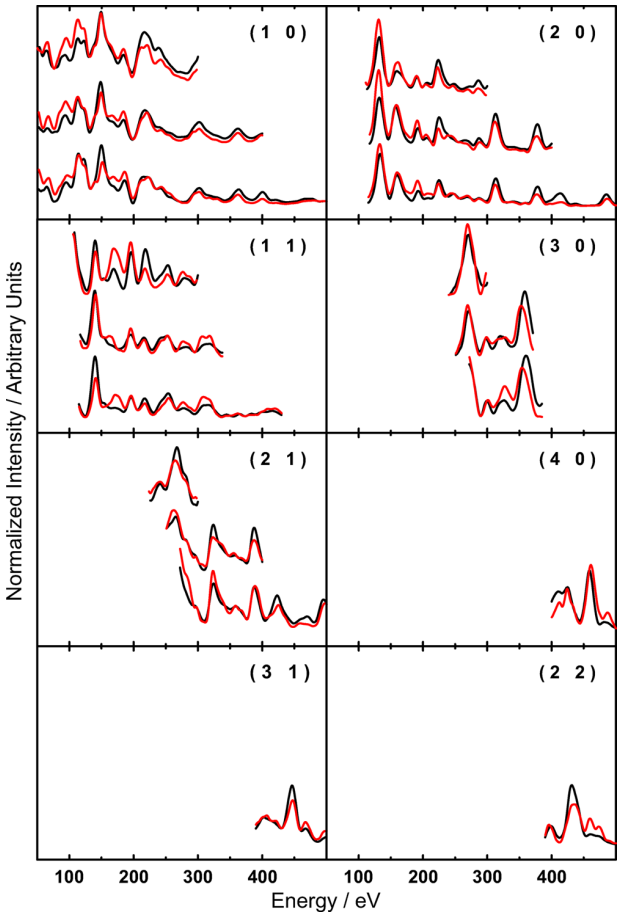

Figure 7. Experimental (black) and computed best-fit (red) I/V curves for a structural model with V═O termination. In each graph the top curves correspond to preparation #2B, the middle curves to preparation #3H, and the bottom curves to preparation #4O.

energy range: the *R*-factors for the models with vanadyl termination do essentially not depend on the energy range, as expected for the correct model, while for the O3 termination the *R*-factor increases with increasing energy range due to the well-known problem of fitting a data set with the wrong function. This may work satisfactorily for a small fit range, but the error will unavoidably increase when the fit range is increased.

We note that the *R*-factors for the SM model are always smaller than those for the O3 model but larger than those for the VO model. This is likely related to the similarity of the VO model and the SM model which differ just by the presence/absence of the vanadyl oxygen atoms, which are comparably weak scatterers, while the structural difference between the VO model and the O3 model is larger (absence of vanadyl groups in the O3 model and upward movement of vanadium atoms below the surface). Best-fit structural parameters for preparation #4O are given in Table S3 for all 14 models tested.

While the I/V-LEED calculations discussed above have been performed with the bulk in plane lattice constant of a = 4.9570 Å,[23] we have also performed calculations for different values of a using the data set of preparation #4O. This lead to a very slight improvement of the *R*-factor to 0.11 for a lattice constant of a = 4.9756 Å. The very small difference of 0.4% between the best-fit lattice constant and the value reported in the literature is another indicator that the V═O structure is the correct model.

The parameters for this structure are tabulated in Table 4 with the corresponding distances visualized in Figure 8. A graph showing the dependence of the *R*-factor on the lattice parameter can be found in Figure S2.

Table 4. Best-Fit Structural Data for Preparation #4O[a]

	VO model	SM model	O3 model
V═O	1.46		
$O3_1$–V	0.61	0.96	
$O3_1$ rotation	+3.5°	+0.2°	+6.2°
$O3_1$ scaling	+1%	−15%	+6%
V_{1A}–$O3_1$	0.98	0.91	0.93
V_{1B}–V_{1A}	0.26	0.29	0.01
V_{1C}–V_{1B}			0.28
$O3_2$–$V_{1B(C)}$	1.06	1.10	1.09
$O3_2$ rotation	+2.4°	+4.3°	+9.2°
$O3_2$ scaling	+3%	+9%	±0%
$V_{2(A)}$–$O3_2$	1.00	0.96	1.35
V_{2B}–V_{2A}	0.39	0.36	
$O3_3$–$V_{2(B)}$	0.99	0.98	0.97
$O3_3$ rotation	−2.0°	0.3°	−6.2°
$O3_3$ scaling	+6%	+9%	−1%
V_{3A}–$O3_3$	0.95	0.98	0.96
V_{3B}–V_{3A}	0.39	0.37	0.29
$O3_4$–V_{3B}	0.95	0.92	1.08

[a]Structural data (layer distances in Å, scaling and rotation of the oxygen trimers) for the VO model using the optimized lattice constant a = 4.9756 Å and for the SM and O_3 models using the bulk value a = 4.9570 Å. Oxygen trimer (O_3) clockwise rotation and scaling are given relative to the bulk values.

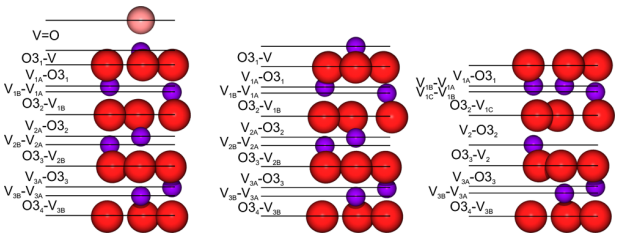

Figure 8. Structural models of the best-fit structures for VO, SM, and O3 termination models using I/V-LEED data for preparation #4O. The corresponding structural data are collected in Table 4.

Comparison of the layer distances in the best-fit V═O terminated structure with those of the bulk structure reveals a decrease of the $O3_1$–V distance by 38%. The next interlayer distance V_{1A}–$O3_1$ is identical to the bulk value of 0.98 Å while the following V_{1B}–V_{1A} distance is again reduced (by 28% compared to the bulk value of 0.36 Å). The remaining changes of interlayer distances are listed in Table S4. They are all smaller than 10%. The changes of the lateral positions of the oxygen atoms compared to the bulk values are rather small for the V═O-terminated model (trimer rotations of 3.5°, 2.4°, and 2.0° and trimer size changes of +1%, +3%, and +6% for the first, second, and third O_3 layer, respectively). The size changes in the best-fit SM struture are significantly larger (−15%, +9%, and +9%, respectively) while the best-fit O3 structure involves much larger rotations (6° and 9°) for the first two O_3 layers.

DOI: 10.1021/acs.jpcc.5b06943
J. Phys. Chem. C 2015, 119, 22961−22969

While the V═O bond length determined here with I/V-LEED (1.46 Å) is slightly shorter than that determined with DFT (1.59, 1.61, and 1.57 Å, respectively),[9,17,19] the changes in interlayer distances resulting from structural optimization in the DFT calculations of Kresse et al.[9] and Feiten et al.[17] match the values determined with I/V-LEED remarkably well as shown by the numbers in Table 5.

Table 5. Comparison of Interlayer Relaxations (in %) Determined with I/V-LEED and DFT[a]

	this study	DFT (PW91)[9]	DFT (HSE)[17]
$O3_1$–V	−38	−31	−34
V_{1A}–$O3_1$	±0	+1	−1
V_{1B}–V_{1A}	−28	−25	−25
$O3_2$–V_{1B}	+8	+10	+9

[a]The changes given are given relative to the corresponding bulk distances. $O3–V_{bulk}$ = 0.98 Å and $V–V_{bulk}$ = 0.36 Å.[23]

A large contraction of the $O3_1$–M distance between the topmost metal atom and the underlying O3 layer has also been found for other oxides with corundum structure, both experimentally (Cr_2O_3[30] and Fe_2O_3[31,32]) and theoretically (Cr_2O_3,[33] Fe_2O_3[34,35]).

DISCUSSION

Our results are in marked contrast to the results of ion scattering studies performed by Window et al., who have found their ion scattering data (medium energy ion scattering (MEIS) and noble gas impact-collision ion scattering spectroscopy (NICISS) data) to be in clear favor of a reconstructed O_3 termination.[15,16] While we cannot explain this discrepancy for the MEIS experiment, the rather thin films (~25 Å compared to ≥100 Å in our studies as well as in the studies using MEIS) and the different substrate ($Cu_3Au(100)$) in the NICISS experiment could be responsible for a different surface termination. This could also be the reason for the unusual STM images obtained by Niehus et al. which they attribute to "a full vanadium layer stabilized by one-third of an oxygen layer".[36]

Window et al. have performed Tersoff–Hamann STM simulations for a V═O-terminated V_2O_3 surface as well as for both bulk-like and reconstructed O3-terminated surfaces (see Figure 1 for the structures). While the simulated STM images of Window et al.[15] show more fine structure for the two O3 terminations than the STM simulations of Surnev et al.,[37] both studies predict round shapes for vanadyl-terminated surfaces and triangular features for O3 terminations. The triangular features observed in our STM images can clearly be attributed to reduction and do not correspond to the O3 model. We have never observed any STM images similar to the simulated STM images for O3-terminated structures. Although the defects that we observe in STM images sometimes do display local order, we have never seen extended ordered areas that could be related to a different coexisting surface structure, which renders the model of coexisting O3 and V═O surface phases as proposed by Window et al.[16] unlikely. Coexisting surface structures, which might be interpreted as arising from differently terminated regions on the surface, have been observed by Surnev et al.[37] Their occurrence could be due to the relatively low thickness of the films investigated (3 monolayer equivalents on Pd(111)).

A quantitative surface structure determination of $V_2O_3(0001)$ using photoelectron diffraction was in favor of a single metal terminated structure but could not exclude the presence of oxygen atoms atop of the V atoms, i.e., V═O groups.[18] While the overall conclusion is in good agreement with our findings, our data clearly favor a vanadyl termination over a single metal terminated structure without oxygen atoms atop. By including the Debye temperatures of the surface atoms in the optimization process, we feel that we have adequately treated vibrational amplitudes within the I/V-LEED calculations, an issue that was raised in the comparison of photoelectron diffraction results with I/V-LEED results for $Al_2O_3(0001)$[38] and $Cr_2O_3(0001)$.[30]

Another ion scattering method, ion beam triangulation (IBT), has also been employed to study the structure of the $V_2O_3(0001)$ surface.[14] The authors came to the conclusion that the surface should be terminated by an O_3 layer. IBT was assumed to be very surface sensitive, but recently it has been shown that this may not be as true as formerly assumed.[39] In the case of $V_2O_3(0001)$ an O3 plane is located below the vanadyl groups, which may be the reason for the results of the IBT study if the contribution of the surface vanadyl groups to the measured signal is less dominant than previously assumed. A different ion scattering experiment, fast atom diffraction, performed on $V_2O_3(0001)$ by the same group strongly supports the conclusion that $V_2O_3(0001)$ is vanadyl terminated, as we have reported recently.[17]

Two DFT studies have predicted phase diagrams for the surface structure of $V_2O_3(0001)$ as a function of the chemical potential of oxygen in the gas phase above the oxide. While Kresse et al. have performed calculations on V_2O_3 slabs,[9] Todorova et al. have considered thin films of V_2O_3 supported on Al_2O_3.[10] Both studies predict the existence of a surface covered by vanadyl groups, which are gradually removed with increasing oxygen chemical potential leading to partially V═O covered surfaces and finally to a reconstructed O3 termination. The stability ranges for different surface terminations reported in refs 9 and 10 indicate that the thermodynamically stable structure is an O3-terminated surface at the typical oxygen pressures and temperatures used in the preparation of the $V_2O_3(0001)$ films. Also, neither of the studies predicts full V═O coverage to be the most stable surface structure at any oxygen chemical potential, rather they favor partial V═O coverage over a range of conditions. However, we note that the GGA and PW91 functionals employed in those studies overestimate the stability of phases with a high oxygen content. Furthermore, the authors of both theoretical studies clearly stated that DFT calculations with semilocal functionals have problems to describe V_2O_3. In particular, the $V_2O_3(0001)$ surface became a ferromagnetic insulator if spin polarization was considered in the DFT calculations, which is in stark contrast with the experimental observation that it is paramagnetic and metallic. We have recently performed DFT calculations using a hybrid functional which appears to describe V_2O_3 more accurately than the functionals previously employed.[17] This is reflected in the better reproduction of the experimental heats of formation of various V_xO_y species. In these calculations the range of the oxygen chemical potential in which the vanadyl-covered surface is predicted to be thermodynamically stable is significantly enlarged compared to earlier DFT studies and the region where an O3-terminated structure is thermodynamically stable corresponds to conditions where V_2O_5 is the stable bulk phase. This explains well

DOI: 10.1021/acs.jpcc.5b06943
J. Phys. Chem. C 2015, 119, 22961−22969

why the O3 structure could not be prepared in this study since V_2O_5 formation prevented the formation of the O3 structure.

CONCLUSION

Our combined I/V-LEED and STM measurements clearly indicate that the $V_2O_3(0001)$ surface is covered by vanadyl groups under typical UHV preparation conditions. This is in marked contrast to conclusions derived from ion scattering experiments by Window et al.[15,16] While the surface could be oxidized to show a $(\sqrt{3} \times \sqrt{3})R30°$ LEED pattern indicative of one of the $\sqrt{3}$ structures, we were not able to prepare an O_3 terminated surface due to the formation and sublimation of V_2O_5 at the required preparation conditions. Through atomically resolved STM images we could distinguish two different types of surface defects. While the surfaces are never completely free of defects, the number of defects could be reduced by annealing in UHV or in an oxygen atmosphere depending on the type of the defects.

We have determined surface Debye temperatures for $V_2O_3(0001)$ by using them as fit parameters in the structural optimizations of the I/V-LEED calculations. This method avoids the shortcomings of the kinematical determination through temperature-dependent measurements of the LEED intensity. Using five different Debye temperatures, we obtained values of $\Theta_{D,surf} \approx 300$ K for the atoms in vanadyl groups, $\Theta_{D,surf} \approx 400$ K for the top oxygen trilayer and $\Theta_{D,bulk} \approx 600$ K for the bulk. The good agreement with the literature value of $\Theta_{D,bulk} = 580$ K[27] indicates the reliability of this method.

ASSOCIATED CONTENT

Supporting Information

The Supporting Information is available free of charge on the ACS Publications website at DOI: 10.1021/acs.jpcc.5b06943.

Preparative details for additional preparation steps; structural data for the start structures used in the I/V-LEED calculations; XPS spectrum indicating V_2O_5 evaporation; structural parameters for best fits resulting from all 14 start structures for preparation #4O; graph showing the dependence of the *R*-factor on the lattice parameter *a*; comparison of interlayer distances (PDF)

AUTHOR INFORMATION

Corresponding Author

*E-mail: kuhlenbeck@fhi-berlin.mpg.de (H.K.).

Notes

The authors declare no competing financial interest.

ACKNOWLEDGMENTS

This work was funded by the Deutsche Forschungsgemeinschaft through their Sonderforschungsbereich 546 "Transition Metal Oxide Aggregates". We gratefully acknowledge the Fonds der Chemischen Industrie for financial support. The LEED calculations were performed using programs derived from the Barbieri/Van Hove Symmetrized Automated LEED package.

REFERENCES

(1) Cuenya, B. R. Synthesis and Catalytic Properties of Metal Nanoparticles: Size, Shape, Support, Composition, and Oxidation State Effects. *Thin Solid Films* **2010**, *518*, 3127−3150.

(2) Freund, H.-J.; Pacchioni, G. Oxide Ultra-Thin Films on Metals: New Materials for the Design of Supported Metal Catalysts. *Chem. Soc. Rev.* **2008**, *37*, 2224−2242.

(3) Royer, S.; Duprez, D. Catalytic Oxidation of Carbon Monoxide over Transition Metal Oxides. *ChemCatChem* **2011**, *3*, 24−65.

(4) Kuhlenbeck, H.; Shaikhutdinov, S.; Freund, H.-J. Well-Ordered Transition Metal Oxide Layers in Model Catalysis - a Series of Case Studies. *Chem. Rev.* **2013**, *113*, 3986−4034.

(5) Wachs, I. E.; Weckhuysen, B. M. Structure and Reactivity of Surface Vanadium Oxide Species on Oxide Supports. *Appl. Catal., A* **1997**, *157*, 67−90.

(6) Haber, J. Fifty Years of my Romance with Vanadium Oxide Catalysts. *Catal. Today* **2009**, *142*, 100−113.

(7) Göbke, D.; Romanyshyn, Y.; Guimond, S.; Sturm, J. M.; Kuhlenbeck, H.; Döbler, J.; Reinhardt, U.; Ganduglia-Pirovano, M. V.; Sauer, J.; Freund, H.-J. Formaldehyde Formation on Vanadium Oxide Surfaces $V_2O_3(0001)$ and $V_2O_5(001)$: How does the Stable Methoxy Intermediate Form? *Angew. Chem., Int. Ed.* **2009**, *48*, 3695−8.

(8) Romanyshyn, Y.; Guimond, S.; Kuhlenbeck, H.; Kaya, S.; Blum, R. P.; Niehus, H.; Shaikhutdinov, S.; Simic-Milosevic, V.; Nilius, N.; Freund, H.-J.; et al. Selectivity in Methanol Oxidation as Studied on Model Systems Involving Vanadium Oxides. *Top. Catal.* **2008**, *50*, 106−115.

(9) Kresse, G.; Surnev, S.; Schoiswohl, J.; Netzer, F. P. $V_2O_3(0001)$ Surface Terminations: a Density Functional Study. *Surf. Sci.* **2004**, *555*, 118−134.

(10) Todorova, T. K.; Ganduglia-Pirovano, M. V.; Sauer, J. Vanadium Oxides on Aluminum Oxide Supports. 1. Surface Termination and Reducibility of Vanadia Films on α-$Al_2O_3(0001)$. *J. Phys. Chem. B* **2005**, *109*, 23523−31.

(11) Schoiswohl, J.; Sock, M.; Surnev, S.; Ramsey, M.; Netzer, F.; Kresse, G.; Andersen, J. $V_2O_3(0001)$ Surface Terminations: From Oxygen- to Vanadium-Rich. *Surf. Sci.* **2004**, *555*, 101−117.

(12) Dupuis, A.-C.; Abu-Haija, M.; Richter, B.; Kuhlenbeck, H.; Freund, H.-J. $V_2O_3(0001)$ on Au(111) and W(110): Growth, Termination and Electronic Structure. *Surf. Sci.* **2003**, *539*, 99−112.

(13) Kolczewski, C.; Hermann, K.; Guimond, S.; Kuhlenbeck, H.; Freund, H.-J. Identification of the Vanadyl Terminated $V_2O_3(0001)$ Surface by NEXAFS Spectroscopy: A Combined Theoretical and Experimental Study. *Surf. Sci.* **2007**, *601*, 5394−5402.

(14) Seifert, J.; Meyer, E.; Winter, H.; Kuhlenbeck, H. Surface Termination of an Ultrathin V_2O_3-film on Au(111) Studied via Ion Beam Triangulation. *Surf. Sci.* **2012**, *606*, L41−L44.

(15) Window, A.; Hentz, A.; Sheppard, D.; Parkinson, G.; Woodruff, D.; Unterberger, W.; Noakes, T.; Bailey, P.; Ganduglia-Pirovano, M.; Sauer, J. The Structure of Epitaxial V_2O_3 Films and Their Surfaces: A Medium Energy Ion Scattering Study. *Surf. Sci.* **2012**, *606*, 1716−1727.

(16) Window, A. J.; Hentz, A.; Sheppard, D. C.; Parkinson, G. S.; Niehus, H.; Ahlbehrendt, D.; Noakes, T. C. Q.; Bailey, P.; Woodruff, D. P. $V_2O_3(0001)$ Surface Termination: Phase Equilibrium. *Phys. Rev. Lett.* **2011**, *107*, 016105.

(17) Feiten, F. E.; Seifert, J.; Paier, J.; Kuhlenbeck, H.; Winter, H.; Sauer, J.; Freund, H.-J. Surface Structure of $V_2O_3(0001)$ Revisited. *Phys. Rev. Lett.* **2015**, *114*, 216101.

(18) Kröger, E. A.; Sayago, D. I.; Allegretti, F.; Knight, M. J.; Polcik, M.; Unterberger, W.; Lerotholi, T. J.; Hogan, K. A.; Lamont, C. L. A.; Woodruff, D. P. The Structure of the $V_2O_3(0001)$ Surface: A Scanned-Energy Mode Photoelectron Diffraction Study. *Surf. Sci.* **2007**, *601*, 3350−3360.

(19) Czekaj, I.; Hermann, K.; Witko, M. Ab Initio Density Functional Theory Studies on Oxygen Stabilization at the $V_2O_3(0001)$ Surface. *Surf. Sci.* **2003**, *545*, 85−98.

(20) Ascolani, H.; Cerda, J. R.; de Andres, P. L.; de Miguel, J. J.; Miranda, R.; Heinz, K. Detecting stacking faults during epitaxial growth by low energy electron diffraction. *Surf. Sci.* **1996**, *345*, 320−330.

(21) Blum, B. Single Crystal Alignment Method for LEED Experiments with Ungraded Tilt Sample-Holders. *Surf. Rev. Lett.* **1997**, *4*, 629−635.

(22) Czekaj, I.; Hermann, K.; Witko, M. Relaxation and Electronic Structure of the $V_2O_3(0001)$ Surface: Ab Initio Cluster Model Studies. *Surf. Sci.* **2003**, *525*, 33−45.

DOI: 10.1021/acs.jpcc.5b06943
J. Phys. Chem. C 2015, 119, 22961−22969

(23) Tenailleau, C.; Suard, E.; Rodriguez-Carvajal, J.; Crosnier-Lopez, M. P.; Lacorre, P. Effect of Mo Doping on the Room-Temperature Structure of Vanadium Sesquioxide. *Chem. Mater.* **2002**, *14*, 3569−3575.
(24) Igel, C.; Heidrich-Meisner, V.; Glasmachers, T. Shark. *J. Mach. Learn. Res.* **2008**, *9*, 993−996.
(25) Guimond, S.; Sturm, J. M.; Göbke, D.; Romanyshyn, Y.; Naschitzki, M.; Kuhlenbeck, H.; Freund, H.-J. Well-Ordered V_2O_3(001) Thin Films on Au(111): Growth and Thermal Stability. *J. Phys. Chem. C* **2008**, *112*, 11835−11846.
(26) van Delft, F. Bulk and Surface Debye Temperatures in Relation to Cohesive Energy and Lennard-Jones Potentials. *Surf. Sci.* **1991**, *251*−*252*, 690−695.
(27) Keer, H.; Dickerson, D.; Kuwamoto, H.; Barros, H.; Honig, J. Heat Capacity of Pure and Doped V_2O_3 Single Crystals. *J. Solid State Chem.* **1976**, *19*, 95−102.
(28) Jepsen, D. W.; Marcus, P. M.; Jona, F. The Determination of Surface Debye Temperatures from Low-Energy Electron Diffraction Data. *Surf. Sci.* **1974**, *41*, 223−236.
(29) Steurer, W.; Apfolter, A.; Koch, M.; Ernst, W. E.; Holst, B. Surface Debye Temperature of α-Quartz(0001). *Surf. Sci.* **2008**, *602*, 1080−1083.
(30) Rohr, F.; Bäumer, M.; Freund, H.-J.; Mejias, J.; Staemmler, V.; Müller, S.; Hammer, L.; Heinz, K. Strong Relaxations at the Cr_2O_3(0001) Surface as Determined via Low-Energy Electron Diffraction and Molecular Dynamics Simulations. *Surf. Sci.* **1997**, *372*, L291−L297.
(31) Lübbe, M.; Moritz, W. A LEED Analysis of the Clean Surfaces of α-Fe_2O_3(0001) and α-Cr_2O_3(0001) Bulk Single Crystals. *J. Phys.: Condens. Matter* **2009**, *21*, 134010.
(32) Ketteler, G.; Weiss, W.; Ranke, W. Surface Structures of α-Fe_2O_3(0001) Phases Determined by LEED Crystallography. *Surf. Rev. Lett.* **2001**, *8*, 661−683.
(33) Rehbein, C.; Harrison, N.; Wander, A. Structure of the α-Cr_2O_3(0001) Surface: An Ab Initio Total-Energy Study. *Phys. Rev. B: Condens. Matter Mater. Phys.* **1996**, *54*, 14066−14070.
(34) Rohrbach, A.; Hafner, J.; Kresse, G. Ab Initio Study of the (0001) Surfaces of Hematite and Chromia: Influence of Strong Electronic Correlations. *Phys. Rev. B: Condens. Matter Mater. Phys.* **2004**, *70*, 1−17.
(35) Bergermayer, W.; Schweiger, H.; Wimmer, E. Ab Initio Thermodynamics of Oxide Surfaces: O_2 on Fe_2O_3(0001). *Phys. Rev. B: Condens. Matter Mater. Phys.* **2004**, *69*, 1−12.
(36) Niehus, H.; Blum, R.-P.; Ahlbehrendt, D. Structure of Vanadium Oxide (V_2O_3) Grown on Cu_3Au(100). *Surf. Rev. Lett.* **2003**, *10*, 353−359.
(37) Surnev, S.; Kresse, G.; Sock, M.; Ramsey, M. G.; Netzer, F. P. Surface Structures of Ultrathin Vanadium Oxide Films on Pd(111). *Surf. Sci.* **2001**, *495*, 91−106.
(38) Walters, C. F.; Mccarty, K. F.; Soares, E. A.; Van Hove, M. A. The Surface Structure of α-Al_2O_3 Determined by Low-Energy Electron Diffraction: Aluminum Termination and Evidence for Anomolously Large Thermal Vibrations. *Surf. Sci.* **2000**, *464*, L732−L738.
(39) Seifert, J.; Busch, M.; Meyer, E.; Winter, H. Surface Structure of Alanine on Cu(110) via Grazing Scattering of Fast Atoms and Molecules. *Phys. Rev. B: Condens. Matter Mater. Phys.* **2014**, *89*, 075404.

DOI: 10.1021/acs.jpcc.5b06943
J. Phys. Chem. C 2015, 119, 22961−22969

Supporting Information:

The Surface Structure of V_2O_3(0001) - a Combined I/V-LEED and STM Study

Felix E. Feiten, Helmut Kuhlenbeck, and Hans-Joachim Freund

Department of Chemical Physics, Fritz-Haber-Institut der Max-Planck-Gesellschaft, Faradayweg 4-6, 14195 Berlin, Germany

Table S1. Details of the preparation steps missing in Table 1.

#	step	preparation details	LEED pattern / comment	
3	A	film deposition 523 K, 2 x 10^{-7} mbar O_2 annealing 523 K, 2 x 10^{-7} mbar O_2, 15 min	(1×1)	
	B	annealing 673 K, UHV, 10 min	(1×1)	
	C	annealing 773 K, UHV, 10 min	(1×1)	
	D	annealing 823 K, UHV, 30 min	(1×1)	
	E	annealing 823 K, 6.2 x 10^{-11} mbar, 90 min	(1×1)	
	F	annealing 823 K, 5 x 10^{-7} mbar O_2, 120 min	(1×1)	
	G	annealing 823 K, 5 x 10^{-7} mbar O_2, 60 min	(1×1)	
	H	annealing 900 K, 2.9 x 10^{-10} mbar, 30 min	(1×1)	
	I	annealing 900 K, 5 x 10^{-7} mbar O_2, 60 min	(1×1)	
	J	annealing 900 K, 5 x 10^{-7} mbar O_2, 150 min	(1×1)	
4	A	film deposition 573 K, 2 x 10^{-6} mbar O_2 annealing 773 K, 2 x 10^{-6} mbar O_2, 15 min	√3	
	B	annealing 900 K, 8.8 x 10^{-10} mbar, 30 min	√3	
	C	annealing 973 K, 8.0 x 10^{-10} mbar, 30 min	√3	
	D	annealing 923 K, 1.6 x 10^{-9} mbar, 30 min	(1×1)	
	E	Ar^+ bombardment, 1000 V, 5.8 µA sputter current, 5 min	reduced	
	F	Ar^+ bombardment, 1000 V, 5.8 µA sputter current, 30 min	heavily reduced	
	G	annealing 923 K, 8 x 10^{-10} mbar, 30 min	bad (1×1)	
	H	annealing 950 K, 2 x 10^{-7} mbar O_2, 45 min annealing 923 K, 3.1 x 10^{-9} mbar O_2, 45 min	(1×1)	
	I	annealing 923 K, 5 x 10^{-7} mbar O_2, 35 min annealing 950 K, 5 x 10^{-7} mbar O_2, 25 min	(1×1)	
	J	annealing 950 K, 1.1 x 10^{-10} mbar, 15 min	(1×1)	
	K	annealing 950 K, 1.1 x 10^{-10} mbar, 15 min	(1×1)	
	L	annealing 923 K, 2 x 10^{-7} mbar O_2, 30 min	(1×1)	
	M	annealing 923 K, 2 x 10^{-7} mbar O_2, 90 min	(1×1)	
	N	annealing 950 K, 2 x 10^{-7} mbar O_2, 105 min	(1×1)	
	O	annealing 923 K, 1.3 x 10^{-10} mbar, 23 min	(1×1)	
	P	XPS measurements for 4 hours	(1×1)	
	Q	annealing 923 K, 2 x 10^{-7} mbar O_2, 23 min	(1×1)	
	R	annealing 900 K, 2 x 10^{-7} mbar O_2, 15 min	(1×1)	measuring beam damage
	S	annealing 923 K, 2 x 10^{-7} mbar O_2, 15 min	(1×1)	
	T	annealing 923 K, 2 x 10^{-7} mbar O_2, 15 min	(1×1)	

Table S2. Structural parameters of the trial structures employed as starting point in the I/V-LEED calculations. Interlayer distances in Å

	Single Metal					Double Metal	
	Bulk	Czekaj	Kresse	Czekaj V=O - O	Kröger	Bulk	Czekaj
V=O	-	-	-	-	-	-	-
V-V	-	-	-	-	-	0.36	0.52
O_3(1)-V	0.98	0.68	0.35	0.82	0.68	0.98	0.58
V-O_3(1)	0.98	0.98	1.12	0.93	0.93	0.98	1.09
V-V	0.36	0.27	0.22	0.34	0.35	0.36	0.18
V-V	-	-	-	-	-	-	-
O_3(2)-V	0.98	0.96	1.13	0.96	1.02	0.98	0.98
V-O_3(2)	0.98	0.98	1.02	0.98	0.98	0.98	0.98
V-V	0.36	0.36	0.38	0.36	0.36	0.36	0.36
O_3(3)-V	0.98	0.98	1.01	0.98	0.98	0.98	0.98
V-O_3(3)	0.98	0.98	0.98	0.98	0.98	0.98	0.98
V-V	0.36	0.36	0.36	0.36	0.36	0.36	0.36
O_3(4)-V	0.98	0.98	0.98	0.98	0.98	0.98	0.98
	Vanadyl					reconstructed O_3	
	Bulk SM + O	Czekaj	Kresse	Czekaj SM + O	Kröger	Kresse	Window
V=O	1.61	1.59	1.61	1.61	1.55	-	-
V-V	-	-	-	-	-	-	-
O_3(1)-V	0.98	0.82	0.75	0.68	0.69	-	-
V-O_3(1)	0.98	0.93	0.99	0.97	1.05	0.86	0.91
V-V	0.36	0.34	0.28	0.27	0.34	0.19	0.18
V-V	-	-	-	-	-	0.19	0.18
O_3(2)-V	0.98	0.96	1.08	0.96	0.95	0.99	0.98
V-O_3(2)	0.98	0.98	0.99	0.98	0.98	1.44	1.27
V-V	0.36	0.36	0.41	0.36	0.36	-	-
O_3(3)-V	0.98	0.98	1.00	0.98	0.98	1.06	0.98
V-O_3(3)	0.98	0.98	0.98	0.98	0.98	0.98	1.07
V-V	0.36	0.36	0.36	0.36	0.36	0.36	0.36
O_3(4)-V	0.98	0.98	0.98	0.98	0.98	0.98	0.98

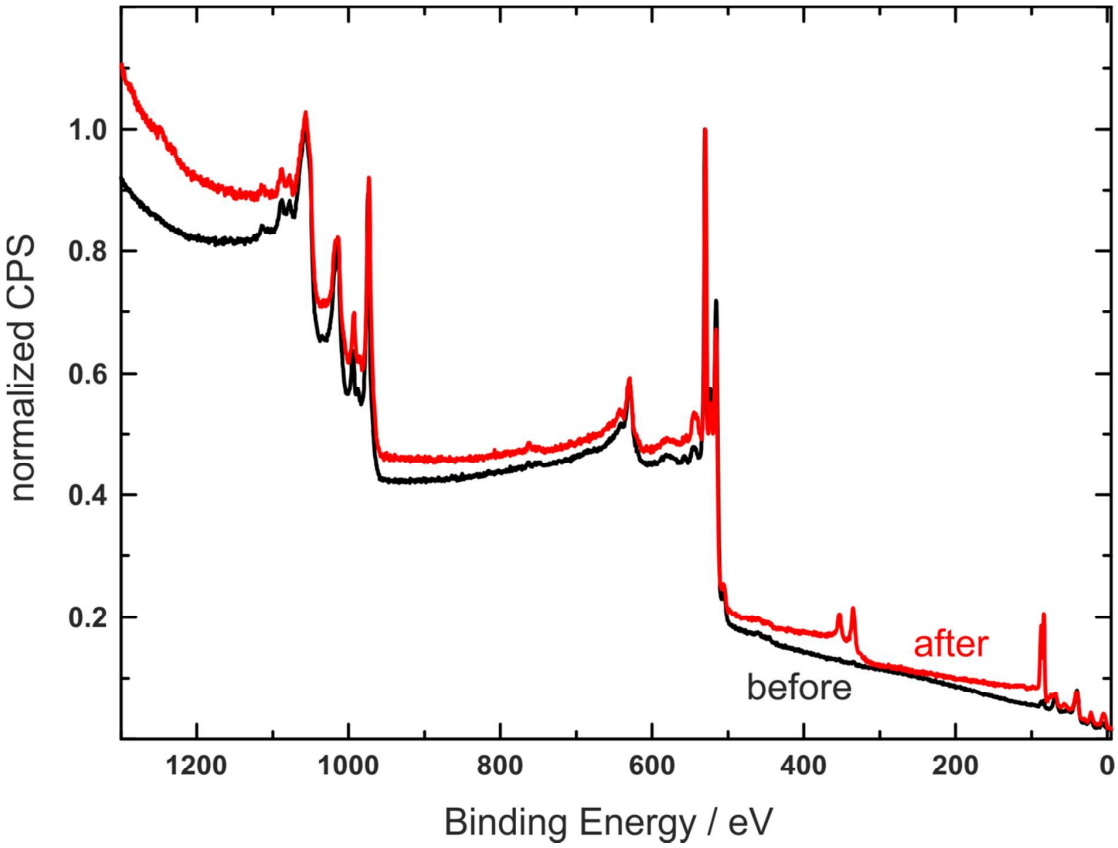

Figure S1. XPS spectra of film #1 after the steps A (labelled *before*) and D (labelled *after*) showing an increase in the intensities of Au peaks (e.g. Au 4f at 91 eV BE). The spectra are normalized to the O 1s peak at 530 eV BE.

Table S3. Structural parameters for the best fit structures resulting from the corresponding start structures in Table S2 with the experimental I/V-data for film #4O with the corresponding Pendry R-factors. All interlayer distances are given in Å

	Single Metal					Double Metal	
	Bulk	Czekaj	Kresse	Czekaj V=O - O	Kröger	Bulk	Czekaj
V=O	-	-	-	-	-	-	-
V-V	-	-	-	-	-	0.96	0.43
O_3(1)-V	0.96	0.59	0.56	0.74	0.59	0.94	1.21
V-O_3(1)	0.91	0.95	0.96	0.97	0.94	0.94	0.70
V-V	0.29	0.57	0.24	0.86	0.58	0.21	0.21
V-V	-	-	-	-	-	-	-
O_3(2)-V	1.10	0.77	1.09	0.45	0.76	1.16	1.85
V-O_3(2)	0.96	0.96	0.99	0.99	0.96	1.23	0.33
V-V	0.36	0.41	0.39	0.40	0.42	0.10	0.36
O_3(3)-V	0.98	1.19	1.02	1.02	1.20	0.98	1.07
V-O_3(3)	0.98	0.74	0.94	0.96	0.73	0.96	0.89
V-V	0.37	0.43	0.41	0.42	0.44	0.43	0.13
O_3(4)-V	0.92	0.92	0.94	0.92	0.91	0.92	1.24
R_{pendry}	**0.23**	**0.28**	**0.24**	**0.33**	**0.30**	**0.33**	**0.41**

Table S3. continued

	Vanadyl					reconstructed O_3	
	Bulk SM + O	Czekaj	Kresse	Czekaj SM + O	Kröger	Kresse	Window
V=O	1.75	1.45	1.99	1.86	1.50	-	-
V-V	-	-	-	-	-	-	-
O_3(1)-V	1.04	0.62	0.61	0.67	0.68	-	-
V-O_3(1)	0.89	0.97	0.96	0.92	0.92	0.93	0.96
V-V	0.58	0.26	0.26	0.86	0.59	0.01	0.27
V-V	-	-	-	-	-	0.28	0.02
O_3(2)-V	0.80	1.08	1.05	0.50	0.77	1.09	1.18
V-O_3(2)	0.92	0.99	1.00	1.25	0.95	1.35	1.28
V-V	0.40	0.39	0.38	0.40	0.40	-	-
O_3(3)-V	1.11	1.01	1.00	0.74	1.02	0.97	1.03
V-O_3(3)	0.85	0.94	0.95	0.97	0.90	0.96	0.88
V-V	0.37	0.39	0.39	0.34	0.39	0.29	0.49
O_3(4)-V	0.93	0.95	0.95	0.94	0.95	1.08	0.88
R_{pendry}	**0.31**	**0.12**	**0.13**	**0.33**	**0.27**	**0.36**	**0.39**

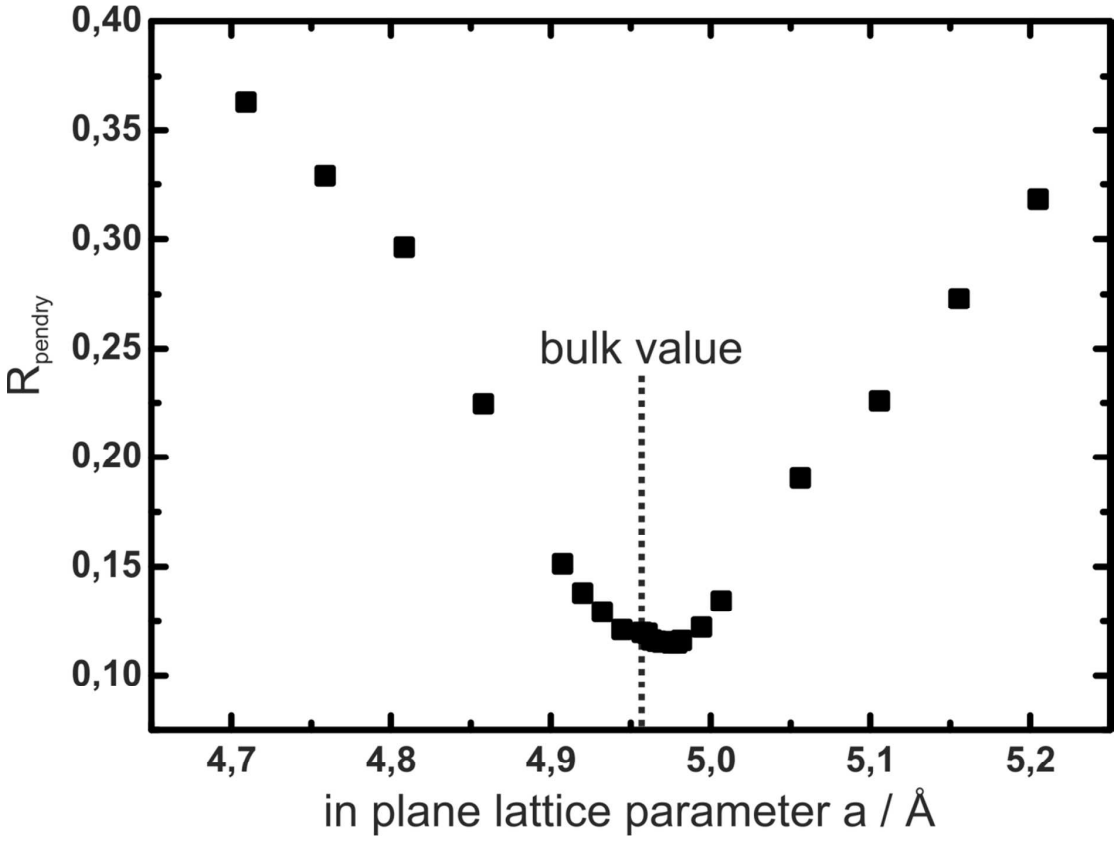

Figure S2. Dependence of R_{pendry} on the in plane lattice constant a; experimental data used: #4O

Table S4. Comparison of interlayer distances of the best fit V=O structure for film #4O, resulting from the I/V-LEED calculations, with the bulk single metal termination parameters. Distances given in Å. Lattice constant of the optimized structure a = 4.9756 Å

	bulk SM	optimized VO	difference	% difference
V=O	-	1.46	-	-
O_3(1)-V	0.98	0.61	-0.37	-38 %
V-O_3(1)	0.98	0.98	0	0
V-V	0.36	0.26	-0.1	-28 %
O_3(2)-V	0.98	1.06	+0.08	+8 %
V-O_3(2)	0.98	1.00	+0.02	+2 %
V-V	0.36	0.39	+0.03	+8 %
O_3(3)-V	0.98	0.99	+0.01	+1 %
V-O_3(3)	0.98	0.95	-0.03	-3 %
V-V	0.36	0.39	+0.03	+8 %
O_3(4)-V	0.98	0.95	-0.03	-3 %

As the previous two publications show, the $V_2O_3(0001)$ surface is indeed terminated by vanadyl groups. So the idea that electron bombardment removes vanadyl oxygen atoms, put forth in the catalytic studies performed on $V_2O_3(0001)$ in our group [58–60,62,63,65], seems reasonable. STM images also clearly show changes in the surface structure after LEED (see Figure 6 C) in Publication 2: *Surface Structure of $V_2O_3(0001)$: A Combined I/V-LEED and STM Study*) and XPS measurements (see Figure 21).

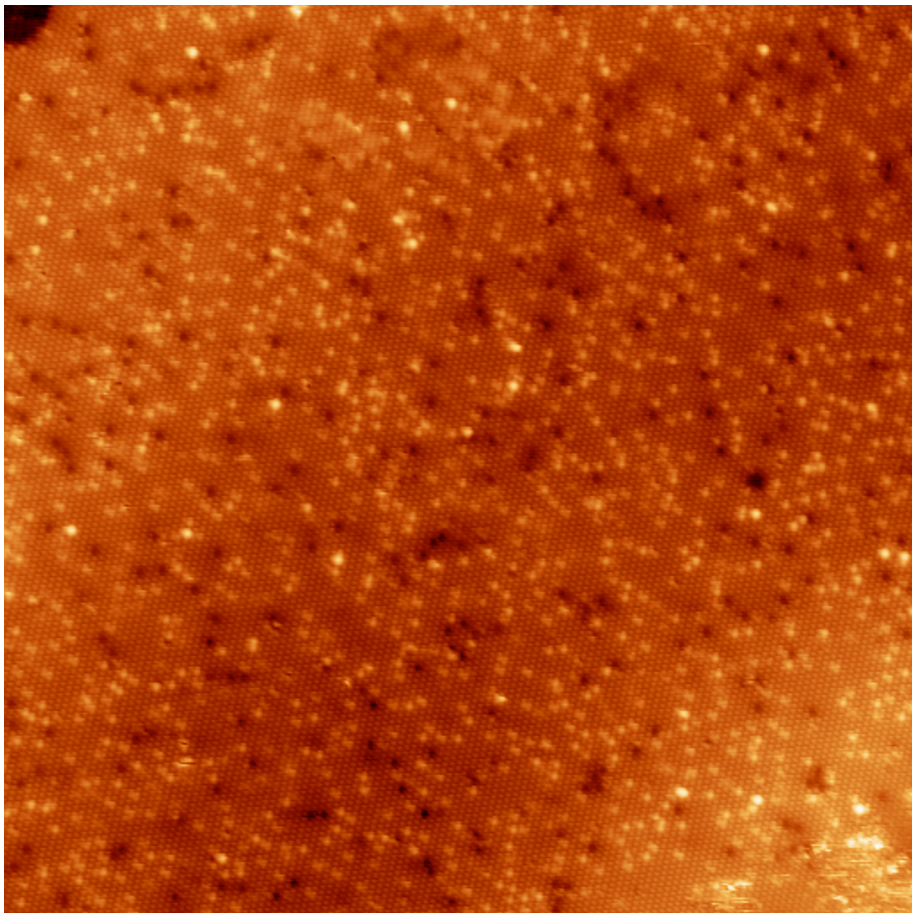

Figure 21: 70 nm by 70 nm STM image of the $V_2O_3(0001)$ surface after over one hour of XPS measurements

These initial changes resulting from exposure of the $V_2O_3(0001)$ surface to electrons produce trimeric structures in the STM pictures. In order to investigate if the surface reduced by larger electron doses corresponds to a single metal termination, which would result from removal of all vanadyl oxygen atoms, the following quantitative structure determination of $V_2O_3(0001)$ surfaces reduced by electron bombardment was performed.

PCCP

PAPER

View Article Online
View Journal | View Issue

Cite this: *Phys. Chem. Chem. Phys.*, 2016, **18**, 3124

Reducing the $V_2O_3(0001)$ surface through electron bombardment – a quantitative structure determination with *I*/*V*-LEED†

Felix E. Feiten, Helmut Kuhlenbeck* and Hans-Joachim Freund

Received 30th November 2015,
Accepted 22nd December 2015

DOI: 10.1039/c5cp07390a

www.rsc.org/pccp

The (0001) surface of vanadium sesquioxide, V_2O_3, is terminated by vanadyl groups under standard ultra high vacuum preparation conditions. Reduction with electrons results in a chemically highly active surface with a well-defined LEED pattern indicating a high degree of order. In this work we report the first quantitative structure determination of a reduced $V_2O_3(0001)$ surface. We identify two distinct surface phases by STM, one well ordered and one less well ordered. *I*/*V*-LEED shows the ordered phase to be terminated by a single vanadium atom per surface unit cell on a quasi-hexagonal oxygen layer with three atoms per two-dimensional unit cell. Furthermore we compare the method of surface reduction *via* electron bombardment with the deposition of V onto a vanadyl terminated film. The latter procedure was previously proposed to result in a structure with three surface vanadium atoms in the 2D unit cell and we confirm this with simulated STM images.

1 Introduction

The surface structure determines the catalytic activity of heterogeneous catalysts. It is thus indispensable to determine the surface structure of heterogeneous catalysts to develop mechanistic models for catalytic reactions and to systematically improve catalyst materials. Real catalysts are often in powder form and can be studied with techniques such as high resolution transition electron microscopy which can provide detailed information on the catalysts's atomic structure. However, many powerful surface characterization techniques cannot be applied to powder samples. For example, diffraction experiments such as LEED require long range order, while scanning probe microscopy can only be applied to very flat surfaces, precluding industrial powder catalysts from being studied with these methods. Model catalysts reduce the structural complexity and enable application of various characterization techniques. Epitaxially grown thin films of metal oxides on metal or metal oxide single crystals expose extended crystal faces which can be studied in detail. Such surfaces also exist at the faces of micro- or nanoparticles employed in industrial catalysis. Vanadium oxides are widely employed in industrial scale heterogeneous catalysis involving oxygen transfer reactions such as sulfuric acid production and the oxidation of butane to maleic anhydride.[1] V_2O_5 is the thermodynamically stable vanadium oxide under ambient conditions and is usually employed in industrial catalytic applications.[2–5] However under catalytic conditions it is reduced and the active species has a vanadium oxidation state smaller than five.[2] There has been an extended discussion about the surface termination of $V_2O_3(0001)$ films prepared under typical UHV conditions,[6–18] which show catalytic activity in a number of oxidation reactions.[19–24] Recently, we have shown that this surface is terminated by vanadyl groups[25,26] as they are also present on $V_2O_5(001)$ surfaces, however, in tetrahedral and not in pyramidal pentagonal configuration.

The vanadyl oxygen atoms at the $V_2O_3(0001)$ surface can be removed through electron bombardment.[6,13] While the V=O covered surface is unreactive towards a variety of gases, the surface reduced by electron bombardment interacts strongly with a number of molecules and also shows catalytic activity.[19–21] In particular the oxidation of methanol to formaldehyde on this reduced surface has been studied in detail,[22–24] and it was shown that oxygen vacancies in V=O groups are relevant for the reaction. The dominating type of defects under typical UHV preparation conditions are missing vanadyl groups,[27] instead of just missing vanadyl oxygen atoms, and these defects have been shown to not catalyze methanol oxidation.[24]

Despite the number of catalytic studies of the reduced $V_2O_3(0001)$ surface[19–24] there has been no experimental quantitative structure determination of this surface. In this paper we combine *I*/*V*-LEED measurements with STM to determine

Fritz Haber Institute of the Max Planck Society, Faradayweg 4-6, 14195 Berlin, Germany. E-mail: kuhlenbeck@fhi-berlin.mpg.de; Fax: +49 30 8413 3155; Tel: +49 30 8413 4222

† Electronic supplementary information (ESI) available. See DOI: 10.1039/c5cp07390a

the surface structure of the $V_2O_3(0001)$ surface reduced by electron bombardment. This structure is different from the one previously proposed for the $V_2O_3(0001)$ surface reduced by deposition of additional vanadium.[10] We compare the two reduced surfaces obtained by the different approaches and discuss differences and the reasons for these differences. We present STM simulations based on density functional theory (DFT) calculations which confirm the previously proposed structure for the surface reduced by vanadium deposition.

2 Experimental

The experiments have been performed in an Omicron UHV chamber equipped with STM, MCP LEED and other methods. The background pressure of the system was less than 5×10^{-11} mbar and especially before and during reduction experiments a pressure in the 10^{-11} mbar range was maintained to avoid rapid contamination of the reactive reduced surface. V_2O_3 films were grown on an Au(111) single crystal, purchased from MaTeck, Germany, by physical vapor deposition of vanadium in an oxygen atmosphere. The films were ordered *via* multiple annealing steps in oxygen or UHV and the ratio of spot-intensity over background in the LEED patterns was used as a measure to optimize the surface quality prior to the reduction experiments. The Au(111) sample was cleaned by Ar^+ bombardment and annealing. Electron bombardment for surface reduction was carried out with a W-filament placed approximately 1 cm in front of the sample. During reduction the sample temperature was kept below 400 K. For more details of the experimental setup see ref. 26. *I*/*V*-LEED measurements were performed with a stepwidth of 1 eV from 50 eV to 500 eV. Normal incidence of the electron beam to the sample, which is assumed in the *I*/*V*-LEED calculations, was achieved with a Helmholtz coil and confirmed by checking the similarity of *I*/*V*-curves of symmetry equivalent diffraction spots. *I*/*V*-LEED calculations were performed with a modified version of the SATLEED code by A. Barbieri and M. A. van Hove (http://www.icts.hkbu.edu.hk/vanhove). The relativistic phase shifts used in the calculations have been computed for bulk V_2O_3 with the phase shift package supplied with SATLEED. Two different search algorithms were employed to optimize the structure with respect to the Pendry *R*-factor. Initially differential evolution[28] (DE) was used with a maximum angular momentum (LMAX) of 7 and 2 eV step width while the final optimization steps were carried out using CMA-ES with the SHARK library,[29] LMAX = 9 and 1 eV steps. This was done because DE is better at finding the global minimum when the start structure is significantly different to the structure corresponding to the global minimum in R_{Pendry}. CMA-ES on the other hand converges faster when the optimization is started close to the global minimum. Four different types of structural models with one, two or three vanadium atoms or one vanadyl (V═O) group in the surface unit cell were investigated. The number of optimized atomic coordinates and Debye temperatures depends on the model (16 coordinates and four Debye temperatures for the model with one vanadium atom at the surface, 17 coordinates and five Debye temperatures for the models with two vanadium atoms or one vanadyl group at the surface and 18 coordinates and five Debye temperatures for the model with three metal atoms). Additional optimization parameters were in all cases the real and imaginary parts of the inner potential. For each of the metal terminations around 30 different start structures, varying in the interlayer distances, were used as start structures in independent *I*/*V*-LEED optimization runs.

STM simulations were performed with the FHI-aims program package.[30] Electronic structure calculations have been performed with the functional by Perdew and Wang (PW91)[31] using a $10 \times 10 \times 1$ Monkhorst–Pack *k*-grid and tight basis functions as described in ref. 30. We used symmetric slabs generated from the structural data discussed in the Results and discussion section. The surface structure down to the first vanadium layer below the fourth oxygen layer was repeated in reverse order below. This means, the *z*-distances along the surface normal were mirrored while the order, in which the vanadium atoms occupy the sites was kept. In this way slabs of roughly 20 Å thickness were generated. The self-consistent field cycle for the electronic structure calculations was repeated until the total energies of two subsequent runs were different by less than 1×10^{-6} eV. STM images were produced from the electronic structure using the procedure by Tersoff and Hamann.[32] Addition of more basis functions or expanding the *k*-grid to $12 \times 12 \times 1$ did not lead to a noticeable change in the resulting STM pictures. Visualization of the images was done with Visual Molecular Dynamics (VMD).[33]

3 Results and discussion

A number of reduced $V_2O_3(0001)$ surfaces, *i.e.* with a lower oxygen content than the vanadyl terminated surface obtained under standard preparation conditions in UHV, can be envisaged. Two different metal terminated surfaces can be obtained by cutting the bulk V_2O_3 unit cell parallel to the (0001) plane: a surface terminated by one V atom atop a distorted hexagonal O_3 layer, henceforth called single metal (SM) termination, and a surface with two V atoms in the surface unit cell, which we call double metal (DM) termination. DFT calculations by Kresse *et al.* have suggested a surface termination with three V atoms in the surface unit cell, *i.e.* a triple metal (TM) termination.[11] This TM termination was also found experimentally when depositing additional V ontop of a vanadyl terminated surface.[10] These structural models are shown in Fig. 1 together with the vanadyl terminated model structure. Furthermore, in the DFT study mentioned above as well as in another DFT study, reduced surface phases with partial vanadyl coverage were predicted, in which vanadium atoms occupy the sites of missing V═O groups.[11,18]

A vanadyl terminated film was reduced in five steps with *I*/*V*-LEED measurements performed before the reduction procedure and after each reduction step. The *I*/*V*-curves corresponding to the (1 0) diffraction spot are plotted in Fig. 2, with the

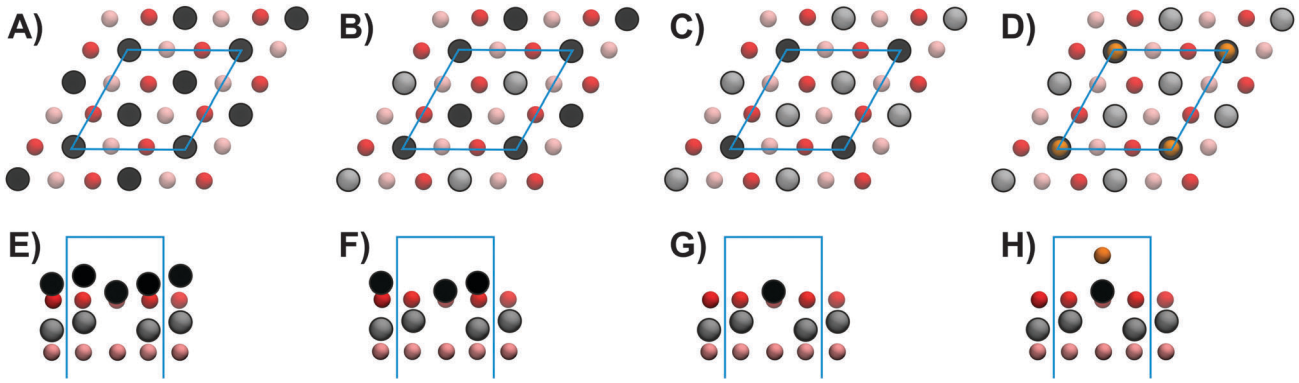

Fig. 1 Structural models of the TM structure (A + E), the DM structure (B + F), the SM structure (C + G) and the V═O terminated structure (D + H). Images (A) through (D) show top views of the respective surfaces while images (E) through (H) show sideviews visualizing the stacking sequence. Color-coding: surface V – black, bulk V – grey, surface O – red, bulk O – pink, vanadyl O – orange; unit cells indicated in blue.

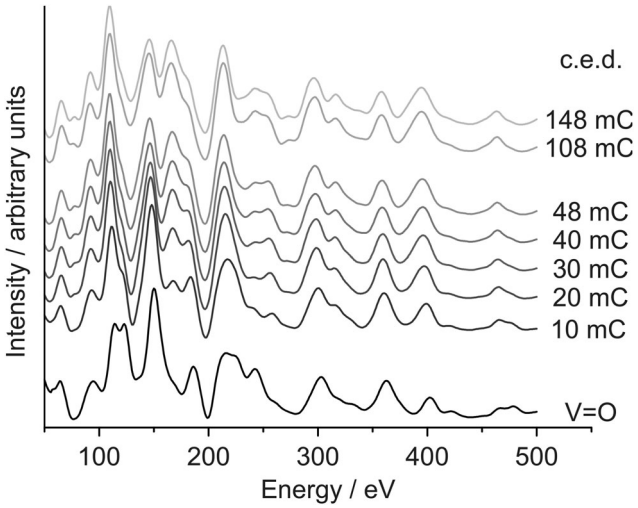

Fig. 2 *I*/*V*-LEED curves showing the stepwise reduction of the V_2O_3(0001) surface. The cumulative electron dose is indicated next to the curves.

cumulative electron dose (c.e.d.) irradiated onto the sample prior to the measurement indicated next to the curves.

I/*V*-LEED calculations for the vanadyl terminated sample (curve labelled V═O) yield a Pendry *R*-factor of 0.09. The sample was then irradiated in five steps with electron doses (E_{kin} = 500 eV) of 10 mC per step (8 mC for the last reduction step). There is a significant change of the *I*/*V*-curve after the first electron dose. For example out of the two peaks at 125 eV that have similar intensities for the V═O terminated surface one shows increased intensity while the other one is reduced to a shoulder after the initial reduction step. Changes in the *I*/*V*-curves are discernible up to a c.e.d. of 40 mC while the curves measured after the last reduction step, corresponding to a c.e.d. of 48 mC, are practically identical to those measured after a c.e.d. of 40 mC. This might be interpreted as a sign of finished reduction, insofar as further electron bombardment does not seem to change the surface structure. Additional reduction experiments on vanadyl terminated V_2O_3(0001) films with doses of 108 mC (E_{kin} = 50 eV) and 145 mC (E_{kin} = 500 eV), both applied in a single dose, also generated *I*/*V*-curves very similar to those obtained after the last two steps of the stepwise reduction (top two curves in Fig. 2).

Table 1 Best-fit Pendry *R*-factors for the fully reduced surface. The two numbers given for the DM termination relate to different settings for the optimization of the Debye temperature of the second surface vanadium atom. Details are given in the text

Surface termination	R_{Pendry}
Triple metal	0.32
Double metal	0.18/0.22
Single metal	0.19
Vanadyl	0.19

I/*V*-LEED calculations gave the best-fit Pendry *R*-factors listed in Table 1 after structural optimization (the dataset obtained after 40 mC cumulative electron dose in the stepwise reduction was used in the *I*/*V*-LEED evaluation). The variation ranges for the Debye temperatures in the *I*/*V*-LEED optimization runs were limited to 550–600 K and to 600–650 K for bulk vanadium and oxygen, respectively. These ranges correspond to the bulk Debye temperatures determined for vanadyl terminated V_2O_3(0001) previously.[26] Without restriction unphysically low bulk Debye temperatures were obtained while the respective Pendry *R*-factors are on average 0.01 smaller than with restriction to physically sensible values. The triple metal termination gives an *R*-factor of 0.32, significantly worse than the results for the other three models, and it is thus unlikely, that this model is the right one. The other three surface terminations yield very similar *R*-factors of 0.19 for the single metal, 0.18 for the double metal and 0.19 for a vanadyl termination model. While the Debye temperature for the vanadium atom ontop of the top oxygen trilayer is around 200 K for all three of those models, the Debye temperature for the second vanadium atom in the DM termination is just 102 K (the lower limit set in the optimization procedure was 100 K). This might be an indication that the DM model does not correspond to the actual surface structure as an artificially low Debye temperature corresponds to strong vibration of this atom, reducing its influence on the *I*/*V*-curves. Furthermore two independent optimizations for DM model

structures resulted in almost identical parameters and *R*-factors (0.184 and 0.187 respectively) but significantly different V–V interlayer distances of 0.68 Å and 0.96 Å between the two surface vanadium atoms. This is also attributed to the limited influence of this atom onto the *I*/*V* data. Limiting the Debye temperature for all atoms to a minimum of 200 K leads to an *R*-factor of 0.22 for the DM model.

The relatively low *R*-factor of the vanadyl terminated structural model could indicate that reduced and V=O terminated areas coexist on the surface. In order to check this, *I*/*V*-LEED calculations with modified experimental data were performed. In these curves certain percentages of V=O coverage were simulated *via* subtraction of *I*/*V*-curves of a vanadyl terminated surface from the experimental data measured for the reduced surface. Partial vanadyl coverages of 10%, 20%, 30%, 40% and 50% were simulated for all three metal terminations. The result was in all cases an increase of *R*-Pendry with increasing V=O admixture, rendering the existence of V=O covered areas unlikely. This is in agreement with the fact that additional electron bombardment does not change the *I*/*V*-LEED curves noticeably which indicates that essentially all vanadyl groups have been reduced. Vibrational spectroscopy of the fully reduced surface also indicates that all vanadyl groups are reduced, as the V=O stretch mode at 127 meV disappears completely.[22]

The STM image of the reduced $V_2O_3(0001)$ surface shown in Fig. 3 reveals the coexistence of two different types of surface termination. The flat areas exhibit round features with a spacing identical to that of the vanadyl terminated surface but with a much lower corrugation of around 0.4 Å. The rougher areas have a corrugation of around 1.2 Å. In some areas the features appear to be somewhat ordered with a structure resembling a $(\sqrt{3} \times \sqrt{3})R30°$ supercell relative to the (1×1) vanadyl termination. The corresponding unit cells are indicated in Fig. 3 with closed (flat area) or broken (rough area) lines. It should be noted that LEED images do not show any visible reflexes of a $(\sqrt{3} \times \sqrt{3})R30°$ supercell indicating that the areas with this structure are too small to produce clearly visible LEED intensity maxima. Consequently in the remaining discussion the focus is on the structure of the flat areas.

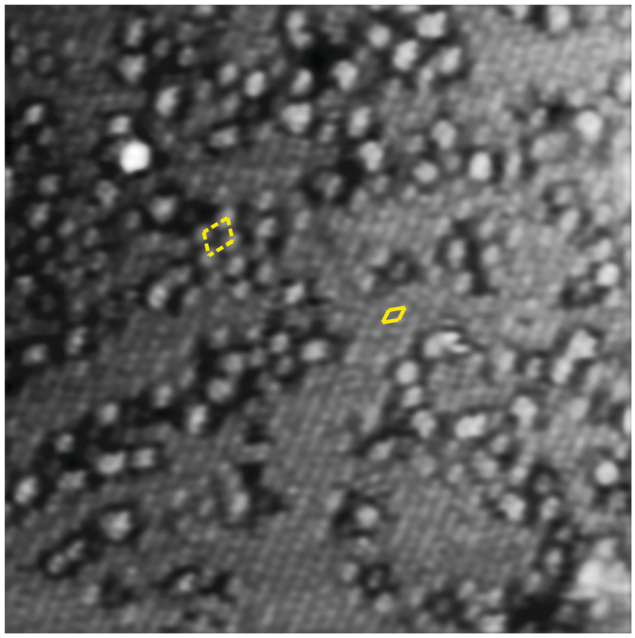

Fig. 3 20 nm × 20 nm STM image of the reduced $V_2O_3(0001)$ surface (145 mC c.e.d.), +1 V, +0.1 nA. The apparent unit meshes are indicated by rhombi drawn with full (flat surface) and broken (rough surface) lines. The image has been FFT-filtered. See the ESI† for the raw image and Fourier transforms.

The triple metal termination can be excluded as the correct structural model for the flat surface areas based on the significantly worse *R*-factor compared to the other three terminations. The double metal termination is rejected based on the very low Debye temperature for the second surface vanadium atom calculated in the *I*/*V*-LEED optimizations and the fact that limiting this Debye temperature to a minimum value of 200 K results in a significantly worse *R*-factor. The vanadyl termination can be counted out based on vibrational spectroscopy, the lack of change in the *I*/*V*-curves after 40 mC cumulative electron dose and the low corrugation in the STM images. We thus conclude that the reduced surface is terminated by a single layer of vanadium atoms atop a distorted hexagonal oxygen trilayer. This termination can be produced from the vanadyl terminated surface simply by removal of the vanadyl oxygen atoms. The rough areas visible in STM might be the result of oxygen atoms removed from the underlying oxygen trilayer by electron bombardment. Previous STM studies of a surface reduced with a smaller electron dose show a smaller amount of disordered surface area indicating that this disordered phase grows with prolonged electron irradiation.[22]

Table 2 lists the interlayer distances in the best-fit SM structure together with the interlayer distances obtained in DFT calculations and the respective changes relative to the corresponding distances in the bulk structure. The distance between the top vanadium atom and the topmost oxygen trilayer is contracted by 45% in the best-fit SM structure. DFT calculations also predict a significant contraction of 64% (GGA) or 55% (HSE). The distance between the topmost O3 layer and the underlying vanadium is changed relatively little in the

Table 2 Interlayer distances in the best-fit SM structure resulting from the *I*/*V*-LEED optimizations in comparison with DFT-results published in references[25] and[11] together with the respective change Δ relative to the bulk interlayer distances

	I/*V*-LEED	Δ (%)	GGA[11]	Δ (%)	HSE[25]	Δ (%)
V_{top}–O	0.54	−45	0.35	−64	0.44	−55
O–V	0.92	−6	1.12	+14	1.00	+2
V–V	0.20	−44	0.22	−39	0.27	−25
V–O	1.15	+17	1.13	+15	1.05	+7
O–V	1.07	+9	1.02	+4	0.91	−7
V–V	0.30	−17	0.38	+6	0.50	+39
V–O	1.07	+9	1.01	+3	0.91	−7
O–V	0.91	−7	0.98	—	0.91	−7
V–V	0.39	+8	(0.36)	—	0.46	+28
V–O	0.95	−3	(0.98)	—	0.91	−7

I/*V*-LEED calculations (5% contraction) while GGA and HSE calculations predict an expansion of 14% and 2% respectively. The V–V distance in the following vanadium double layer is reduced by 44% in good agreement with reductions of 39% and 25% in the DFT studies. The distance to the next oxygen trilayer is increased by 17% with respect to the bulk value (15% and 7% respective increases result from the DFT calculations). For the lower lying layers the interlayer distances resulting from the *I*/*V*-LEED calculations show some deviations from the DFT calculations. Overall the changes of the interlayer distances relative to the bulk values become smaller with increasing distance from the surface and the agreement between experiment and theory is good. The trend for expansion or contraction of the interlayer distances for the five layers closest to the surface is very similar to that for the vanadyl terminated surface,[26] the magnitude of the changes however is larger for the reduced surface. Graphs showing all experimental *I*/*V*-curves for the unreduced surface and the reduced surface after 40 mC c.e.d. as well as the calculated beams for the best-fit structures for a vanadyl terminated model (unreduced surface) and a single metal termination (reduced surface) can be found in the ESI.†

The parameters (V═O model structure) determined for the vanadyl terminated surface match those published previously[26] very well. For the case of the reduced surface we have shown that it is terminated by a vanadium layer with a single atom in the 2D surface unit cell. However, different from the case of the vanadyl terminated surface, in this case three structural models (SM, DM, and V═O) gave very similar *R*-factors so that additional arguments were required to identify the real termination. The reason for this result is likely the limited quality of the fit using the SM model in combination with the higher number of fit parameters for the V═O and the DM models. The VO structure and the DM structure both have one atom more than the SM structure. This corresponds to two additional fit parameters: one interlayer distance and one additional Debye temperature. The optimization algorithm adapts these parameters such that, together with small changes of the other parameters, a good fit results also for the DM and the V═O model, which would not be the case if the fit was better for the correct model. With increasing quality of the fit for the correct structure model the differences between the *R*-factors obtained for this model and for other models get larger as shown previously for very well ordered V═O covered surfaces.[26] For these surfaces the *R*-factor for the vanadyl terminated model is rather small (≈ 0.1) and the difference in *R*-factor between a vanadyl terminated model structure and a single or double metal termination is significant (roughly 0.1 difference in R_{Pendry} for the SM model and 0.2 for the DM model). A solution to the issue of similar *R*-factors for different structural models would be to increase the total energy range of the LEED data since the fit will get worse with increasing energy range for a wrong model. Unfortunately, increasing the energy range was technically not possible in our experiments.

We now turn to the comparison of two different methods of reducing the $V_2O_3(0001)$ surface. In contrast to our method of reduction through electron bombardment the vanadyl terminated surface can also be reduced by depositing additional vanadium as done by Schoiswohl and coworkers.[10] The deposition of additional vanadium leads to coexisting surface structures with one of the two different types of surface-structure having a similarly low corrugation as the flat areas in the STM image of the $V_2O_3(0001)$ surface reduced by electron bombardment shown in this work. However, high resolution STM images of this flat area show that the spacing between the protrusions corresponds to $1/\sqrt{3}$ that of the regular vanadyl terminated surface lattice parameter. It was concluded that the surface prepared by vanadium deposition onto the vanadyl terminated surface contains three metal atoms per surface unit cell. This is also indicated by the attenuation of the (1 0) type spots in LEED and the simultaneous increase in the intensity of diffraction spots corresponding to the $(1/\sqrt{3} \times 1/\sqrt{3})R30^\circ$ unit cell. There is no such systematic attenuation of the (1 0) type spots when reducing the $V_2O_3(0001)$ surface by electron bombardment.

Schoiswohl *et al.* have reported that the surface reduced by deposition of additional vanadium can be ordered by flash-annealing the film to 700 K.[10] More specifically the flat areas, attributed to a metal termination, grow at the expense of the rougher surface areas. For the surface reduced by electron bombardment this procedure leads to a significant decrease of order as seen in LEED images (not shown here). Prolonged annealing in UHV leads to restoring of the vanadyl terminated surface for the surface reduced by vanadium deposition as well as for the surface reduced by electron bombardment. This is in agreement with DFT studies which predict the metal terminated surfaces to be thermodynamically unfavored even at the lowest pressures achievable in UHV systems.[11,25]

STM images have been computed for the four different models using the approach by Tersoff and Hamann[32] applied to electronic structures calculated with DFT as described in the experimental part. The pictures shown in Fig. 4 have been calculated for the structural parameters resulting from the *I*/*V*-LEED calculations corresponding to the *R*-factors in Table 1 for SM, DM and VO models. For the 3M termination model structural data from DFT calculations by Kresse *et al.*[11] were used instead since the *I*/*V*-LEED calculations only give very bad agreement between experiment and theory. Each image shows nine unit cells. First of all it should be noted, that at imaging conditions comparable to our STM measurements (+1 V, 0.1 nA) and previous STM measurements[13,22] (−1 V/+2 V and 0.2 nA), all four structural models give a single round protrusion per unit cell. The simulated STM images thus do not contribute to the identification of the $V_2O_3(0001)$ surface reduced by electron bombardment in this study. The images shown in Fig. 4 have been computed for a voltage of +0.1 V and relatively high isovalues (the isovalue is proportional to the tunneling current). This means that the virtual STM tip is very close to the surface. These simulation conditions match the experimental conditions in STM measurements on the $V_2O_3(0001)$ surface reduced by vanadium deposition.[10] At these conditions the three metal terminations result in distinctly different STM images. The triple metal termination shown in

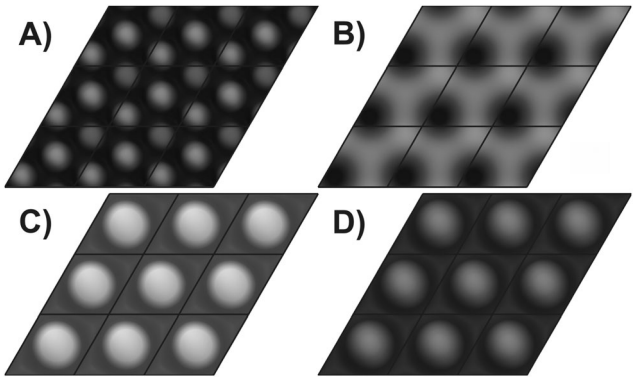

Fig. 4 Simulated STM images for (A) TM, (B) DM, (C) SM and (D) V═O structures; bias +0.1 V; each image shows nine unit cells.

Fig. 4A shows three round protrusions per unit cell. This is in agreement with the experimental images observed by Schoiswohl *et al.* and corroborates their conclusion that the $V_2O_3(0001)$ surface reduced by vanadium deposition is terminated by three vanadium atoms in the surface unit cell. The double metal termination [Fig. 4B] shows two features in the surface unit cell, one slightly more intense than the other, corresponding to the height difference between these two vanadium atoms. The single metal termination [Fig. 4C] shows just a single round protrusion per surface unit cell. In each of the three metal termination simulations the protrusions show up at the positions of the surface vanadium atoms. Finally, the simulation of the vanadyl terminated structure [Fig. 4D][9] also shows one round protrusion per unit cell, as observed experimentally for non-reduced $V_2O_3(0001)$ films.[10,25,26] Previous STM simulations by others also showed one round protrusion per surface unit cell for the V═O termination[18,34] while they did not consider any of the metal terminations.

4 Conclusions

We have shown that reducing the $V_2O_3(0001)$ surface through electron bombardment leads to a coexistence of two surface structures: a badly ordered and an ordered phase. While currently only speculations can be made as to the nature of the badly ordered phase, we have quantitatively determined the structure of the ordered phase. It is terminated by a single vanadium atom in the surface unit cell, similar to the V═O terminated surface with the vanadyl oxygen atoms removed. The interlayer relaxations in the structure with the reduced surface are even larger than in the corresponding vanadyl terminated structure according to *I*/*V*-LEED.

The mediocre R_{Pendry} of 0.18 for this structure is most likely related to the overall limited quality of the surface with significant amounts of disordered areas. The relatively low Pendry *R*-factors of 0.18 for the double metal termination and 0.19 for the vanadyl termination show how the optimization algorithms can fit even an incorrect model to the experimental data with the help of additional free parameters. Increasing the Debye temperature for the topmost vanadium atom in the double metal termination leads to an increase of R_{Pendry} to 0.22.

We have shown that the structure of the reduced $V_2O_3(0001)$ surface depends on the preparation method. The surface reduced by deposition of additional vanadium is terminated by three rather than one metal atoms in the surface unit cell. Our simulated STM images confirm the match of the STM images obtained by Schoiswohl *et al.* with the triple metal structure calculated by Kresse *et al.* by DFT.[10,11]

Both of the different reduced surfaces are only kinetically stabilized and revert to the vanadyl terminated surface upon annealing by oxygen diffusion from the bulk to the surface. This is in agreement with density functional theory predicting the thermodynamic instability of the reduced surfaces even at the lowest pressures achievable in UHV experiments.[11,25]

Acknowledgements

The authors thank Sergey Levchenko for help in setting up the FHI-aims software and for help in performing DFT calculations and STM simulations and Georg Kresse for providing structural data for the triple metal termination. This work was funded by the Deutsche Forschungsgemeinschaft (DFG) within the collaborative research center 546, ''Transition Metal Oxide Aggregates''. We gratefully acknowledge the Fonds der Chemischen Industrie for financial support. Modified versions of the SATLEED code by Barbieri/Van Hove were used in the *I*/*V*-LEED calculations.

References

1 B. M. Weckhuysen and D. E. Keller, *Catal. Today*, 2003, **78**, 25–46.
2 G. L. Simard, J. F. Steger, R. J. Arnott and L. A. Siegel, *Ind. Eng. Chem.*, 1955, **47**, 1424–1430.
3 S. Kasaoka, E. Sasaoka and H. Iwasaki, *Bull. Chem. Soc. Jpn.*, 1989, **62**, 1226–1232.
4 G. C. Bond and S. F. Tahir, *Appl. Catal.*, 1991, **71**, 1–31.
5 G. Deo and I. E. Wachs, *J. Catal.*, 1993, **146**, 323–334.
6 A.-C. Dupuis, M. Abu Haija, B. Richter, H. Kuhlenbeck and H.-J. Freund, *Surf. Sci.*, 2003, **539**, 99–112.
7 I. Czekaj, M. Witko and K. Hermann, *Surf. Sci.*, 2003, **525**, 46–56.
8 I. Czekaj, K. Hermann and M. Witko, *Surf. Sci.*, 2003, **525**, 33–45.
9 H. Niehus, R.-P. Blum and D. Ahlbehrendt, *Surf. Rev. Lett.*, 2003, **10**, 353–359.
10 J. Schoiswohl, M. Sock, S. Surnev, M. Ramsey, F. Netzer, G. Kresse and J. Andersen, *Surf. Sci.*, 2004, **555**, 101–117.
11 G. Kresse, S. Surnev, J. Schoiswohl and F. P. Netzer, *Surf. Sci.*, 2004, **555**, 118–134.
12 T. K. Todorova, M. V. Ganduglia-Pirovano and J. Sauer, *J. Phys. Chem. B*, 2005, **109**, 23523–23531.
13 S. Guimond, M. Abu Haija, S. Kaya, J. Lu, J. Weissenrieder, S. Shaikhutdinov, H. Kuhlenbeck, H.-J. Freund, J. Döbler and J. Sauer, *Top. Catal.*, 2006, **38**, 117–125.

14 E. A. Kröger, D. I. Sayago, F. Allegretti, M. J. Knight, M. Polcik, W. Unterberger, T. J. Lerotholi, K. A. Hogan, C. L. A. Lamont and D. P. Woodruff, *Surf. Sci.*, 2007, **601**, 3350–3360.
15 C. Kolczewski, K. Hermann, S. Guimond, H. Kuhlenbeck and H.-J. Freund, *Surf. Sci.*, 2007, **601**, 5394–5402.
16 J. Seifert, E. Meyer, H. Winter and H. Kuhlenbeck, *Surf. Sci.*, 2012, **606**, L41–L44.
17 A. J. Window, A. Hentz, D. C. Sheppard, G. S. Parkinson, H. Niehus, D. Ahlbehrendt, T. C. Q. Noakes, P. Bailey and D. P. Woodruff, *Phys. Rev. Lett.*, 2011, **107**, 016105.
18 A. Window, A. Hentz, D. Sheppard, G. Parkinson, D. Woodruff, W. Unterberger, T. Noakes, P. Bailey, M. Ganduglia-Pirovano and J. Sauer, *Surf. Sci.*, 2012, **606**, 1716–1727.
19 M. Abu Haija, S. Guimond, Y. Romanyshyn, A. Uhl, H. Kuhlenbeck, T. Todorova, M. V. Ganduglia-Pirovano, J. Döbler, J. Sauer and H.-J. Freund, *Surf. Sci.*, 2006, **600**, 1497–1503.
20 M. Abu Haija, S. Guimond, A. Uhl, H. Kuhlenbeck and H.-J. Freund, *Surf. Sci.*, 2006, **600**, 1040–1047.
21 A. Bandara, M. Abu Haija, F. Höbel, H. Kuhlenbeck, G. Rupprechter and H.-J. Freund, *Top. Catal.*, 2007, **46**, 223–230.
22 Y. Romanyshyn, S. Guimond, H. Kuhlenbeck, S. Kaya, R. P. Blum, H. Niehus, S. Shaikhutdinov, V. Simic-Milosevic, N. Nilius, H.-J. Freund, M. V. Ganduglia-Pirovano, R. Fortrie, J. Döbler and J. Sauer, *Top. Catal.*, 2008, **50**, 106–115.
23 D. Göbke, Y. Romanyshyn, S. Guimond, J. M. Sturm, H. Kuhlenbeck, J. Döbler, U. Reinhardt, M. V. Ganduglia-Pirovano, J. Sauer and H.-J. Freund, *Angew. Chem., Int. Ed.*, 2009, **48**, 3695–3698.
24 Y. Romanyshyn, S. Guimond, D. Göbke, J. M. Sturm, H. Kuhlenbeck, J. Döbler, M. V. Ganduglia-Pirovano, J. Sauer and H.-J. Freund, *Top. Catal.*, 2011, **54**, 669–684.
25 F. E. Feiten, J. Seifert, J. Paier, H. Kuhlenbeck, H. Winter, J. Sauer and H.-J. Freund, *Phys. Rev. Lett.*, 2015, **114**, 216101.
26 F. E. Feiten, H. Kuhlenbeck and H.-J. Freund, *J. Phys. Chem. C*, 2015, **119**, 22961–22969.
27 N. Nilius, V. Brázdová, M.-V. Ganduglia-Pirovano, V. Simic-Milosevic, J. Sauer and H.-F. Freund, *New J. Phys.*, 2009, **11**, 093007.
28 V. B. Nascimento and E. W. Plummer, *Mater. Charact.*, 2015, **100**, 143–151.
29 C. Igel, V. Heidrich-Meisner and T. Glasmachers, *J. Mach. Learn. Res.*, 2008, **9**, 993–996.
30 V. Blum, R. Gehrke, F. Hanke, P. Havu, V. Havu, X. Ren, K. Reuter and M. Scheffler, *Comput. Phys. Commun.*, 2009, **180**, 2175–2196.
31 J. P. Perdew, J. A. Chevary, S. H. Vosko, K. A. Jackson, M. R. Pederson, D. J. Singh and C. Fiolhais, *Phys. Rev. B: Condens. Matter Mater. Phys.*, 1992, **46**, 6671–6687.
32 J. Tersoff and D. R. Hamann, *Phys. Rev. B: Condens. Matter Mater. Phys.*, 1985, **31**, 805–813.
33 W. Humphrey, A. Dalke and K. Schulten, *J. Mol. Graphics*, 1996, **14**, 33–38.
34 S. Surnev, G. Kresse, M. Sock, M. G. Ramsey and F. P. Netzer, *Surf. Sci.*, 2001, **495**, 91–106.

Electronic Supplementary Material (ESI) for Physical Chemistry Chemical Physics.

Supporting Information for „Reducing the V_2O_3(0001) Surface through Electron Bombardment – A Quantitative Structure Determination with I/V-LEED"

Felix E. Feiten, Helmut Kuhlenbeck, Hans-Joachim Freund
Fritz Haber Institute of the Max Planck Society,
Faradayweg 4-6, 14195 Berlin, Germany

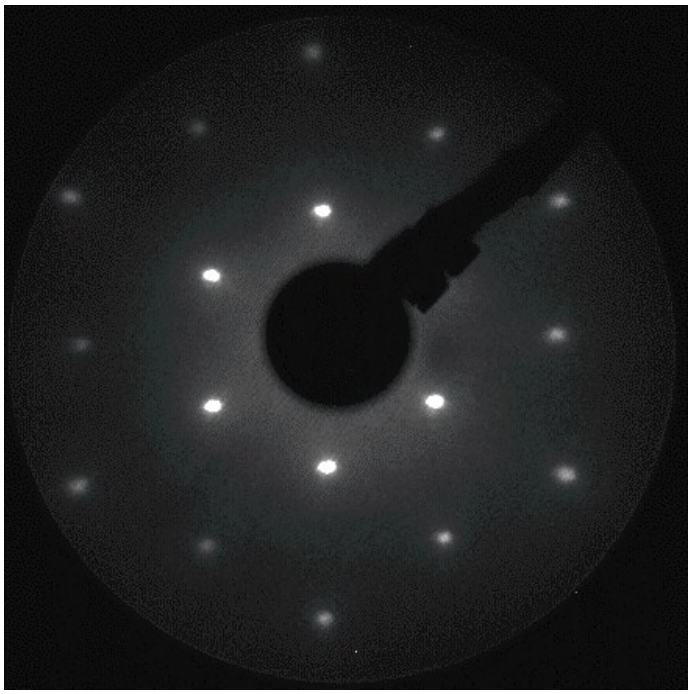

Figure S1. LEED pattern of the reduced V_2O_3(0001) surface taken at an electron kinetic energy of 150 eV. The image contrast and brightness have been digitally modified to make sure that all spots are clearly visible.

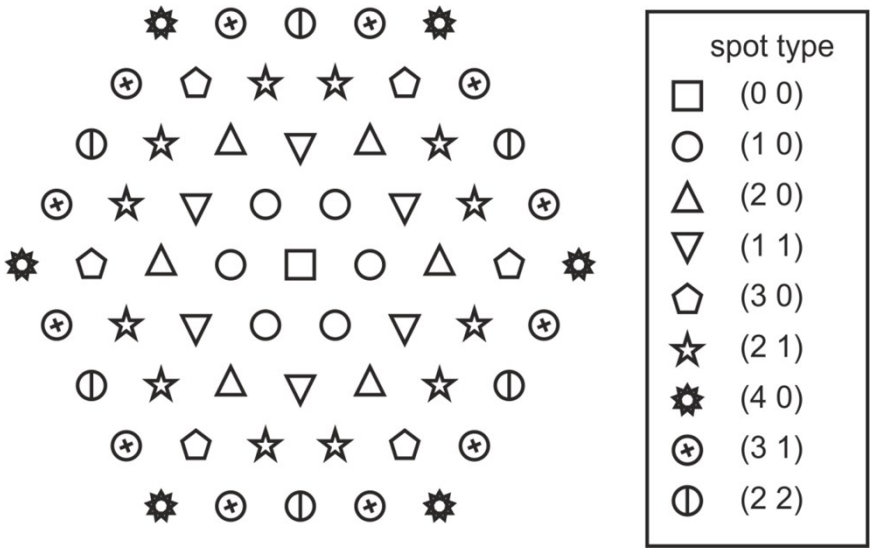

Figure S2. LEED pattern of V_2O_3(0001) showing the effective symmetry. For details regarding the symmetry see reference 7 in the paper

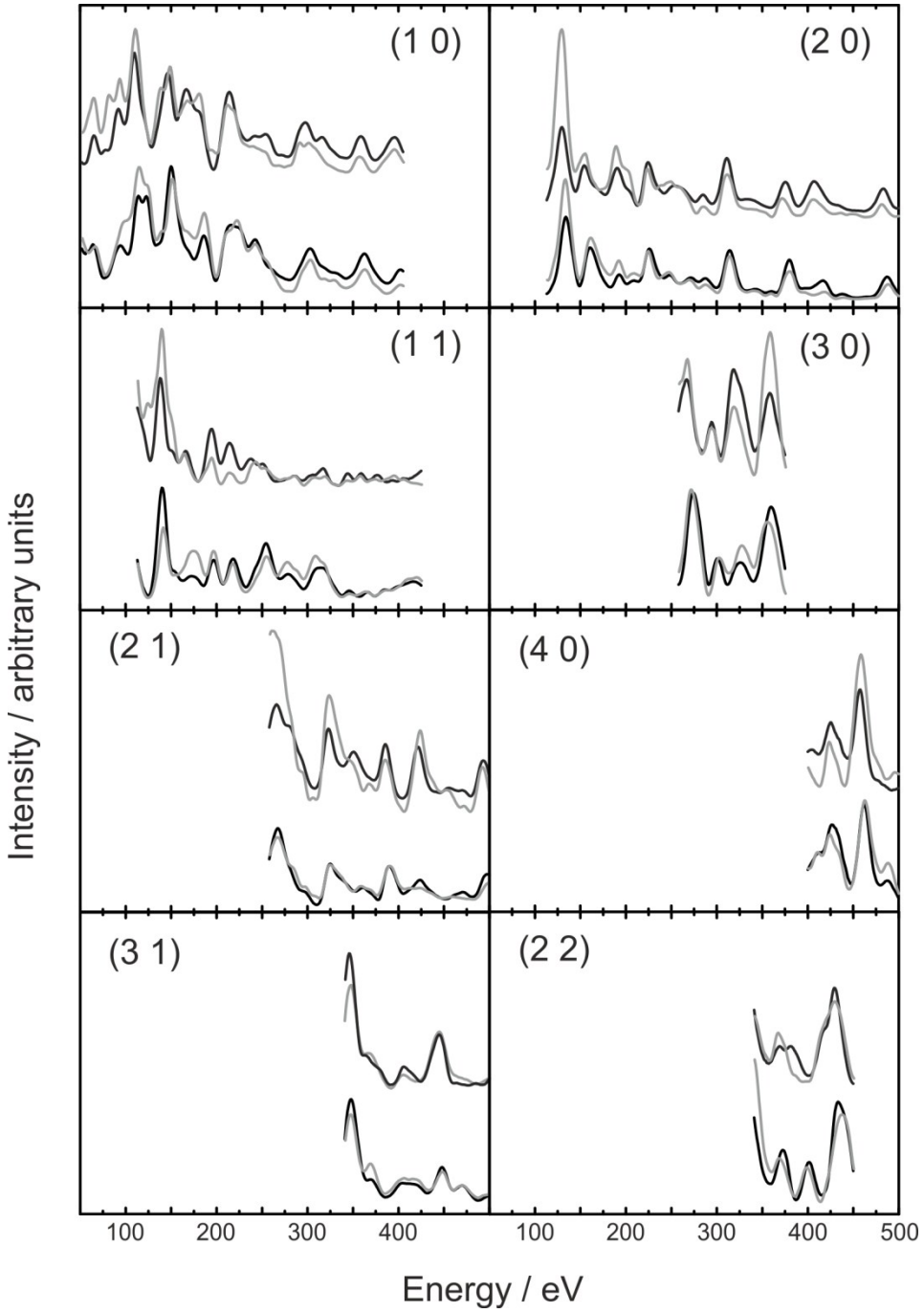

Figure S3. I/V-LEED curves for the vanadyl covered surface (bottom two curves in each graph) and the reduced surface (top two curves in each graph, cumulative electron dose 40 mC). The respective experimental data are shown in black and the calculated beams for the best-fit structure in grey. The structural model for the reduced surface is the single metal termination as described in the paper.

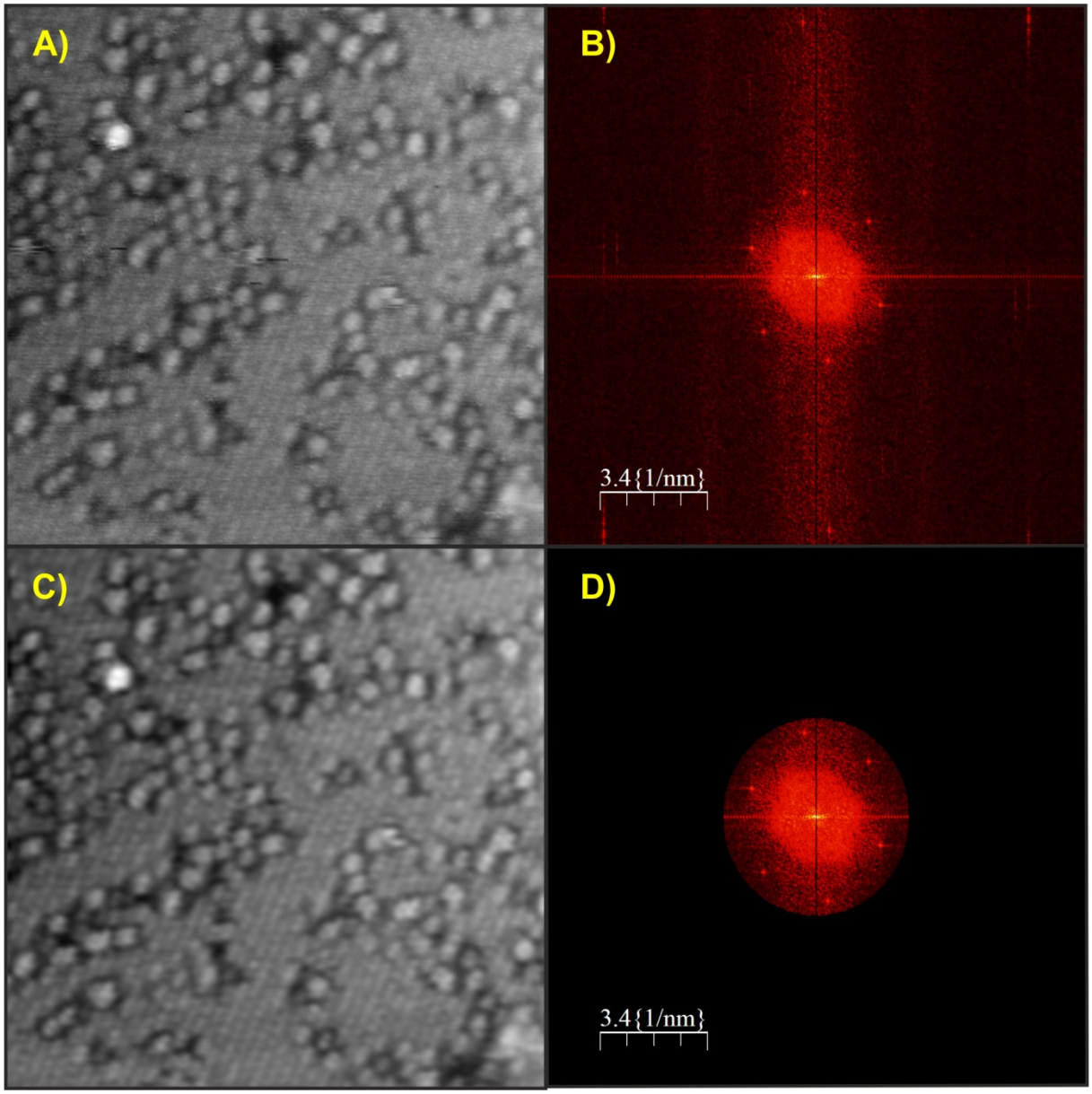

Figure S4. Raw STM image of the reduced surface (A) with the corresponding fourier transform (B) and the fourier filtered STM image (C) with the fourier transform (D).

Chapter 4

Comprehensive Interpretation, Review and Discussion

In this chapter references to figures in all three publications will be made.The following abbreviations will be used for the respective publications: **P1** for Publication 1: *Surface Structure of* $V_2O_3(0001)$ *Revisited*, **P2** for Publication 2: *Surface Structure of* $V_2O_3(0001)$*: A Combined I/V-LEED and STM Study* and **P3** for Publication 3: *Reducing the* $V_2O_3(0001)$ *Surface through Electron Bombardment - A Quantitative Structure Determination with I/V-LEED*

4.1 The Vanadyl Terminated Surface

Phase Space

The experimentally observed phases, as indicated by their LEED patterns, are shown in **P1** Figure 2. The films deposited at oxygen pressures between 1×10^{-7} mbar and 1×10^{-6} mbar and temperatures between 525 K and 750 K show a hexagonal LEED pattern referred to as (1×1) in the following. Oxidation of these films, i.e. heating to temperatures of 673 K to 873 K in oxygen pressures of 5×10^{-6} mbar to 2×10^{-5} mbar, creates additional reflexes in the LEED images. These preparations are termed $\sqrt{3}$ because of the corresponding $\left(\sqrt{3} \times \sqrt{3}\right)$ R30° supercell. Films with a $\sqrt{3}$ structure can also be obtained directly after vanadium deposition, when the oxygen pressure during deposition is 2×10^{-6} mbar. Further oxidation of structures with a $\left(\sqrt{3} \times \sqrt{3}\right)$ R30° supercell, at oxygen pressures of roughly 5×10^{-5} mbar and temperatures of 773 K to 873 K, leads to formation and evaporation of V_2O_5. This sequence of oxidation steps is visualized in

P2 Figure 2.

Comparing this behaviour of the V_2O_3 films upon oxidation with theoretical phase diagrams is helpful to identify the structure of the (1×1) phase. The theoretical phase diagram by Kresse et al. [91], depicted in Figure 3 in Chapter 1.3, shows that vanadyl groups are expected to be removed from the vanadyl terminated surface when increasing the oxygen pressure. This leads to the $\sqrt{3}$ structure with 1/3 or 2/3 of vanadyl groups missing. Increasing the oxygen pressure further should lead to the formation of an O3 terminated surface. The same sequence of surface structures at varying oxygen pressures is found in the theoretical phase diagram published by Window et al. [46] based on computations by Todorova et al. [92,100] Neither of the two phase diagrams makes predictions for surface structures with a higher oxygen content than in an O3 termination.

Thus, the oxidation of films with a (1×1) LEED pattern to films showing a $\left(\sqrt{3} \times \sqrt{3}\right)$ R30° LEED pattern is only compatible with the theoretical phase diagrams if the (1×1) structure represents a vanadyl terminated surface. If however, the structure that shows a (1×1) LEED pattern was terminated by an O3 layer, the oxidation of this structure to a surface with a $\left(\sqrt{3} \times \sqrt{3}\right)$ R30° LEED pattern would have to be explained by introducing completely new surface structures.

Two issues arise when comparing the theoretical phase diagrams with the experimentally observed phases. First, neither of the theoretical phase diagrams predicts a fully vanadyl terminated surface to be thermodynamically favored at any oxygen pressure. Second, the absolute values of the oxygen pressure under typical preparation conditions seem to favor the O3 termination over the vanadyl termination. Both issues are related to the same underlying cause: The relatively simple functional employed (PW91), based on the generalized gradient approximation, does not describe the vanadium-oxygen bond strength accurately. Instead, the bonding of oxygen to vanadium is overestimated and thus phases with a higher oxygen content are predicted to be too stable. This issue was partially resolved by the application of a hybrid functional (HSE) by Paier and Sauer within **P1**. The introduction of Fock exchange into the calculations leads to a more accurate description of vanadium-oxygen binding energetics. This is shown through comparison of calculated heats of formation, calculated for a number of vanadium oxide species with the HSE as well as the PBE functional (PBE is a functional similar to PW91 using the generalized gradient approximation), with experimental values. The DFT calculations

of the surface phase diagram for $V_2O_3(0001)$ with the HSE functional predict that the vanadyl termination should be thermodynamically favored over a much larger range of oxygen pressures compared to previous DFT studies. This is visualized in **P1** Figure 6. The $\sqrt{3}$ structure was not considered in these DFT calculations and taking it into account would likely reduced the stability regime of the vanadyl termination. However, it should be kept in mind, that these calculations are always based on repeating, symmetric structures (for reasons of computational cost). It is very likely, that there is a range of oxygen pressures where a statistically distributed number of missing V=O groups is thermodynamically most stable. This would then directly correspond to the experimental finding that it is hard to prepare a surface with very few defects and the common observation of statistically distributed missing V=O groups. **P1** Figure 6. also shows the thermodynamically favored bulk phases at the varying oxygen potentials. At oxygen potentials high enough to favor an O3 surface termination the stable bulk phase is calculated to be V_2O_5. This agrees with the experimental observation, that oxidation of $\sqrt{3}$ structures leads to the formation and evaporation of V_2O_5 instead of producing O3 terminated V_2O_3 films. The theoretical description of $V_2O_3(0001)$ is still not complete as all density functional theory calculations up to now, including the ones using the hybrid HSE functional, have issues correctly describing magnetism and electronic behaviour of V_2O_3. While V_2O_3 is non-magnetic and conducting at room temperature, relaxation of spins in calculations leads to a magnetic insulator. On the other hand, structural parameters of V_2O_3 are described rather well by both GGA-based as well as hybrid functionals as the comparison with experimental values in **P2** Table 5 and the accompanying text shows.

Film History

The overall oxygen content of the whole film is not easily determined. While annealing the $\sqrt{3}$ structure in UHV will lead to reduction to a V=O terminated surface, the degree of surface oxidation, as evidenced by trimeric features or missing V=O groups in STM images, can only be determined by performing STM measurements which are relatively time consuming. A time-saving method to judge the overall surface quality, i.e. ordering and amount of local defects, is evaluating the ratio of spot intensity over background intensity in LEED images. For example, after preparation of a $V_2O_3(0001)$ film, LEED

images are taken and the signal/background ratio is calculated for a given diffraction spot. The sample is then annealed in UHV. If the signal/background ratio increases this suggests that the sample was slightly oxidized before this annealing step. If however the signal/background ratio decreases after annealing in UHV this indicates that the sample surface was or is slightly reduced. Optimizing the signal/background ratio by repeated annealing steps in UHV or oxygen allows for quicker optimization of the film surface compared to performance of STM measurements after each preparation step which can be very time consuming.

STM

P1 Figure 4 shows two STM images of the (1×1) structure. They both display a honeycomb lattice with round features. This matches STM simulations for a vanadyl terminated surface. [46, 73] For an O3 termination STM simulations predict triangular features instead. [46,73] The dark depressions in **P1** Figure 4 (b) correspond to missing V=O groups and are thus indicative of a (slightly) oxidized surface. The bright protrusions in **P1** Figure 4 (a) that appear as trimers, i.e. constituted of three round protrusions, are a sign of surface reduction. They appear in STM images taken after I/V-LEED measurements [**P1** Figure 4 (a) and **P2** Figure 6 C)] or, in higher number, after XPS experiments [Figure 21 and **P2** Figures 3 A) and 6 B)]. As shown in the series of images in **P2** Figure 3 A) to C) oxidation of a film with trimers leads to removal of the trimers and removal of V=O groups. While this stepwise oxidation can be seen in the STM images, the I/V-curves of these three preparations look very similar, as the defects are randomly distributed. Therefore, STM measurements are needed to get detailed information about the type and number of randomly distributed defects.
The honeycomb lattice with round features was found in all STM images recorded throughout this work. No STM images showing coexistence of two or more different surface terminations were obtained.

I/V-LEED

I/V-LEED measurements and calculations to determine the surface structure of the

(1×1) termination were performed on several preparations. In order to assess the type and density of local defects, I/V-LEED measurements were always performed in direct succession with STM measurements. The STM pictures shown in **P1** Figure 4 (a) and **P2** Figure 6 C) were taken directly after the corresponding I/V-LEED measurements, while the STM images in **P2** Figure 6 A) and B) were taken immediately prior to the respective I/V-LEED measurements. The size of the dataset obtained experimentally and used in the calculations, based on the electron energy range, varies as described below. For all I/V-LEED calculations 14 different initial trial structures were used: Five single metal, five vanadyl, two double metal and two reconstructed O3 structures. These were taken from the literature. [46, 71, 80, 81, 91] Different trial structures of the same structural model, e.g. different vanadyl structures, have different interlayer distances. The trial structures were then optimized with respect to the Pendry R-factor as described in Section 2.2 through variation of 15-17 atomic coordinates and three to five Debye temperatures as well as the real and imaginary parts of the inner potential. The double metal terminations always yielded R-factors bigger than 0.3 and will thus not be discussed in the following. Models with a vanadyl termination give the best R-factor for all preparations with a (1×1) LEED pattern. **P2** Table 3 gives an overview over the best-fit R-factors for vanadyl, single metal and O3 termination models for three different preparations with the corresponding STM images depicted in **P2** Figure 6. The R-factor for the vanadyl terminated structure is always close to 0.1 and does not vary significantly with the size of the dataset. The R-factor for a single metal termination is always worse than for vanadyl termination with values of 0.20 for a total energy range (ΔE) of 766 eV, 0.14 for an energy range of 1128 eV and 0.23 for 1819 eV. The relatively low R_{Pendry} of 0.14 matches the significant number of trimeric structures in the STM image **P2** Figure 6 B). This preparation had been investigated with XPS prior to STM and I/V-LEED measurements and the photoelectrons from the XPS measurement might have induced some surface reduction. For all other preparations XPS measurements were carried out after the combined STM and I/V-LEED measurements. The Pendry R-factors for reconstructed O3 terminated structures are always worse than those for vanadyl or single metal terminated structures. Interestingly, the R-factors for the O3 terminated structures also show a dependence on the size of the dataset used: $R_{Pendry}(O_3)$ =0.23 (ΔE =766 eV), $R_{Pendry}(O_3)$ =0.26 (ΔE =1128 eV) and $R_{Pendry}(O_3)$ =0.36 (ΔE =1819 eV). The agree-

ment between experiment and theory for an O3 terminated structural model becomes worse with increasing dataset size. In addition to the fact that the vanadyl terminated surface structure is clearly favored by the lower R-factors, this is another indication that the (1×1) surface is not terminated by an oxygen trilayer. An incorrect model can be fitted to experimental data but this fit will become worse with increasing dataset size. This is precisely the case for the fit between O3 terminated model structures and the experimental data for (1×1) terminated surfaces.

The R factor of 0.10 for vanadyl terminated structural models is very strong proof that the (1×1) structure is indeed terminated by vanadyl groups. All other structural models including the O3 structure give significantly worse fits. This result is in strong contrast to the studies by Window et al. [45, 46] that favor an O3 terminated structural model.

Debye Temperatures

In the course of the I/V-LEED calculations the vibrational amplitudes of vanadium and oxygen atoms, represented by their Debye temperatures Θ_D, were also determined. Depending on the structure investigated three to five independent Debye temperatures were used. One Debye temperature was assigned to oxygen atoms in the topmost O3 layer and one to all lower lying vanadium and oxygen atoms respectively, which will henceforth be referred to as bulk vanadium and oxygen Debye temperatures. Additionally, individual Debye temperatures were assigned to the surface vanadium atom(s) in single metal and double metal terminations, the vanadium atom in the vanadyl group of vanadyl terminated surfaces and the oxygen atom in the vanadyl group of vanadyl terminated surfaces. Just as the structural coordinates, these were treated as fit parameters in the I/V-LEED optimization procedure. The Debye temperatures for the best fit of vanadyl terminated structural models to three I/V-LEED measurements are shown in **P2** Table 2. The average values are $\Theta_D(\text{vanadyl O}) = 310\,\text{K}$, $\Theta_D(\text{vanadyl V}) = 339\,\text{K}$, $\Theta_D(\text{top O3 layer O}) = 447\,\text{K}$, $\Theta_D(\text{bulk V}) = 570\,\text{K}$ and $\Theta_D(\text{bulk O}) = 624\,\text{K}$. The average of the bulk vanadium and oxygen Debye temperatures is 597 K and matches the bulk Debye temperature of V_2O_3 (580 K) reported in the literature [119] reasonably well. This is an indication that this method of determining Debye temperatures is accurate.

Ion Scattering

The fast atom diffraction (FAD) experiments performed by Jan Seifert and reported in **P1** constitute the fourth ion scattering investigation of $V_2O_3(0001)$ films reported in the last years. [45–47] Simulated curves for a vanadyl terminated structure match the experimental curves recorded on $V_2O_3(0001)$ very well while the agreement between experimental curves and curves simulated for an O3 termination is bad. This is in contrast to an ion beam triangulation (IBT) study on $V_2O_3(0001)$ by Seifert et al. that favored an O3 terminated structural model. [47] However, IBT does not always image the topmost surface layer. Seifert et al. reported that the IBT curves of a Cu(110) surface covered with alanine molecules are essentially identical to the curves measured on a clean Cu(110) surface. [125] Thus the alanine surface layer is not seen in IBT. This allows the FAD and IBT experiments by Seifert et al. to be reconciled. The ion beam triangulation experiment might actually have imaged the O3 layer below the surface vanadyl groups.

The NICISS study reported by Window et al. was performed on $V_2O_3(0001)$ films prepared on Cu_3Au. [45] The Cu_3Au sample was pretreated with oxygen and vanadium oxide films with a thickness of $\sim 25\,\text{Å}$ were deposited onto a Cu-O surface layer. Comparison of experimental and calculated curves for the NICISS experiment clearly favors an O3 surface structure over a vanadyl covered surface. The different substrate (Cu_3Au) and the different preparation procedure (sequential deposition and oxidation of thin vanadium layers with oxygen also diffusing out from the substrate) as well as the much smaller overall film thickness involved in the NICISS experiments could possibly have led to differently terminated, more oxidized $V_2O_3(0001)$ films, compared to our studies on the surface structure of $V_2O_3(0001)$.

Finally the MEIS study by Window et al. is also in favor of an O3 terminated $V_2O_3(0001)$ surface. [45, 46] The MEIS experiments were performed on thick ($\sim 200\,\text{Å}$) $V_2O_3(0001)$ films deposited on Au(111) and thinner ($\sim 20\,\text{Å}$) $V_2O_3(0001)$ films deposited on Pd(111) with very similar resulting curves measured for the different substrates and thicknesses. While the MEIS experiments are not easily refuted, this study seems to be the only reliably comparable ion scattering study of $V_2O_3(0001)$ films definitely in favor of an O3 terminated surface. The vanadyl terminated surface on the other hand is in agreement with a multitude of experiments summarized in Chapter 1.3. Moreover the evidence pre-

sented within this thesis, specifically the combination of real space images obtained by STM with quantitative structure determination through I/V-LEED makes it very clear, that the films prepared in UHV under standard conditions are terminated by a full layer of vanadyl groups with some local defects.

4.2 The Reduced Surface

The structure of the as-deposited surface of $V_2O_3(0001)$ films has been shown to contain one vanadyl group per surface unit mesh in **P1** and **P2**. This surface is rather inert and does not show catalytic activity. [58, 60] The vanadyl terminated $V_2O_3(0001)$ surface can be reduced via electron bombardment [57] or via deposition of additional vanadium [73]. Both modes of reduction lead to surfaces that show catalytic activity. [58–60,62,63,65,75] It has been assumed that electron bombardment of the vanadyl terminated $V_2O_3(0001)$ surface leads to removal of vanadyl oxygen atoms, as also indicated by STM images. [62,63,65] In order to quantitatively determine the surface structure of $V_2O_3(0001)$ surfaces reduced by electron bombardment I/V-LEED measurements in combination with STM were performed. **P3** Figure 2 shows I/V-LEED curves of the (1 0) spot after varying electron doses. The curve at the bottom corresponds to a vanadyl terminated surface prior to electron bombardment. This surface was reduced via electron bombardment in doses of 10 mC (8 mC for the last step) with the cumulative electron dose indicated next to the curves. While the change to the I/V-curve after the first reduction step is pronounced, the changes become increasingly smaller with increasing cumulative electron dose. The curves taken after 40 mC c.e.d. and 48 mC c.e.d. show almost no differences. Two additional I/V-curves, obtained from surfaces reduced by single, longer doses of 108 mC and 148 mC are also very similar. An STM image of the $V_2O_3(0001)$ surface reduced by a 148 mC dose is shown in **P3** Figure 3. In it two coexisting surface phases can be seen: an ordered phase with low corrugation, which has the same unit mesh size as the V=O terminated surface and a disordered phase with much larger corrugation. This disordered phase seems to exhibit a $\left(\sqrt{3} \times \sqrt{3}\right)$ R30° supercell. However, no reflexes corresponding to such a supercell can be seen in the LEED images. Therefore, in the following, the discussion will focus on the flat, well ordered areas. I/V-LEED calculations were performed for the experimental data of the $V_2O_3(0001)$ surface reduced by a cumulative electron dose of 40 mC. The

resulting R-factors are listed in **P3** Table 1. For a triple metal termination the R-factor is 0.32 and this structural model can thus be ruled out. The R-factors for the other three surface termination models are very similar with R = 0.18 for a double metal terminated model, R = 0.19 for a single metal terminated surface structure and R = 0.19 for a vanadyl terminated model structure. In the optimized parameters for the double metal termination the Debye temperature for the topmost vanadium atom has an extremely low Debye temperature of 102 K. This means that this atom would be vibrating very strongly, reducing its influence on the I/V-curves. This might be an indication that the DM termination model is not the correct structure. Increasing this Debye temperature to a more sensible value of 200 K increases the R-factor to 0.22. The double metal termination and the vanadyl termination both contain one more atom than the single metal termination. This presents the fitting algorithm with two additional fit parameters: the z-coordinate of the extra atom as well as its Debye temperature. This factor should become less relevant when using experimental data of a very well ordered surface and this can indeed be seen in **P2** where double metal terminated structural models give much worse fits to the experimental data of the vanadyl terminated films than single metal terminated model structures. The vanadyl terminated model can be excluded as the right structural model due to vibrational spectroscopy of $V_2O_3(0001)$ films reduced via electron bombardment, which shows complete quenching of the V=O stretch mode. [57] Thus it is concluded that the flat, well ordered areas of the surface reduced by electron bombardment are terminated by a single vanadium layer.

To further substantiate this conclusion STM images for four different surface terminations (TM, DM, SM and V=O) were simulated with DFT calculations using the Tersoff-Hamann approach. At measurement conditions similar to those used in the STM measurements reported herein and similar to those used in STM measurements of the $V_2O_3(0001)$ surface reduced by electron bombardment previously [62, 63, 65] no distinction can be made between the four structural models. Each of them results in a single round protrusion per surface unit mesh. At smaller tip distances, i.e. smaller voltages and bigger tunneling currents (represented through the isovalue in the STM simulations), the differently terminated surfaces do show significant differences as visualized in **P3** Figure 4. The triple metal termination exhibits three round features per surface unit mesh, the double metal termination two, and both single metal as well as vanadyl termination show one round

protrusion per surface unit mesh. Schoiswohl et al. have performed STM measurements with similar conditions on $V_2O_3(0001)$ surfaces reduced by deposition of vanadium onto vanadyl terminated films.[73] They observed coexistence of two different surfaces phases, one of which has a low corrugation as expected for a metal terminated surface. Their STM images show three round protrusions per surface unit mesh. Thus, the STM simulations reported in **P3** confirm the conclusion made by Schoiswohl et al. that the flat areas of the surface reduced by vanadium deposition are terminated by three vanadium atoms in the surface unit mesh.

Chapter 5

Conclusions and Outlook

The present thesis shows that the $V_2O_3(0001)$ surface prepared under standard UHV conditions is terminated by a full layer of vanadyl groups with some local defects.
I/V-LEED calculations performed for several different preparations of $V_2O_3(0001)$ films are all in clear favor of a vanadyl terminated surface as demonstrated by Pendry R-factors of ~ 0.1, independent of the energy range of the measurements. I/V-LEED calculations for O3 terminated structural models on the other hand yield significantly worse Pendry R-factors that also increase in magnitude when expanding the dataset. STM images obtained directly before or after the I/V-LEED experiments give no indication of a coexistence of different surface terminations. They show round protrusions, as expected for a vanadyl terminated surface from simulated STM images. On the other hand, $V_2O_3(0001)$ surfaces terminated by an oxygen trilayer are expected to show trigonal features instead, as calculated by DFT. [46, 70]
The as-prepared films can be oxidized to a $\sqrt{3}$-structure which is in agreement with the theoretical phase diagram calculated by Kresse et al. [91] only if the as-prepared films are vanadyl terminated. There have been no indications that the (0001) surface of V_2O_3 can be further oxidized than in an O3 terminated structure, but formation of a bulk oxide with higher oxygen content is possible. Surfaces with a $\sqrt{3}$ structure could not be oxidized to form O3 terminated surfaces, although this might have been expected based on the theoretical phase diagram [91]. Instead formation and evaporation of V_2O_5 occured when exposing the $\sqrt{3}$ structure to higher oxygen pressures.
The results of fast atom diffraction experiments performed by Jan Seifert at the Humboldt University have been reported in Publication 1: *Surface Structure of $V_2O_3(0001)$ Revisited*. The experimental data fit calculated curves for a vanadyl terminated surface well while there are significant deviations between experiment and theory for an O3 ter-

minated surface. The ion beam triangulation study by Seifert et al. [47] was at that time interpreted as evidence of an O3 terminated surface. However, these results do not have to be in conflict with a vanadyl terminated surface. As Seifert et al. have shown [125] ion beam triangulation is not always sensitive to the topmost surface layer and thus the observed experimental curves in [47] might not correspond to an O3 termination but might have instead resulted from the oxygen layer underneath the vanadyl groups.

The DFT calculations performed by Joachim Paier and discussed in Publication 1: *Surface Structure of V_2O_3(0001) Revisited* show that the vanadyl terminated surface is stable over a wider range of oxygen potentials than previous theoretical studies suggested [91,92,100], albeit ignoring phases with a larger two dimensional unit cell such as the $\sqrt{3}$-structures with partial V=O coverage. Including $\sqrt{3}$-structures into the calculations would very likely reduce the maximum oxygen pressure at which a vanadyl terminated surface is thermodynamically favor. The enlargement of the stability regime of the vanadyl terminated phase, relative to previous DFT studies, is due to a more accurate description of the V-O bond strength by calculations employing the hybrid HSE functional as compared to calculations employing the GGA based functionals PW91 and PBE that were used in earlier computational studies. The two latter functionals overestimate the strength of vanadium to oxygen bonding. The DFT calculations with the HSE functional predict V_2O_5 to be the stable bulk vanadium oxide at oxygen pressures where the O3 termination would be thermodynamically favored over other surface terminations of V_2O_3(0001). This substantiates the conclusion that the oxidation of V_2O_3(0001) surfaces with a $\sqrt{3}$ structure leads to formation of V_2O_5 which evaporates at typical preparation conditions.

Debye temperatures for the vanadyl terminated V_2O_3(0001) films were determined by two different methods: temperature dependent measurements of LEED intensities and using the Debye temperatures as fit parameters in the I/V-LEED calculations. While the first method gives only a rough estimate for the surface Debye temperature, the second method allows rather accurate determination of several Debye temperatures for different atomic species within the sample. The obtained Debye temperatures are 310 K for vanadyl oxygen atoms, 340 K for vanadyl vanadium atoms, 447 K for oxygen atoms in the top O3-layer, 570 K for bulk vanadium atoms and 624 K for bulk oxygen atoms. The values for bulk oxygen and vanadium are very close to the reported bulk Debye temperature for V_2O_3 of 580 K [119], indicating the reliability of this method.

The present thesis has also shown that reduction of a vanadyl terminated $V_2O_3(0001)$ film via electron bombardment leads to a single metal termination.

STM images of surfaces reduced by electron bombardment show coexistence of an ordered, flat and a disordered, more corrugated structure. The flat surface has been analyzed by I/V-LEED giving R-factors of 0.19 for a single metal termination and a vanadyl termination, 0.22 for a double metal termination and 0.32 for a triple metal termination. A vanadyl termination can be ruled out for the flat, reduced surface since the corrugation in STM is too low, additional electron bombardment did not change the I/V-curves significantly and vibrational spectroscopy shows complete quenching of the V=O stretch mode at 127 meV. [62] The comparatively small R-factors for V=O and double metal termination are attributed to the limited order of the sample and to the fact that these models both have two more parameters to fit than the single metal terminated model.

The disordered areas of the surface reduced by electron bombardment might indicate that this procedure can reduce the surface beyond a single metal termination, i.e. remove oxygen atoms below the vanadyl groups.

Simulated STM images based on DFT calculations were obtained for triple metal, double metal, single metal and vanadyl terminated structures. At tunneling conditions similar to those used in the STM measurements on the surface reduced by electron bombardment in this thesis as well as in other publications [62, 98] all four structural models produce just one protrusion per surface unit cell in the simulated STM images.

Schoiswohl et al. have reported reduction of vanadyl terminated $V_2O_3(0001)$ surfaces via deposition of additional vanadium. [73] The STM images they have presented show three round protrusions per surface unit cell. Our STM simulations with parameters matching the experiments of Schoiswohl et al. confirm their reasoning that deposition of vanadium onto a V=O terminated surface leads to a triple metal termination. The simulated STM images show three protrusions per surface unit cell for a TM termination, two for a double metal termination and just one protrusion per surface unit cell for single metal and vanadyl terminations.

Both ways to reduce the $V_2O_3(0001)$ surface, electron bombardment and vanadium deposition, lead to surfaces that are not thermodynamically stable. Upon annealing in ultra-high vacuum they are transformed back into vanadyl terminated surfaces. This is

in agreement with DFT calculations by Kresse et al. [91] and by Paier and Sauer within this thesis: single metal and triple metal terminated surface structures are thermodynamically favored only at extremely low oxygen pressures far beyond those achievable in UHV systems.

Several questions remain that might warrant further investigations.

Regarding the $V_2O_3(0001)$ surface reduced via electron bombardment the nature of the disordered phase observed in STM images is still to be determined. However it might be hard to characterize this.

Another issue regarding surface reduction is the appearance of trimeric features in STM images recorded after XPS or I/V-LEED measurements. STM images of surfaces reduced slightly by electron bombardment usually show dark depressions corresponding to missing vanadyl oxygen atoms. [62, 63, 65] These are remarkably different from the trimeric structures. Simulation of STM images for a variety of possible structures that these trimers could represent might be a means to identify their nature.

Finally the mechanism of oxidation from a vanadyl terminated surface to $\sqrt{3}$ structures is still unknown. Schoiswohl et al. have propesed migration of V=O groups to step edges upon oxidation [73] but this would not really be an oxidation as the V=O groups would not be removed but rather just moved and the overall oxygen content of the surface would not be changed by this.

Chapter 6

Appendix

6.1 List of Publications

Publication 1:

Felix E. Feiten, Jan Seifert, Joachim Paier, Helmut Kuhlenbeck, Helmut Winter, Joachim Sauer, and Hans-Joachim Freund, **Surface Structure of** $V_2O_3(0001)$ **Revisited**, *Phys. Rev. Lett.* **114**, 216101, 2015.

http://dx.doi.org/10.1103/PhysRevLett.114.216101

Contribution of Felix E. Feiten:

The I/V-LEED and STM experiments as well as the experimental investigation of the phase space were planned and performed by Felix E. Feiten under supervision of Helmut Kuhlenbeck and Hans-Joachim Freund. During the course of the study Felix E. Feiten established contact with Jan Seifert and Helmut Winter who had already performed the fast atom diffraction experiments that are part of this publication. With the help of Hans-Joachim Freund, Joachim Paier and Joachim Sauer were included in the project and performed DFT calculations to supplement the experimental results of Felix E. Feiten and Jan Seifert. During the course of the experiments and in the preparation of the initial draft all coauthors met several times to discuss the results and their interpretation. The initial draft of the publication was written by Felix E. Feiten with the parts about their respective investigations written by Jan Seifert and Joachim Paier. In the following all coauthors made suggestions for improvements which were implemented by Felix E. Feiten.

Publication 2:

Felix E. Feiten, Helmut Kuhlenbeck, and Hans-Joachim Freund, **Surface Structure of $V_2O_3(0001)$: A Combined I/V-LEED and STM Study** *J. Phys. Chem. C*, **119**, 22961-22969, 2015.

http://dx.doi.org/10.1021/acs.jpcc.5b06943

Contribution of Felix E. Feiten:

All experiments were conducted by Felix E. Feiten under supervision of Helmut Kuhlenbeck and Hans-Joachim Freund. The publication was written by Felix E. Feiten with corrections and suggestions from Helmut Kuhlenbeck and Hans-Joachim Freund.

Publication 3:

Felix E. Feiten, Helmut Kuhlenbeck, and Hans-Joachim Freund, **Reducing the $V_2O_3(0001)$ Surface through Electron Bombardment - A Quantitative Structure Determination with I/V-LEED**, *Phys. Chem. Chem. Phys.* **18**, 3124-3130, 2016

http://dx.doi.org/10.1039/C5CP07390A

Contribution of Felix E. Feiten:

All experiments were conducted by Felix E. Feiten under supervision of Helmut Kuhlenbeck and Hans-Joachim Freund. The DFT calculations and STM simulations were also performed by Felix E. Feiten. The publication was written by Felix E. Feiten with corrections and suggestions from Helmut Kuhlenbeck and Hans-Joachim Freund.

6.2 List of Abbreviations

- c.e.d. - cumulative electron dose
- CMA-ES - covariance matrix adaptation-evolutionary strategy
- DE - differential evolution

- DM termination - double metal termination
- DFT - density functional theory
- FAD - fast atom diffraction
- FHI-aims - Fritz Haber Institute-ab initio molecular simulations package
- FX - Fock exchange
- GGA - generazlited gradient approximation
- HREELS - high resolution electron energy loss spectroscopy
- HSE - Heyd, Scuseria, Erzerhof, referring to the hybrid DFT functional defined by those authors [126, 127]
- IBT - ion beam triangulation
- IRAS - infrared reflection absorption spectroscopy
- I/V-LEED - intensity/voltage-low energy electron eiffraction
- LEED - low energy electron diffraction
- MCP - microchannel plate
- MEIS - medium energy ion scattering
- MSA - mean square amplitude
- NEXAFS - near edge X-ray absorption fine structure
- NICISS - near impact collision ion scattering spectroscopy
- PAW - projector-augmented plane wave
- PBE - Perdew, Becke, Ernzerhof, referring to the GGA-based DFT functional defined by those authors [85]
- PED - photoelectron diffraction
- QMB - quartz crystal microbalance

- SATLEED - Symmetryzed Automated Tensor Low Energy Electron Diffraction
- SM termination - single metal termination
- STM - scanning tunneling microscopy
- UHV - ultra high vacuum
- VASP - Viena Ab initio Simulation Package
- XPS - X-ray Photoelectron Spectroscopy

6.3 Calculation of Scattering Vectors for Debye-Temperature Determination

Since the incoming beam is normal to the surface it can be described completely through its' z-component:

$$\vec{K}_{in} = \begin{pmatrix} 0 \\ 0 \\ k \end{pmatrix} \tag{28}$$

Here k is determined by

$$E + V_0 = \frac{\hbar^2 k^2}{2m_e} \tag{29}$$

with V_0 being the real part of the inner potential inside the sample. With $E = 100\,\mathrm{eV}$ and $V_0 = -3.95\,\mathrm{eV}$ taken from the I/V-LEED calculations

$$\begin{aligned} k &= \sqrt{(E+V_0)\,2m_e}/\hbar \\ &= \sqrt{(100\,\mathrm{eV} - 3.95\,\mathrm{eV}) \cdot 2 \cdot 5.109\,989\,28 \times 10^5\,\mathrm{eV}/c^2}/6.582\,119\,28 \times 10^{-16}\,\mathrm{eV\,s} \\ &= 9.907\,718\,9 \times 10^3\,\mathrm{eV}/\left(c \cdot 6.582\,119\,28 \times 10^{-16}\,\mathrm{eV\,s}\right) \\ &= 1.505\,247\,549 \times 10^{19}\,\mathrm{s}^{-1}/c \\ &= 1.505\,247\,549 \times 10^{19}\,\mathrm{s}^{-1}/299\,792\,458\,\mathrm{m\,s}^{-1} \\ &= 5.020\,965\,367 \times 10^{10}\,\mathrm{m}^{-1} \end{aligned} \tag{30}$$

$$\vec{K}_{in} = \begin{pmatrix} 0 \\ 0 \\ 5.02\,\text{Å}^{-1} \end{pmatrix} \tag{31}$$

$$\vec{K}_{out} = \begin{pmatrix} k_x \\ k_y \\ k_z \end{pmatrix} \tag{32}$$

With energy/momentum-conservation imposing

$$k^2 = k_x^2 + k_y^2 + k_z^2 \tag{33}$$

k_x^2 and k_y^2 being properties of the corresponding reciprocal lattice vector $\vec{g}_{hk}$ k_z^2 can be calculated by

$$k_z^2 = \sqrt{k^2 - k_x^2 - k_y^2} \tag{34}$$

In order to determine the reciprocral lattice vectors $\vec{g}_{10}$ and $\vec{g}_{11}$ the basis vectors of the reciprocal lattice $\vec{a}_1^*$ and $\vec{a}_2^*$ are calculated from the basis vectors of the real space unit cell:

$$\vec{a}_1^* = 2\pi \left(\frac{\vec{a}_2 \times \vec{n}}{\vec{a}_1 \cdot (\vec{a}_2 \times \vec{n})} \right) \tag{35}$$

and

$$\vec{a}_2^* = 2\pi \left(\frac{\vec{n} \times \vec{a}_1}{\vec{a}_2 \cdot (\vec{n} \times \vec{a}_1)} \right) \tag{36}$$

The reciprocal lattice vector then results as

$$\vec{g} = h \cdot \vec{a}_1^* + k \cdot \vec{a}_2^* \tag{37}$$

The lattice vectors of the unit cell are taken from bulk measurements of the V_2O_3 crystal structure [80] and are the same as those used in the I/V-LEED calculations in Publication 1: *Surface Structure of V_2O_3 Revisited*. In the following the units are ommited, all units are given in Å.

$$\vec{a}_1 = \begin{pmatrix} 4.9570 \\ 0 \\ 0 \end{pmatrix} \qquad \vec{a}_2 = \begin{pmatrix} -2.4785 \\ 4.2929 \\ 0 \end{pmatrix} \tag{38}$$

$$\vec{a}_1^* = 2\pi \frac{\begin{pmatrix} -2.4785 \\ 4.2929 \\ 0 \end{pmatrix} \times \begin{pmatrix} 0 \\ 0 \\ 1 \end{pmatrix}}{\begin{pmatrix} 4.9570 \\ 0 \\ 0 \end{pmatrix} \cdot \left[\begin{pmatrix} -2.4785 \\ 4.2929 \\ 0 \end{pmatrix} \times \begin{pmatrix} 0 \\ 0 \\ 1 \end{pmatrix} \right]} \tag{39}$$

$$\begin{aligned} \vec{a}_1^* &= 2\pi \frac{\begin{pmatrix} 4.2929 \\ 2.4785 \\ 0 \end{pmatrix}}{\begin{pmatrix} 4.9570 \\ 0 \\ 0 \end{pmatrix} \cdot \begin{pmatrix} 4.2929 \\ 2.4785 \\ 0 \end{pmatrix}} \\ &= \tfrac{2\pi}{21.28} \begin{pmatrix} 4.2929 \\ 2.4785 \\ 0 \end{pmatrix} = \begin{pmatrix} 1.2675 \\ 0.7318 \\ 0 \end{pmatrix} \end{aligned} \tag{40}$$

and

$$\vec{a}_2^* = 2\pi \frac{\begin{pmatrix} 0 \\ 0 \\ 1 \end{pmatrix} \times \begin{pmatrix} 4.9570 \\ 0 \\ 0 \end{pmatrix}}{\begin{pmatrix} -2.4785 \\ 4.2929 \\ 0 \end{pmatrix} \cdot \left[\begin{pmatrix} 0 \\ 0 \\ 1 \end{pmatrix} \times \begin{pmatrix} 4.9570 \\ 0 \\ 0 \end{pmatrix} \right]} \tag{41}$$

$$\begin{aligned}\vec{a}_1^{\,*} &= 2\pi \frac{\begin{pmatrix} 0 \\ 4.9570 \\ 0 \end{pmatrix}}{\begin{pmatrix} -2.4785 \\ 4.2929 \\ 0 \end{pmatrix} \cdot \begin{pmatrix} 0 \\ 4.9570 \\ 0 \end{pmatrix}} \\ &= \tfrac{2\pi}{21.28} \begin{pmatrix} 0 \\ 4.9570 \\ 0 \end{pmatrix} = \begin{pmatrix} 0 \\ 1.4636 \\ 0 \end{pmatrix}\end{aligned} \tag{42}$$

$$\vec{g}_{10} = 1 \cdot \vec{a}_1^{\,*} + 0 \cdot \vec{a}_2^{\,*} = \begin{pmatrix} 1.2675 \\ 0.7318 \\ 0 \end{pmatrix} \tag{43}$$

$$\vec{g}_{11} = 1 \cdot \vec{a}_1^{\,*} + 1 \cdot \vec{a}_2^{\,*} = \begin{pmatrix} 1.2675 \\ 2.1954 \\ 0 \end{pmatrix} \tag{44}$$

$$\vec{K}_{in} = \begin{pmatrix} 0 \\ 0 \\ 5.02 \end{pmatrix} \qquad \vec{K}_{10} = \begin{pmatrix} 1.2675 \\ 0.7318 \\ -4.8019 \end{pmatrix} \qquad \vec{K}_{11} = \begin{pmatrix} 1.2675 \\ 2.1954 \\ -4.3329 \end{pmatrix} \tag{45}$$

$$\begin{aligned} \Delta\vec{K}_{10} &= \begin{pmatrix} -1.2675 \\ -0.7318 \\ 9.8219 \end{pmatrix} & \Delta\vec{K}_{11} &= \begin{pmatrix} -1.2675 \\ -2.1954 \\ 9.3529 \end{pmatrix} \\ \left(\Delta\vec{K}_{10}\right)^2 &= 98.6118 & \left(\Delta\vec{K}_{11}\right)^2 &= 93.9031 \end{aligned} \tag{46}$$

Bibliography

[1] Dingerdissen, U.; Martin, A.; Herein, D.; Wernicke, H. J. The Development of Industrial Heterogeneous Catalysis. In Handbook of Heterogeneous Catalysis. Wiley-VCH Verlag GmbH & Co. KGaA, **2008**.

[2] Bell, A. T. The impact of nanoscience on heterogeneous catalysis. *Science 299*, **2003**, 1688–1691.

[3] Weckhuysen, B. M.; Keller, D. E. Chemistry, spectroscopy and the role of supported vanadium oxides in heterogeneous catalysis. *Catal. Today 78*, **2003**, 25–46.

[4] Kuhlenbeck, H.; Shaikhutdinov, S.; Freund, H.-J. Well-Ordered Transition Metal Oxide Layers in Model Catalysis - A Series of Case Studies. *Chem. Rev. 113*, **2013**, 3986–4034.

[5] Weiss, W.; Ranke, W. Surface chemistry and catalysis on well-defined epitaxial iron-oxide layers. *Prog. Surf. Sci. 70*, **2002**, 1–151.

[6] Smith, R. D. L.; Pre, M. S.; Fagan, R. D.; Trudel, S. Water Oxidation Catalysis: Electrocatalytic Response to Metal Stoichiometry in Amorphous Metal Oxide Films Containing Iron, Cobalt, and Nickel. *J. Am. Chem. Soc. 135*, **2013**, 11580–11586.

[7] Freund, H.-J.; Bäumer, M.; Kuhlenbeck, H. Catalysis and Surface Science: What Do We Learn from Studies of Oxide-Supported Cluster Model Systems? *Adv. Catal. 45*, **2000**, 333–384.

[8] Freund, H.-J.; Ernst, N.; Risse, T.; Hamann, H.; Rupprechter, G. Models in Heterogeneous Catalysis: Surface Science Quo Vadis? *Phys. status solidi 187*, **2001**, 257–274.

[9] Nilius, N.; Risse, T.; Shaikhutdinov, S.; Sterrer, M.; Freund, H.-J. Model catalysts based on Au clusters and nano particles. In Gold Clusters, Colloids and Nanoparticles II. Springer, **2014**, 91–138.

[10] Freund, H.-J. Oxide Films as Catalytic Materials and Models of Real Catalysts. In Pacchioni, G.; Valeri, S. (eds.), Oxide Ultrathin Films. Wiley-VCH, Weinheim, **2012**, 145–179.

[11] Ertl, G.; Freund, H.-J. Catalysis and Surface Science. *Phys. Today 52*, **1999**, 32.

[12] Freund, H. J.; Libuda, J.; Bäumer, M.; Risse, T.; Carlsson, A. Cluster, facets, and edges: Site-dependent selective chemistry on model catalysts. *Chem. Rec. 3*, **2003**, 181–200.

[13] Freund, H. J. Model studies on heterogeneous catalysts at the atomic level. *Catal. Today 100*, **2005**, 3–9.

[14] Zhou, K.; Li, Y. Catalysis based on nanocrystals with well-defined facets. *Angew. Chemie - Int. Ed. 51*, **2012**, 602–613.

[15] Haber, J. Fifty years of my romance with vanadium oxide catalysts. *Catal. Today 142*, **2009**, 100–113.

[16] Wriedt, H. A. The O-V (Oxygen-Vanadium) System. *J. Phase Equilibria 10*, **1989**, 271–277.

[17] Henrich, V. E.; Cox, P. A. The Surface Science of Metal Oxides. Cambridge University Press, Cambridge, **1994**.

[18] Stefanovich, G.; Pergament, A.; Stefanovich, D. Electrical switching and Mott transition in VO_2. *J. Phys. Condens. Matter 12*, **2000**, 8837–8845.

[19] Kim, H.-T.; Chae, B.-G.; Youn, D.-H.; Maeng, S.-L.; Kim, G.; Kang, K.-Y.; Lim, Y.-S. Mechanism and observation of Mott transition in VO_2-based two- and three-terminal devices. *New J. Phys. 6*, **2004**, 52–52.

[20] Graner, F.; Glazier, J. a. VO_2: Peierls or Mott-Hubbard? A View from Band Theory. *Phys. Rev. Lett. 69*, **1992**, 2013–2016.

[21] Biermann, S.; Poteryaev, A.; Lichtenstein, A. I.; Georges, A. Dynamical Singlets and Correlation-Assisted Peierls Transition in VO_2. *Phys. Rev. Lett. 94*, **2005**, 26404.

[22] Qazilbash, M. M.; Brehm, M.; Chae, B.-G.; Ho, P.-C.; Andreev, G. O.; Kim, B.-J.; Yun, S. J.; Balatsky, A. V.; Maple, M. B.; Keilmann, F.; Kim, H.-T.; Basov, D. N. Mott Transition in VO_2 Revealed by Infrared Spectroscopy and Nano-Imaging. *Science 318*, **2007**, 1750–1753.

[23] Adler, D.; Feinleib, J. Semiconductor-to-metal transition in V_2O_3. *Phys. Rev. Lett. 12*, **1964**, 700–703.

[24] McWhan, D. B.; Rice, T. M.; Remeika, J. P. Mott Transition in Cr-doped V_2O_3. *Phys. Rev. Lett. 23*, **1969**, 1384.

[25] McWhan, D. B.; Menth, A.; Remeika, J. P.; Brinkman, W. F.; Rice, T. M. Metal-insulator transitions in pure and doped V_2O_3. *Phys. Rev. B 7*, **1973**, 1920–1931.

[26] Yethiraj, M. Pure and Doped Vanadium Sesquioxide: A Brief Experimental Review. *J. Solid State Chem. 88*, **1990**, 53–69.

[27] Held, K.; Keller, G.; Eyert, V.; Vollhardt, D.; Anisimov, V. I. Mott-Hubbard Metal-Insulator Transition in Paramagnetic V_2O_3: An LDA+DMFT(QMC) Study. *Phys. Rev. Lett. 86*, **2001**, 5345–5348.

[28] Keller, G.; Held, K.; Eyert, V.; Vollhardt, D.; Anisimov, V. I. Electronic structure of paramagnetic V_2O_3: Strongly correlated metallic and Mott insulating phase. *Phys. Rev. B 70*, **2004**, 205116.

[29] Pfuner, F.; Schoiswohl, J.; Sock, M.; Surnev, S.; Ramsey, M. G.; Netzer, F. P. The metal-insulator transition in $V_2O_3(0001)$ thin films: surface termination effects. *J. Phys. Condens. Matter 17*, **2005**, 4035–4047.

[30] Jerominek, H. Vanadium oxide films for optical switching and detection. *Opt. Eng. 32*, **1993**, 2092.

[31] Whittingham, M. S. Lithium batteries and cathode materials. *Chem. Rev. 104*, **2004**, 4271–4301.

[32] Cao, A.-M.; Hu, J.-S.; Liang, H.-P.; Wan, L.-J. Self-Assembled Vanadium Pentoxide (V_2O_5) Hollow Microspheres from Nanorods and Their Application in Lithium-Ion Batteries. *Angew. Chemie Int. Ed. 44*, **2005**, 4391–4395.

[33] Wang, Y.; Cao, G. Synthesis and enhanced intercalation properties of nanostructured vanadium oxides. *Chem. Mater. 18*, **2006**, 2787–2804.

[34] Shrotriya, V.; Li, G.; Yao, Y.; Chu, C.-W.; Yang, Y. Transition metal oxides as the buffer layer for polymer photovoltaic cells. *Appl. Phys. Lett. 88*, **2006**, 073508.

[35] Ho, S. L.; Kwak, D.; Dong, Y. L.; Seung, G. L.; Cho, K. UV-driven reversible switching of a roselike vanadium oxide film between superhydrophobicity and superhydrophilicity. *J. Am. Chem. Soc. 129*, **2007**, 4128–4129.

[36] Chen, Z.; Augustyn, V.; Wen, J.; Zhang, Y.; Shen, M.; Dunn, B.; Lu, Y. High-Performance Supercapacitors Based on Intertwined CNT/V_2O_5 Nanowire Nanocomposites. *Adv. Mater. 23*, **2011**, 791–795.

[37] Boukhalfa, S.; Evanoff, K.; Yushin, G. Atomic layer deposition of vanadium oxide on carbon nanotubes for high-power supercapacitor electrodes. *Energy Environ. Sci. 5*, **2012**, 6872.

[38] Bauer, G.; Güther, V.; Hess, H.; Otto, A.; Roidl, O.; Roller, H.; Sattelberger, S. Vanadium and Vanadium Compounds. In Ullmann's Encyclopedia of Industrial Chemistry. Wiley-VCH, **2012**, 49–69.

[39] Simard, G. L.; Steger, J. F.; Arnott, R. J.; Siegel, L. A. Vanadium Oxides as Oxidation Catalysts. *Ind. Eng. Chem. 47*, **1955**, 1424–1430.

[40] Kasaoka, S.; Sasaoka, E.; Iwasaki, H. Vanadium Oxides (V_2O_x) Catalysts for Dry-Type and Simultaneous Removal of Sulfur Oxides and Nitrogen Oxides with Ammonia at Low Temperature. *Bull. Chem. Soc. Jpn. 62*, **1989**, 1226–1232.

[41] Bond, G. C.; Tahir, S. F. Vanadium oxide monolayer catalysts Preparation, characterization and catalytic activity. *Appl. Catal. 71*, **1991**, 1–31.

[42] Deo, G.; Wachs, I. E. Reactivity of Supported Vanadium Oxide Catalysts: The Partial Oxidation of Methanol. *J. Catal. 146*, **1993**, 323–334.

[43] Kurtz, R.; Henrich, V. Surface electronic structure and chemisorption on corundum transition-metal oxides: V_2O_3. *Phys. Rev. B 28*, **1983**, 6699–6706.

[44] Tepper, B.; Richter, B.; Dupuis, A.-C.; Kuhlenbeck, H.; Hucho, C.; Schilbe, P.; bin Yarmo, M.; Freund, H.-J. Adsorption of molecular and atomic hydrogen on vacuum-cleaved $V_2O_5(001)$. *Surf. Sci. 496*, **2002**, 64–72.

[45] Window, A. J.; Hentz, A.; Sheppard, D. C.; Parkinson, G. S.; Niehus, H.; Ahlbehrendt, D.; Noakes, T. C. Q.; Bailey, P.; Woodruff, D. P. $V_2O_3(0001)$ Surface Termination: Phase Equilibrium. *Phys. Rev. Lett. 107*, **2011**, 016105.

[46] Window, A.; Hentz, A.; Sheppard, D.; Parkinson, G.; Woodruff, D.; Unterberger, W.; Noakes, T.; Bailey, P.; Ganduglia-Pirovano, M.; Sauer, J. The structure of epitaxial V_2O_3 films and their surfaces: A medium energy ion scattering study. *Surf. Sci. 606*, **2012**, 1716–1727.

[47] Seifert, J.; Meyer, E.; Winter, H.; Kuhlenbeck, H. Surface termination of an ultrathin V_2O_3-film on Au(111) studied via ion beam triangulation. *Surf. Sci. 606*, **2012**, L41–L44.

[48] Lewis, K. B.; Oyama, S. T.; Somorjai, G. A. The preparation and reactivity of thin, ordered films of vanadium oxide on Au(111). *Surf. Sci. 233*, **1990**, 75–83.

[49] Biener, J.; Bäumer, M.; Madix, R. J.; Liu, P.; Nelson, E. J.; Kendelewicz, T.; Brown Jr, G. E. A synchrotron study of the growth of vanadium oxide on $Al_2O_3(0001)$. *Surf. Sci. 441*, **1999**, 1–9.

[50] Guo, Q.; Lee, S.; Goodman, D. W. Vanadium oxides thin films grown on rutile $TiO_2(110)$-(1×1) and (1×2) surfaces. *Surf. Sci. 437*, **1999**, 38–48.

[51] Biener, J.; Bäumer, M.; Madix, R. A synchrotron study of the deposition of vanadia on $TiO_2(110)$. *Surf. Sci. 432*, **1999**, 178–188.

[52] Price, N. J.; Reitz, J. B.; Madix, R. J.; Solomon, E. A synchrotron XPS study of the vanadiatitania system as a model for monolayer oxide catalysts. *J. Electron Spectros. Relat. Phenomena 98-99*, **1999**, 257–266.

[53] Sambi, M.; Negra, M. D.; Granozzi, G. The structure of vanadia ultrathin films grown on TiO_2 (110) in an oxygen ambient. *Surf. Sci. 470*, **2000**.

[54] Wong, G. S.; Kragten, D. D.; Vohs, J. M. Oxidation of methanol to formaldehyde on TiO_2(110)-supported vanadia films. *J. Phys. Chem. B 105*, **2001**, 1366–1373.

[55] Magg, N.; Giorgi, J. B.; Schroeder, T.; Bäumer, M.; Freund, H. J. Model catalyst studies on vanadia particles deposited onto a thin-film alumina support - 1. Structural characterization. *J. Phys. Chem. B 106*, **2002**, 8756–8761.

[56] Wong, G.; Vohs, J. An XPS study of the growth and electronic structure of vanadia films supported on CeO_2(111). *Surf. Sci. 498*, **2002**, 266–274.

[57] Dupuis, A.-C.; Abu-Haija, M.; Richter, B.; Kuhlenbeck, H.; Freund, H.-J. V_2O_3(0001) on Au(111) and W(110): growth, termination and electronic structure. *Surf. Sci. 539*, **2003**, 99–112.

[58] Abu Haija, M.; Guimond, S.; Uhl, A.; Kuhlenbeck, H.; Freund, H.-J. Adsorption of water on thin V_2O_3(0001) films. *Surf. Sci. 600*, **2006**, 1040–1047.

[59] Abu Haija, M.; Guimond, S.; Romanyshyn, Y.; Uhl, A.; Kuhlenbeck, H.; Todorova, T.; Ganduglia-Pirovano, M. V.; Döbler, J.; Sauer, J.; Freund, H.-J. Low temperature adsorption of oxygen on reduced V_2O_3(0001) surfaces. *Surf. Sci. 600*, **2006**, 1497–1503.

[60] Bandara, A.; Abu-Haija, M.; Höbel, F.; Kuhlenbeck, H.; Rupprechter, G.; Freund, H.-J. Molecular adsorption on V_2O_3(0001)/Au(111) surfaces. *Top. Catal. 46*, **2007**, 223–230.

[61] Kolczewski, C.; Hermann, K.; Guimond, S.; Kuhlenbeck, H.; Freund, H.-J. Identification of the vanadyl terminated V_2O_3(0001) surface by NEXAFS spectroscopy: A combined theoretical and experimental study. *Surf. Sci. 601*, **2007**, 5394–5402.

[62] Romanyshyn, Y.; Guimond, S.; Kuhlenbeck, H.; Kaya, S.; Blum, R. P.; Niehus, H.; Shaikhutdinov, S.; Simic-Milosevic, V.; Nilius, N.; Freund, H.-J.; Ganduglia-Pirovano, M. V.; Fortrie, R.; Döbler, J.; Sauer, J. Selectivity in Methanol Oxidation as Studied on Model Systems Involving Vanadium Oxides. *Top. Catal. 50*, **2008**, 106–115.

[63] Göbke, D.; Romanyshyn, Y.; Guimond, S.; Sturm, J. M.; Kuhlenbeck, H.; Döbler, J.; Reinhardt, U.; Ganduglia-Pirovano, M. V.; Sauer, J.; Freund, H.-J. Formaldehyde Formation on Vanadium Oxide Surfaces $V_2O_3(0001)$ and $V_2O_5(001)$: How does the Stable Methoxy Intermediate Form? *Angew. Chem. Int. Ed. Engl. 48*, **2009**, 3695–8.

[64] Nilius, N.; Brázdová, V.; Ganduglia-Pirovano, M.-V.; Simic-Milosevic, V.; Sauer, J.; Freund, H.-F. Nucleation of gold atoms on vanadyl-terminated $V_2O_3(0001)$. *New J. Phys. 11*, **2009**, 093007.

[65] Romanyshyn, Y.; Guimond, S.; Göbke, D.; Sturm, J. M.; Kuhlenbeck, H.; Döbler, J.; Ganduglia-Pirovano, M. V.; Sauer, J.; Freund, H.-J. Methanol Adsorption on $V_2O_3(0001)$. *Top. Catal. 54*, **2011**, 669–684.

[66] Yang, B.; Lin, X.; Nilius, N.; Freund, H.-J. Role of the $V_2O_3(0001)$ Defect Structure in the Adsorption of Au Adatoms. *J. Phys. Chem. C* **2011**, 3404–3409.

[67] Kishi, K.; Hirai, K.; Yamamoto, T. XPS and XAES study for oxidation of V/Cu(100) and V,Na/Cu(100) surfaces. *Surf. Sci. 290*, **1993**, 309–318.

[68] Kishi, K.; Fujiwara, K. Ultrathin nickel oxide on the V_2O_3/Cu(100) surface studied by XPS. *J. Electron Spectros. Relat. Phenomena 71*, **1995**, 51–59.

[69] Leisenberger, F. P.; Surnev, S.; Vitali, L.; Ramsey, M. G.; Netzer, F. P. Nature, growth, and stability of vanadium oxides on Pd(111). *J. Vac. Sci. Technol. A Vacuum, Surfaces, Film. 17*, **1999**, 1743.

[70] Surnev, S.; Kresse, G.; Sock, M.; Ramsey, M. G.; Netzer, F. P. Surface structures of ultrathin vanadium oxide films on Pd(111). *Surf. Sci. 495*, **2001**, 91–106.

[71] Kröger, E. A.; Sayago, D. I.; Allegretti, F.; Knight, M. J.; Polcik, M.; Unterberger, W.; Lerotholi, T. J.; Hogan, K. A.; Lamont, C. L. A.; Woodruff, D. P. The structure of the $V_2O_3(0001)$ surface: A scanned-energy mode photoelectron diffraction study. *Surf. Sci. 601*, **2007**, 3350–3360.

[72] Kröger, E. A.; Sayago, D. I.; Allegretti, F.; Knight, M. J.; Polcik, M.; Unterberger, W.; Lerotholi, T. J.; Hogan, K. A.; Lamont, C. L. A.; Cavalleri, M.; Hermann, K.;

Woodruff, D. P. The local structure of OH species on the $V_2O_3(0001)$ surface: A scanned-energy mode photoelectron diffraction study. *Surf. Sci. 602*, **2008**, 1267–1279.

[73] Schoiswohl, J.; Sock, M.; Surnev, S.; Ramsey, M.; Netzer, F.; Kresse, G.; Andersen, J. $V_2O_3(0001)$ surface terminations: from oxygen- to vanadium-rich. *Surf. Sci. 555*, **2004**, 101–117.

[74] Schoiswohl, J.; Sock, M.; Eck, S.; Surnev, S.; Ramsey, M. G.; Netzer, F. P.; Kresse, G. Atomic-level growth study of vanadium oxide nanostructures on Rh(111). *Phys. Rev. B 69*, **2004**, 155403.

[75] Schoiswohl, J.; Surnev, S.; Netzer, F. P.; Kresse, G. Vanadium oxide nanostructures: from zero- to three-dimensional. *J. Phys. Condens. Matter 18*, **2006**, R1–R14.

[76] Xiao, W.; Xie, K.; Guo, Q.; Wang, E. G. Cu on $V_2O_3(0001)$ Films: Growth and Interaction. *J. Phys. Chem. B 106*, **2002**, 4721–4724.

[77] Xiao, W.; Xie, K.; Guo, Q.; Wang, E. G. Interaction of metal with oxide films : V on $Cr_2O_3(0001)$/Re(0001) and Cr on $V_2O_3(0001)$/Re(0001). *J. Phys. Condens. Matter 14*, **2002**, 6321–6328.

[78] Niehus, H.; Blum, R.-P.; Ahlbehrendt, D. Formation of Vanadium Oxide Films on $Cu_3Au(100)$. *Phys. status solidi 187*, **2001**, 151–159.

[79] Niehus, H.; Blum, R.-P.; Ahlbehrendt, D. Structure of Vanadium Oxide (V_2O_3) Grown on $Cu_3Au(100)$. *Surf. Rev. Lett. 10*, **2003**, 353–359.

[80] Tenailleau, C.; Suard, E.; Rodriguez-Carvajal, J.; Crosnier-Lopez, M. P.; Lacorre, P. Effect of Mo Doping on the Room-Temperature Structure of Vanadium Sesquioxide. *Chem. Mater. 14*, **2002**, 3569–3575.

[81] Czekaj, I.; Hermann, K.; Witko, M. Ab initio density functional theory studies on oxygen stabilization at the $V_2O_3(0001)$ surface. *Surf. Sci. 545*, **2003**, 85–98.

[82] Czekaj, I.; Hermann, K.; Witko, M. Relaxation and electronic structure of the $V_2O_3(0001)$ surface: ab initio cluster model studies. *Surf. Sci. 525*, **2003**, 33–45.

[83] Czekaj, I.; Witko, M.; Hermann, K. Structure and electronic properties of the $V_2O_3(0001)$ surface: ab initio density functional theory cluster studies. *Surf. Sci. 525*, **2003**, 46–56.

[84] Vosko, S. H.; Wilk, L.; Nusair, M. Accurate Spin-Dependent Electron Liquid Correlation Energies for Local Spin-Density Calculations - a Critical Analysis. *Can. J. Phys.* **1980**.

[85] Perdew, J. P.; Burke, K.; Ernzerhof, M. Generalized Gradient Approximation Made Simple. *Phys. Rev. Lett. 77*, **1996**, 3865–3868.

[86] Hammer, B.; Hansen, L.; Nørskov, J. Improved adsorption energetics within density-functional theory using revised Perdew-Burke-Ernzerhof functionals. *Phys. Rev. B 59*, **1999**, 7413–7421.

[87] Blöchl, P. Projector augmented-wave method. *Phys. Rev. B 50*, **1994**, 17953–17979.

[88] Kresse, G.; Joubert, D. From ultrasoft pseudopotentials to the projector augmented-wave method. *Phys. Rev. B 59*, **1999**, 1758–1775.

[89] Wang, Y.; Perdew, J. P. Correlation hole of the spin-polarized electron gas, with exact small-wave-vector and high-density scaling. *Phys. Rev. B 44*, **1991**, 13298–13307.

[90] Perdew, J.; Chevary, J.; Vosko, S.; Jackson, K.; Pederson, M.; Singh, D.; Fiolhais, C. Erratum: Atoms, molecules, solids, and surfaces: Applications of the generalized gradient approximation for exchange and correlation. *Phys. Rev. B 48*, **1993**, 4978–4978.

[91] Kresse, G.; Surnev, S.; Schoiswohl, J.; Netzer, F. P. $V_2O_3(0001)$ surface terminations: a density functional study. *Surf. Sci. 555*, **2004**, 118–134.

[92] Todorova, T. K.; Ganduglia-Pirovano, M. V.; Sauer, J. Vanadium Oxides on Aluminum Oxide Supports. 1. Surface Termination and Reducibility of Vanadia Films on alpha-$Al_2O_3(0001)$. *J. Phys. Chem. B 109*, **2005**, 23523–31.

[93] Kresse, G.; Surnev, S.; Ramsey, M.; Netzer, F. First-principles calculations for V_xO_y grown on Pd(111). *Surf. Sci. 492*, **2001**, 329–344.

[94] Schoiswohl, J.; Surnev, S.; Sock, M.; Eck, S.; Ramsey, M.; Netzer, F.; Kresse, G. Reduction of vanadium-oxide monolayer structures. *Phys. Rev. B 71*, **2005**, 1–8.

[95] Freund, H.-J.; Dillmann, B.; Seiferth, O.; Klivenyi, G.; Bender, M.; Ehrlich, D.; Hemmerich, I.; Cappus, D. Molecules on oxide surfaces. *Catal. Today 32*, **1996**, 1–10.

[96] Dillmann, B.; Rohr, F.; Seiferth, O.; Klivenyi, G.; Bender, M.; Homann, K.; Yakovkin, I. N.; Ehrlich, D.; Bumer, M.; Kuhlenbeck, H.; Freund, H.-J. Adsorption on a polar oxide surface: O_2, C_2H_4 and Na on $Cr_2O_3(0001)/Cr(110)$. *Faraday Discuss. 105*, **1996**, 295.

[97] Kolczewski, C.; Hermann, K. Ab initio DFT studies of oxygen K edge NEXAFS spectra for the $V_2O_3(0001)$ surface. *Theor. Chem. Acc. 114*, **2005**, 60–67.

[98] Guimond, S.; Haija, M. A.; Kaya, S.; Lu, J.; Weissenrieder, J.; Shakihutdinov, S.; Kuhlenbeck, H.; Freund, H.-J.; Döbler, J.; Sauer, J. Vanadium oxide surfaces and supported vanadium oxide nanoparticles. *Top. Catal. 38*, **2006**, 117–125.

[99] Schoiswohl, J.; Tzvetkov, G.; Pfuner, F.; Ramsey, M. G.; Surnev, S.; Netzer, F. P. Reactivity of $V_2O_3(0001)$ surfaces: molecular vs dissociative adsorption of water. *Phys. Chem. Chem. Phys. 8*, **2006**, 1614–23.

[100] Todorova, T.; Ganduglia-Pirovano, M.; Sauer, J. Vanadium Oxides on Aluminum Oxide Supports. 3. Metastable κ-$Al_2O_3(001)$ Compared to α-$Al_2O_3(0001)$. *J. Phys. Chem. C 111*, **2007**, 5141–5153.

[101] Wiesendanger, R. Scanning probe microscopy and spectroscopy: methods and applications. University Press, Cambridge, **1994**.

[102] Güntherodt, H.-J.; Wiesendanger, R. (eds.). Scanning probe microscopy and spectroscopy: methods and applications. University Press, Berlin, **1994**.

[103] Davisson, C.; Germer, L. H. The scattering of electrons by a single crystal of nickel. *Nature 119*, **1927**, 558–560.

[104] Barbieri, A.; Van Hove, M. priv. comm., http://www.icts.hkbu.edu.hk/vanhove/.

[105] Somorjai, G. Chemistry in Two Dimensions: Surfaces. Cornell University Press, Ithaca (N.Y.), **1981**.

[106] Van Hove, M. A.; Tong, S. Y. Surface Crystallography by LEED. Springer-Verlag, Berlin Heidelberg New York, **1979**.

[107] Pendry, J. B. Low Energy Electron Diffraction. Academic Press Inc. (London) Ltd., London, **1974**.

[108] Pendry, J. B. Reliability factors for LEED calculations. *J. Phys. C Solid State Phys. 13*, **1980**, 937–944.

[109] Powell, M. J. D. An efficient method for finding the minimum of a function of several variables without calculating derivatives. *The Computer Journal 7*, **1964**, 155–162.

[110] Rous, P.; Pendry, J. Tensor LEED I: A technique for high speed surface structure determination by low energy electron diffraction. TLEED1. *Computer Physics Communications 54*, **1989**, 137 – 156.

[111] Rous, P.; Pendry, J. The theory of tensor LEED. *Surface Science 219*, **1989**, 355 – 372.

[112] Hansen, N.; Ostermeier, A. Adapting Arbitrary Normal Mutation Distributions in Evolution Strategies: The Covariance Matrix Adaptation. In Proc. 1996 IEEE Intern. Conf. Evol. Comput. (ICEC '96). **1996**, 312–317.

[113] Igel, C.; Heidrich-Meisner, V.; Glasmachers, T. Shark. *J. Mach. Learn. Res. 9*, **2008**, 993–996.

[114] Storn, R.; Price, K. Differential Evolution - A Simple and Efficient Heuristic for Global Optimization over Continuous Spaces. *J. Glob. Optim. 11*, **1997**, 341–359.

[115] Binnig, G.; Rohrer, H.; Gerber, C.; Weibel, E. Tunneling through a controllable vacuum gap. *Appl. Phys. Lett. 40*, **1982**, 178–180.

[116] Binnig, G.; Rohrer, H.; Gerber, C.; Weibel, E. Surface Studies by Scanning Tunneling Microscopy. *Phys. Rev. Lett. 49*, **1982**, 57–61.

[117] Hertz, H. Ueber einen Einfluss des ultravioletten Lichtes auf die electrische Entladung. *Ann. der Phys. und Chemie 267*, **1887**, 983–1000.

[118] Einstein, A. Über einen die Erzeugung und Verwandlung des Lichtes betreffenden heuristischen Gesichtspunkt. *Ann. Phys. 322*, **1905**, 132–148.

[119] Keer, H.; Dickerson, D.; Kuwamoto, H.; Barros, H.; Honig, J. Heat Capacity of Pure and Doped V_2O_3 Single Crystals. *Journal of Solid State Chemistry 19*, **1976**, 95–102.

[120] van Delft, F. Bulk and surface Debye temperatures in relation to cohesive energy and Lennard-Jones potentials. *Surface Science 251-252*, **1991**, 690–695.

[121] Jepsen, D. W.; Marcus, P. M.; Jona, F. The Determination of Surface Debye Temperatures from Low-Energy Electron Diffraction Data. *Surface Science 41*, **1974**, 223–236.

[122] Vogt, J.; Henning, J.; Weiss, H. The structure of $CaF_2(111)$ and $BaF_2(111)$ single crystal surfaces: A tensor low energy electron diffraction study. *Surf. Sci. 578*, **2005**, 57–70.

[123] Thacher, H. C. Rational Approximations for the Debye Functions. *The Journal of Chemical Physics 32*, **1960**, 638.

[124] Steurer, W.; Apfolter, A.; Koch, M.; Ernst, W. E.; Holst, B. Surface Debye temperature of α-quartz(0001). *Surface Science 602*, **2008**, 1080–1083.

[125] Seifert, J.; Busch, M.; Meyer, E.; Winter, H. Surface structure of alanine on Cu(110) via grazing scattering of fast atoms and molecules. *Phys. Rev. B 89*, **2014**, 075404.

[126] Heyd, J.; Scuseria, G. E.; Ernzerhof, M. Hybrid functionals based on a screened Coulomb potential. *J. Chem. Phys. 118*, **2003**, 8207.

[127] Heyd, J.; Scuseria, G. E.; Ernzerhof, M. Erratum: Hybrid functionals based on a screened Coulomb potential [J. Chem. Phys. 118, 8207 (2003)]. *J. Chem. Phys. 124*, **2006**, 219906.